

International Journal of Aerospace Engineering

# Modelling and Optimizing Structural Behavior of Advanced Materials for Aerospace

Lead Guest Editor: Roberto G. Citarella

Guest Editors: Filippo Berto and Paulo T. de Castro





---

# **Modelling and Optimizing Structural Behavior of Advanced Materials for Aerospace**

International Journal of Aerospace Engineering

---

## **Modelling and Optimizing Structural Behavior of Advanced Materials for Aerospace**

Lead Guest Editor: Roberto G. Citarella

Guest Editors: Filippo Berto and Paulo T. de Castro



---

Copyright © 2018 Hindawi. All rights reserved.

This is a special issue published in “International Journal of Aerospace Engineering.” All articles are open access articles distributed under the Creative Commons Attribution License, which permits unrestricted use, distribution, and reproduction in any medium, provided the original work is properly cited.

## Editorial Board

José A. Acosta, Spain  
Noor Afzal, India  
Rafic M. Ajaj, UAE  
Antonio Andreini, Italy  
Hikmat Asadov, Azerbaijan  
Giulio Avanzini, Italy  
Nicolas Avdelidis, Canada  
Wen Bao, China  
Franco Bernelli-Zazzera, Italy  
D. Bhattacharyya, New Zealand  
James D. Biggs, Italy  
Paolo Castaldi, Italy  
Pedro Castillo, France  
André Cavalieri, Brazil  
Angelo Cervone, Netherlands  
Enrico Cestino, Italy  
Christian Circi, Italy  
Antonio Concilio, Italy  
Richard Curran, Netherlands  
Christopher J. Damaren, Canada  
Giovanni Delibra, Italy  
Gang Ding, China  
Boris Epstein, Israel  
Juan-Antonio Escareno, France  
Richard Flay, New Zealand  
Paolo Gasbarri, Italy  
Santiago Hernández, Spain  
Robert W. Hewson, UK  
Kathleen C. Howell, USA  
Qinglei Hu, China  
Giacomo V. Iungo, USA  
Gustaaf B. Jacobs, USA  
Ratneshwar Jha, USA  
John B. Kosmatka, USA  
Chetan S. Kulkarni, USA  
Vaios Lappas, Greece  
Timothy Lee, Canada  
Rick Lind, USA  
William W. Liou, USA  
Enrico C. Lorenzini, Italy  
Joseph Majdalani, USA  
James J. McGuirk, UK  
Maj D. Mirmirani, USA  
Marco Morandini, Italy  
Joseph Morlier, France  
Giovanni Palmerini, Italy  
Ch. Oliver Paschereit, Germany  
Jose Carlos Páscoa, Portugal  
Dario Pastrone, Italy  
Marco Pizzarelli, Italy  
Mauro Pontani, Italy  
Seid H. Pourtakdoust, Iran  
Ning Qin, UK  
Mahmut Reyhanoglu, USA  
Fabio Santoni, Italy  
Ennes Sarradj, Germany  
Meinhard T. Schobeiri, USA  
Jacopo Serafini, Italy  
Kenneth M. Sobel, USA  
Zhiguang SONG, China  
Jeremy Straub, USA  
Paolo Tortora, Italy  
Linda L. Vahala, USA  
Eusebio Valero, Spain  
Angel Velazquez, Spain  
Dries Verstraete, Australia  
Antonio Viviani, Italy  
Yue Wang, China  
Paul Williams, Netherlands  
Teng Wu, USA  
Hao J. Xia, UK  
Youngbin Yoon, Republic of Korea  
Youmin Zhang, Canada  
Dan Zhao, New Zealand

# Contents

---

## **Modelling and Optimizing Structural Behavior of Advanced Materials for Aerospace**

Roberto G. Citarella , Filippo Berto , and Paulo M. S. T. de Castro   
Editorial (2 pages), Article ID 6296145, Volume 2018 (2018)

## **Numerical-Experimental Assessment of a Hybrid FE-MB Model of an Aircraft Seat Sled Test**

F. Caputo , A. De Luca , F. Marulo, M. Guida , and B. Vitolo  
Research Article (7 pages), Article ID 8943826, Volume 2018 (2018)

## **Optimization of Hybrid Laminates with Extension-Shear Coupling**

Da Cui  and Daokui Li   
Research Article (12 pages), Article ID 9869105, Volume 2018 (2018)

## **Aeronautical and Aerospace Material and Structural Damages to Failures: Theoretical Concepts**

Andriy Viktorovich Goncharenko   
Research Article (7 pages), Article ID 4126085, Volume 2018 (2018)

## **Effective Mechanical Property Estimation of Composite Solid Propellants Based on VCFEM**

Liu-Lei Shen, Zhi-Bin Shen , Yan Xie, and Hai-Yang Li   
Research Article (9 pages), Article ID 2050876, Volume 2018 (2018)

## **Analytical Study on Deformation and Structural Safety of Parafoil**

Longfang Wang  and Weiliang He   
Research Article (7 pages), Article ID 8924983, Volume 2018 (2018)

## **Application of a Cohesive Zone Model for Simulating Fatigue Crack Growth from Moderate to High $\Delta K$ Levels of Inconel 718**

Huan Li , Jinshan Li, and Huang Yuan  
Research Article (13 pages), Article ID 4048386, Volume 2018 (2018)

## Editorial

# Modelling and Optimizing Structural Behavior of Advanced Materials for Aerospace

**Roberto G. Citarella** <sup>1</sup>, **Filippo Berto** <sup>2</sup> and **Paulo M. S. T. de Castro** <sup>3</sup>

<sup>1</sup>University of Salerno, Fisciano, Italy

<sup>2</sup>Norwegian University of Science and Technology, Trondheim, Norway

<sup>3</sup>Faculdade de Engenharia da Universidade do Porto, Porto, Portugal

Correspondence should be addressed to Roberto G. Citarella; [rcitarella@unisa.it](mailto:rcitarella@unisa.it)

Received 18 July 2018; Accepted 18 July 2018; Published 13 September 2018

Copyright © 2018 Roberto G. Citarella et al. This is an open access article distributed under the Creative Commons Attribution License, which permits unrestricted use, distribution, and reproduction in any medium, provided the original work is properly cited.

Aeronautics and aerospace face great pressure for ever increasing performance and efficiency while ensuring maximum reliability and controlling costs. Material selection, structural design, and fabrication methods play a central role among many different contributions for achieving those objectives.

The main metallic materials have been Al alloys, where the introduction of special alloying (Li, Sc, etc.) may substantially improve performance, and Ti alloys playing an increasingly important role because of their corrosion performance. The trends for additive manufacturing (AM) imply that components may become simpler, reducing weight and part count, a trend that is also supported by fabrication techniques as friction stir welding or laser beam welding leading to integral structures.

Among composites, thin ply laminates and design of composites for specific performance are the object of continuing interest and progress. Joining and adhesive technology is an important area where improved structural performance and durability are expected.

Open problems exist in all those areas, as exemplified by the assurance of integrity and mechanical performance of AM parts or the improvement of composite structure fabrication through reduction of shimming and other nonadded value operations.

The understanding of the mechanical behavior and its incorporation into design practice is made through structural analysis, and this subject is also of interest for this special issue. Computational mechanics has progressed from the

traditional FEM and DBEM approaches to combined/hybrid and multiscale analyses that may accurately model and predict crack paths and damage within controlled computational effort. Some complications arise when considering modelling of crack propagation in orthotropic materials like single crystal and directionally solidified polycrystalline components (typical application in first-stage aircraft turbines).

The purpose of this special issue is to draw attention of the scientific community to recent advances in modelling and optimizing structural behavior of advanced materials for aerospace and their possible applications.

In this special issue researchers contributed original research articles as well as review articles on modelling and optimizing structural behavior and damage of advanced materials used in aeronautics and aerospace, also considering nondestructive testing and evaluation.

Theoretical, numerical, and experimental contributions describing original research results and innovative concepts on aeronautical and aerospace materials and structures were collected.

The special issue includes several high-quality papers written by leading and emerging specialists in the field.

13 submissions have been received. Among the articles collected, a number of high-quality papers existed, which led to 6 published articles.

A very short description of the addressed topics, in the order of themes cited below, is presented as follows:

In “Numerical-Experimental Assessment of a Hybrid FE-MB Model of an Aircraft Seat Sled Test” by F. Caputo et al.,

the development of an established hybrid multibody- (MB-) finite element (FE) model for the simulation of an experimental sled test was provided. The numerical investigation was carried out by focusing on the passenger passive safety: the occupant injury assessment was quantitatively monitored by means of the Head Injury Criterion (HIC). Numerical results provided by the hybrid model proposed in the paper were compared with the experimental ones, provided by Geven S.p.A. company, and with the results carried out by a previously developed full-FE model, showing a good level of consistency vs. experimental results and a significant reduction of computing time vs. full-FE analyses.

In "Optimization of Hybrid Laminates with Extension-Shear coupling" by D. Cui and D. Li, the expressions of stiffness coefficient, thermal stress, and thermal moment for hybrid laminates were derived based on the geometrical factors of laminates, and the necessary and sufficient conditions for the hybrid extension-shear coupled laminates with immunity to hygrothermal shear distortion (HTSD) were further derived. The extension-shear coupled effect of hybrid laminates was optimized with improved differential evolution algorithm. Results were presented for hybrid laminates made of carbon fiber and glass fiber composite material. The hygrothermal effect and extension-shear coupled effect were simulated and verified, and the robustness of hybrid laminates was analyzed by Monte Carlo method.

In "Aeronautical and Aerospace Material and Structural Damages to Failures: Theoretical Concepts" by A. V. Goncharenko, the multioptionality hybrid function uncertainty conditional optimization was implemented for a degrading failure problem optimal solution determination. The principal supposition was that there should have been some certain objectively existing value extremized in the conditions of the hybrid-optional function uncertainty. The described doctrine allowed obtaining the objectively existing optimal values with the help of a not probabilistic rather multi-optimal concept. Applying simplified, however possible, models and expressions for effectiveness, plausible results were obtained, illustrated in diagrams, and allowed taking a good choice.

In "Analytical Study on Deformation and Structural Safety of Parafoil" by L. Wang and W. He, the cell bump distortion and bearing capacity of parafoil structure was analyzed. Based on the mechanical properties of the membrane structure, the spanwise model of parafoil inflation was established and verified by comparing with the fluid-structure interaction (FSI) results. The analytical model was proved to be useful for the weakening deformation design and the safety discussion of large parafoil for rocket booster recovery.

In "Effective Mechanical Property Estimation of Composite Solid Propellants Based on VCFEM" by L. Shen et al., the structural integrity of propellant grain was estimated by a numerical method that combines the Voronoi cell finite element method (VCFEM) and the homogenization method. The correctness of this combined method was validated by comparing with a standard finite element method and conventional theoretical models. The microscopic numerical analysis method proposed in this paper could also be used

to provide references for the design and the analysis of other large volume fraction composite materials.

In "Application of a Cohesive Zone Model for Simulating Fatigue Crack Growth from Moderate to High  $\Delta K$  Levels of Inconel 718" by H. Li et al., a cyclic cohesive zone model was applied to characterize the fatigue crack growth behavior of a IN718 superalloy which is frequently used in aerospace components. The gradual loss of the stress-bearing ability of the material was considered through the degradation of a novel cohesive envelope. The experimental data of cracked specimens were used to validate the simulation result. Based on the reasonable estimation for the model parameters, the fatigue crack growth from moderate to high  $\Delta K$  levels could be reproduced under the small-scale yielding condition, which was in fair agreement with the experimental results.

## Acknowledgments

The editors would like to express their thanks to all authors of the special issue for their valuable contributions and to all reviewers for their useful efforts to provide valuable reviews. We expect this special issue offers a timely view of advanced topics in structural behavior of advanced materials for aerospace, which will grant stimulation for further novel academic researches and innovative applications.

*Roberto G. Citarella  
Filippo Berto  
Paulo M. S. T. de Castro*

## Research Article

# Numerical-Experimental Assessment of a Hybrid FE-MB Model of an Aircraft Seat Sled Test

F. Caputo <sup>1</sup>, A. De Luca <sup>1</sup>, F. Marulo,<sup>2</sup> M. Guida <sup>2</sup> and B. Vitolo<sup>3</sup>

<sup>1</sup>Department of Engineering, University of Campania Luigi Vanvitelli, Aversa, Italy

<sup>2</sup>Department of Industrial Engineering, University of Naples "Federico II", Napoli, Italy

<sup>3</sup>Geven, Zona Asi Boscofangone, Nola, Napoli, Italy

Correspondence should be addressed to F. Caputo; francesco.caputo@unicampania.it

Received 9 March 2018; Accepted 12 June 2018; Published 1 August 2018

Academic Editor: Roberto G. Citarella

Copyright © 2018 F. Caputo et al. This is an open access article distributed under the Creative Commons Attribution License, which permits unrestricted use, distribution, and reproduction in any medium, provided the original work is properly cited.

This paper deals with the development of an established hybrid finite element multibody (FE-MB) model for the simulation of an experimental sled test of a single row of a double passenger seat placed in front of a fuselage bulkhead, by considering a single anthropomorphic Hybrid II 50th dummy arranged on one of the seat places. The numerical investigation has been carried out by focusing on the passenger passive safety. Specifically, the occupant injury assessment has been quantitatively monitored by means of the head injury criterion (HIC), which, based on the average value of the dummy head acceleration during a crash event, should not exceed, according to the standards, the value of 1000. Numerical results provided by the hybrid model have been compared with the experimental ones provided by the Geven S.p.A. company and with the results carried out by a full FE model. The hybrid model simulates with a good level of accuracy the experimental test and allows reducing significantly the computing time with respect to the full FE one.

## 1. Introduction

Nowadays, the importance of passive safety is becoming even more important for the transport field to the point of influencing the design practice [1–3]. In fact, several experimental and numerical studies are addressed to investigate and improve the crashworthiness of vehicles by paying attention to the passengers' safety. Compliance with the passive safety specifications leads to a little increase of the vehicle weight, which can be tolerated in view of an increasing of the chance of survival in case of an accident.

In the aerospace field, several components, such as the seat system, have been completely redesigned in order to improve the capability of the aircraft to protect passengers during crash events. As crash event, it must be intended, for example, an emergency landing.

The vehicle crashworthiness can be measured also in terms of the occupant injuries [4–12]. Among the several parameters that can be monitored, the head injury criterion (HIC) one plays a key role, denoting possible head injuries [13–18]. HIC parameter, based on the average value of the

passenger's head acceleration acting during a crash event, should be lower than 1000 in order to guarantee the passengers' safety. Another parameter is the maximum compressive load measured between the pelvis and the lumbar column of the anthropomorphic test dummy (ATD), which should not exceed 1500 lb (6.67 kN), or, if torso restraints are used, tension loads in individual straps should not exceed 1750 lb (7.78 kN) [1, 2].

Several experimental and numerical studies dealing with such matter have been proposed in literature: the former are characterized usually by destructive tests performed on such large instrumented full-scale structures such as aircraft, fuselage section, and seats, even equipped with ATDs, which cannot be easily repeated due to the high costs and the complexity of the tests, requiring often advanced laboratories, the use of complex acquisition sensor networks, complex and long result analysis, and so on. Concerning the numerical investigations, an established predictive numerical model can give a significant contribution in the assessment of passengers' safety, allowing to overcome all aforementioned issues related to experimental test. In particular, a numerical

tool gives also the possibility, under a certification by analysis (CBA) approach [19–22], to perform optimization analyses aimed to virtually achieve the optimal structural solution, decreasing the number of experimental tests and the costs required for the developmental phase. Concerning the disadvantages, numerical simulation of crash phenomena involving ATDs needs a high computational power. Moreover, the establishment of the model requires facing with the assessment of the assumed assumptions as well as hypotheses, the improvement of the level of accuracy, and consequently, the availability of high computational power.

This paper investigates on the passive safety addressed to the aircraft seat system.

A well-designed seat should allow passengers to not entrap themselves independently and escape the aircraft, by leading to good chance to survive, after a crash. Standards that investigate on the realistic dynamic performance of aircraft seats can be found in literature in order to emphasize occupant impact protection and to analyse the full-scale aircraft impact tests.

This paper deals with an improved hybrid finite element multibody (FE-MB) model for the simulation of an experimental sled test of a single row of a double passenger seat placed in front of a fuselage bulkhead by considering a single anthropomorphic dummy arranged on one of the seat places. Tests have been developed at the laboratory of Geven S.p.A., which is equipped with a sled decelerator testing system compliant with certification requirements from the FAR25 for TSO C127a regulations [1]. The development of the proposed numerical model started from a preliminary hybrid FE-MB model presented by authors in [23]. Specifically, the new modelling has been carried out in order to improve the level of accuracy of the predicted passenger kinematics. The hybrid modelling strategy has been carried out in order to exploit both FE method level of accuracy and the lower MB computational costs [23]. Whilst in the MB approach, which requires less computational costs, the dummy is modelled by rigid bodies, defined by both mass and moments of inertia (connected by suitable characteristics joints); in the FE approach, the dummy is modelled by means of finite elements containing more details than the former, which lead to several difficulties in terms of model management and higher computational costs.

In a seat sled test, all components, such as dummy, seat, and restraint system, may be modelled by means of both MB and FE approaches, leading to a less or more accurate simulation, respectively.

FE codes allow a very detailed modelling of all components, such as safety belts, dummies, and structural parts, by leading to very complex models, which are usually characterized by several million of degrees of freedom with negative feedback on the computing time and on the model versatility. In fact, the management of small design changes implies strong efforts in terms of modelling.

On the contrary, the MB method, to the detriment of a less level of accuracy related to the nondeformability of the modelled components, can be helpful for designers to simulate quickly the structural response of a structure under several configurations. More properly, MB methods lend mainly

themselves to the prediction of the kinematics of assembly components under complex loading conditions more than to the investigation of the stress-strain field.

As a matter of fact, this modelling method is widely used in a preliminary design stage where it is still interesting to investigate more structural solutions.

So in order to enjoy the accuracy of the FE method, as well as the low computational time provided by the MB method, the hybrid approach can be used, allowing improvement of the modelling where needed by means of the FE method as well as lowering the computational time. The lowering of the computational time can be achieved by considering the MB approach for the parts of the analysed system, whose deformations do not influence the dynamic system responses and for which only kinematic aspects must be taken into account.

In order to assess the prediction capability of the developed hybrid FE-MB model, the simulated biomechanical parameters, such as the acceleration of the head of the passenger, with the relative calculation of the head injury criterion (HIC) and the loads transmitted to his lower limbs have been compared with the experimental ones. Moreover, the predicted ATD trajectory has been compared with the trajectory simulated by a full FE model in previous papers [22, 23].

## 2. Experimental Dynamic Testing of Airplane Seats

The experimental test, provided by Geven S.p.A., is aimed to demonstrate the compliance of the seat passenger system with FAR 25.562 [1]. A Hybrid II 50th passenger dummy has been arranged on a double seat positioned in front of a relatively stiff bulkhead (Figure 1). The main parameter monitored during the test is the acceleration of the head, with the relative calculated HIC. The experimental test provided value of HIC higher than the limit one expressed in the standard. However, this aspect does not affect the purpose of determining a methodology for a numerical-experimental correlation.

The sled and passenger seat systems are launched at the prescribed speed against a steel bar deceleration system in order to reproduce the required simulation pulse. The resultant longitudinal deceleration over time is shown in Figure 2.

A dedicated test rig has been set up to reproduce the overall seat installation within the aircraft cabin. Prototype seat has been installed on the test sled with effective seat track. Proper seat belt installation required a test rig able to guarantee the correct position of aircraft/belt interface points with respect to the seat. Additionally, the test rig has been oversized in order to minimize the effects of any deformation occurring during the test.

*2.1. Hybrid FE-MB Model.* In a hybrid FE-MB model, the user diversifies the modelling, where possible, by integrating within the same solver rigid bodies with deformable finite element components, with the advantage of computing time reduction. The paper [23] reported an alternative strategy of simulation, named coupling, that as well as the hybrid one



FIGURE 1: Experimental test.

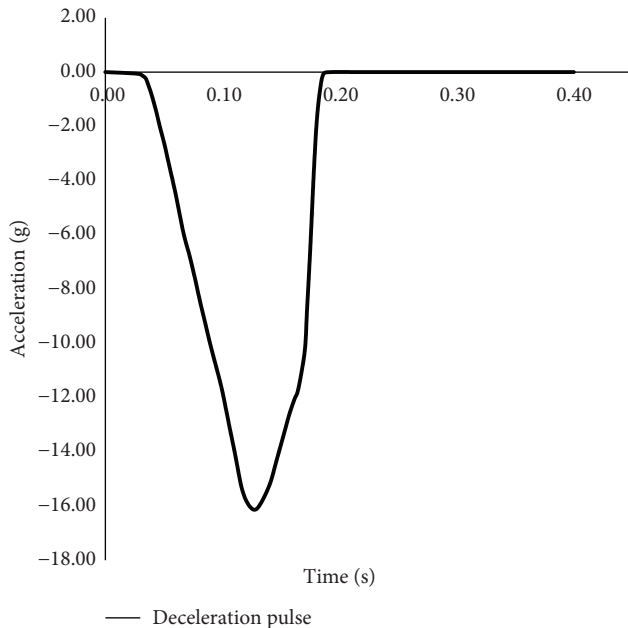


FIGURE 2: Resultant deceleration versus time curve characterizing the seat sled test.

gathers features and advantages of both FE and MB methods; according to this strategy, two separate solvers (one FEM and the other MB) work in parallel, exchanging information, and the connection between the software is represented by contact and constraint forces acting on the elements of the models. Generally, the effectiveness of these techniques lies in the combination of multibody versatility with finite element level of accuracy; these simulations are more flexible than full FEM. The hybrid method, contrary to the coupling approach, does not use an external FE code; for this reason, the computational costs are strongly reduced. Specifically, it has been assessed in a preliminary study [22, 23] that the simulation of the deformability of both seat and restraint system, which cannot be accomplished by means of the MB method, influences significantly the kinematics of the ATD during the seat sled test. This aspect can be empathised by comparing the ATD trajectory simulated by a full FE model (Figure 3(a)) with the trajectory simulated by a full MB one (Figure 3(b)). In fact, according to Figure 3(b), the ATD of the full MB model does not hit the bulkhead, unlike that of the full FEM (Figure 3(a)).

As a result, the modelling of the whole seat system by FEM, in the hybrid FE-MB model, appears to be the most efficient strategy to simulate the seat sled test. Consequently, the other parts, such as the ATD and the bulkhead, are modelled by means of rigid bodies according to the MB approach to reduce the computing time.

The improvement of this hybrid FE-MB model with respect to the one presented by authors in [23] lies in a different setup of the kinematic joints of the MB components. The interconnection structure of a multibody system depends strictly on the definition of the kinematic joints. The equations of motion (Newton-Euler) (1 and 2) of a rigid body, referred to its centre of gravity, are

$$m_i \ddot{r}_i = F_i, \quad (1)$$

$$J_i \cdot \dot{\omega}_i + \omega_i \times J_i \cdot \omega_i = T_i, \quad (2)$$

where  $m_i$  is the mass,  $J_i$  is the inertia tensor with respect to the centre of gravity,  $\omega_i$  is the angular velocity vector,  $F_i$  is the resultant force vector, and  $T_i$  is the resultant torque vector relative to the centre of gravity. For each body,  $F_i$  and  $T_i$  include the constraint forces and torques due to joints which cannot be determined until the acceleration of the system is known, in contrast with all other forces and torques which depend only on position and velocity quantities. Equations (2) and (3) are multiplied by a variation of the position vector,  $\delta r_i$ , and a variation of the orientation,  $\delta \pi_i$ , and the resulting equations are summed for all bodies of the system.

$$\sum \delta r_i \cdot \{m_i \ddot{r}_i - F_i\} + \delta \pi_i \cdot \{J_i \cdot \dot{\omega}_i + \omega_i \times J_i \cdot \omega_i - T_i\} = 0. \quad (3)$$

When the variations  $\delta r_i$  and  $\delta \pi_i$  of connected bodies are such that the constraints caused by the joint are not violated, the constraint forces and torques in joints will cancel.

The model has been developed within the TNO Madymo® software [24, 25] environment (Figure 4), which contains both MB and FE solvers. In the finite element module, solid hexa, penta, 1D beam, and shell elements can be chosen. However, since the Madymo is a native MB code, the FE module is not characterized by the same accuracy of other native FE codes, especially for 3D finite elements. Hence, in order to improve the precision of the simulations, it has been preferred to model the whole seat by means of shell element type for a total of 105,226 elements and 151,219 nodes.

The modelling of inertial properties of the seat system has been guaranteed by the definition of both materials' density and thickness for each shell element.

The adopted hybrid approach allows the use of different integration methods for the equations of motion for both FE and MB modules. For short-duration crash analyses, explicit integration methods are preferred.

The hybrid approach is in any case based on the assumptions that the parts considered rigid do not influence the behaviour of deformable parts [7]. The deceleration pulse (Figure 2) has been applied to the seat fixed to the slide, along the seat sled test longitudinal direction as shown in Figure 4. Gravity and initial velocity have been applied to all parts of the model. The test case selected for the experimental test consists of a metallic double seat, fabricated from aluminium 2024-T351 and 7075-T651 components. Cushions are made of foam material [26], which constitutive law has been shown in Figure 5 in true stress-strain. For each material, an elastic-plastic model has been selected.

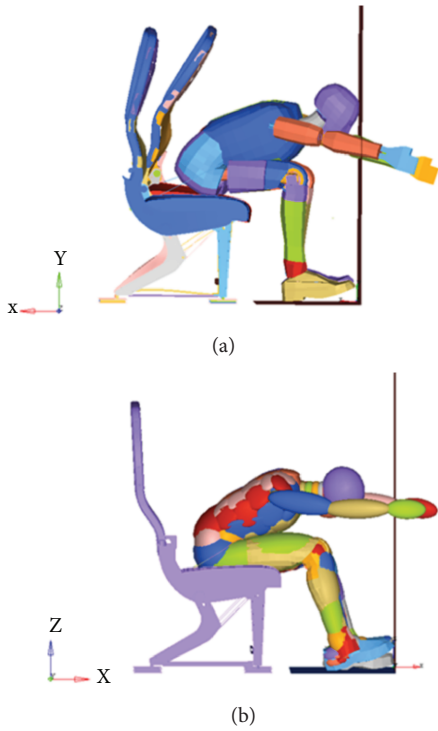


FIGURE 3: Full FE (a) and full MB (b) models.



FIGURE 4: Hybrid model.

### 3. Results and Discussion

To assess the reliability of the proposed hybrid model, the head resultant acceleration has been numerically and experimentally monitored, allowing consequently the calculation of the experimental and predicted HIC values.

The numerical and experimental frames corresponding to the instant of time in which the ATD head hits the bulk-head are shown in Figure 6. According to Figure 6, it is possible to observe that the seat deformation (Figure 6(a)) is in good agreement with the predicted one (Figure 6(b)).

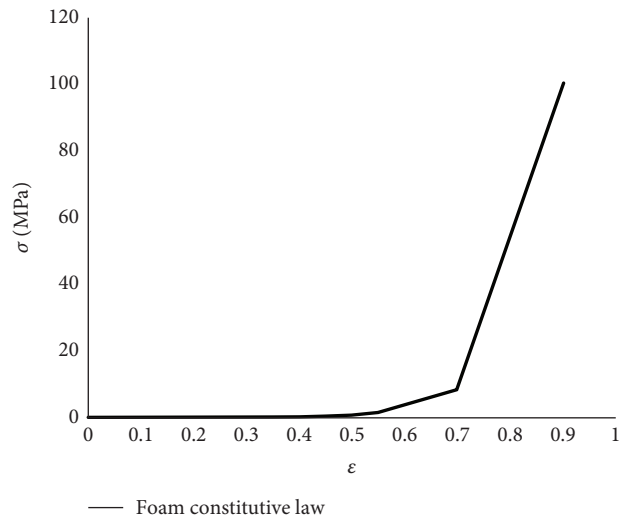


FIGURE 5: Foam constitutive curve.



(a)

Hybrid FEM/MB  
Loadcase 1 : time = 0.175000  
Frame 36



(b)

FIGURE 6: Experimental test (a) and hybrid model (b).

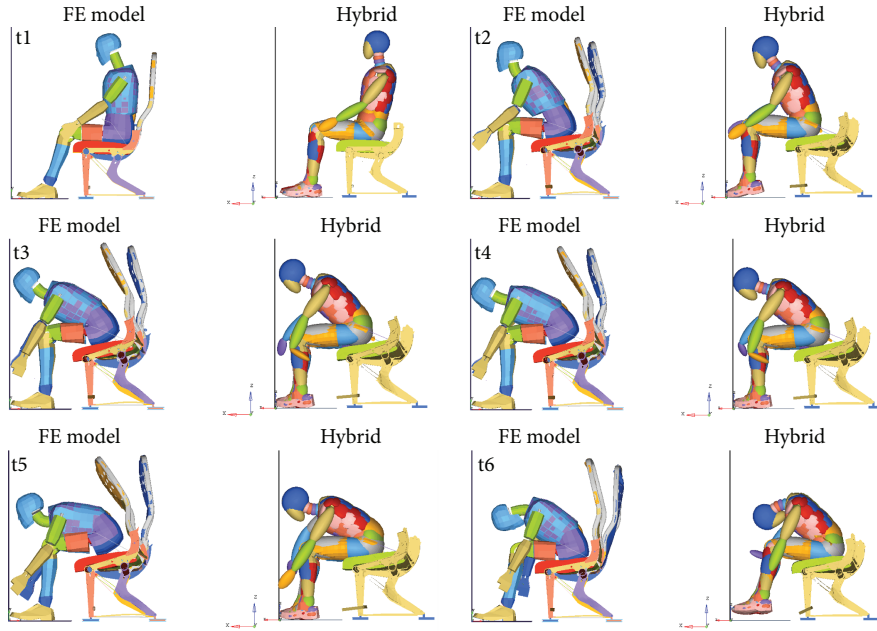


FIGURE 7: Full FE and hybrid model results.

Moreover, results of the hybrid model have been compared to those predicted by the full FE model presented by the authors in [22, 23]. Some numerical frames extracted by both full FE and hybrid models have been compared in Figure 7.

Figure 7 shows a good correlation in terms of seat system and ATD kinematics.

Moreover, the predicted head path, induced mainly by the effects of the deformation on the seat frame, has been compared with the experimental one in Figure 8.

According to Figure 8, a good level of accuracy can be noticed.

Concerning the head resultant accelerations, Figure 9 compares results provided by the experimental and numerical investigations. Acceleration versus time curves have been filtered with SAE filter 1000 [27]. For a better comparison, the numerical curves have been shifted a few milliseconds to make sure that their maximum occurs at the same instant as that of the experimental one.

From Figure 9, it can be noticed that even if all predicted acceleration peaks are well-predicted, the same cannot be said for HIC values. Specifically, HIC value carried out by the full FE simulation is significantly higher than the ones provided by the experimental test and hybrid model. The full FE overestimation can be attributed to the fact that HIC value is calculated by (4), which considers mainly the area under the full FE acceleration versus time curve larger than the other ones.

$$\text{HIC} = \max \left\{ (t_2 - t_1) \left[ \frac{1}{(t_2 - t_1)} \int_{t_1}^{t_2} a(t) dt \right]^{2.5} \right\}, \quad (4)$$

where  $a(t)$  is the resultant head acceleration measured in  $g$  and  $t_1$  and  $t_2$  are the extremes of the integration interval

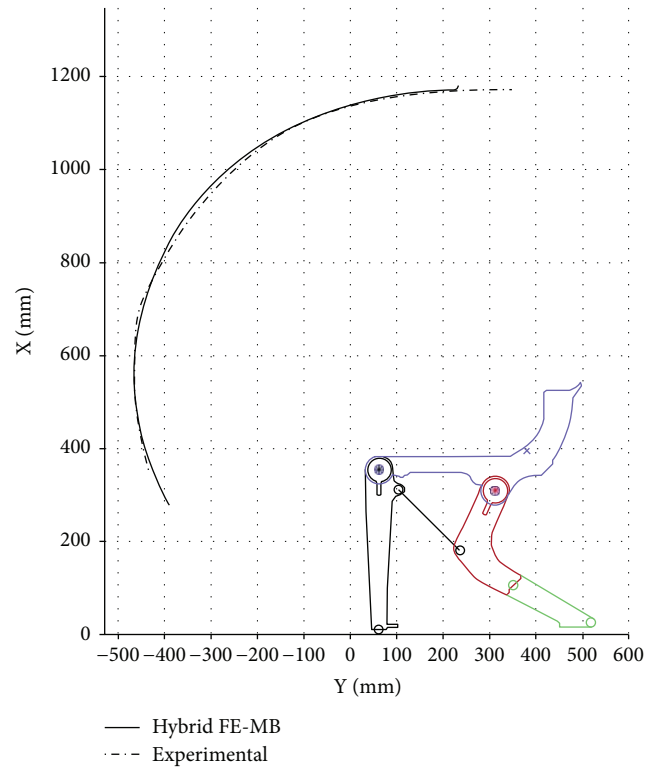


FIGURE 8: Head path correlation.

containing the head acceleration peak measured in seconds for the HIC calculation.

It is very important to emphasize that the computational time of the numerical simulations are about 20 hours for the full FE simulation and about 2 hours for the hybrid one.

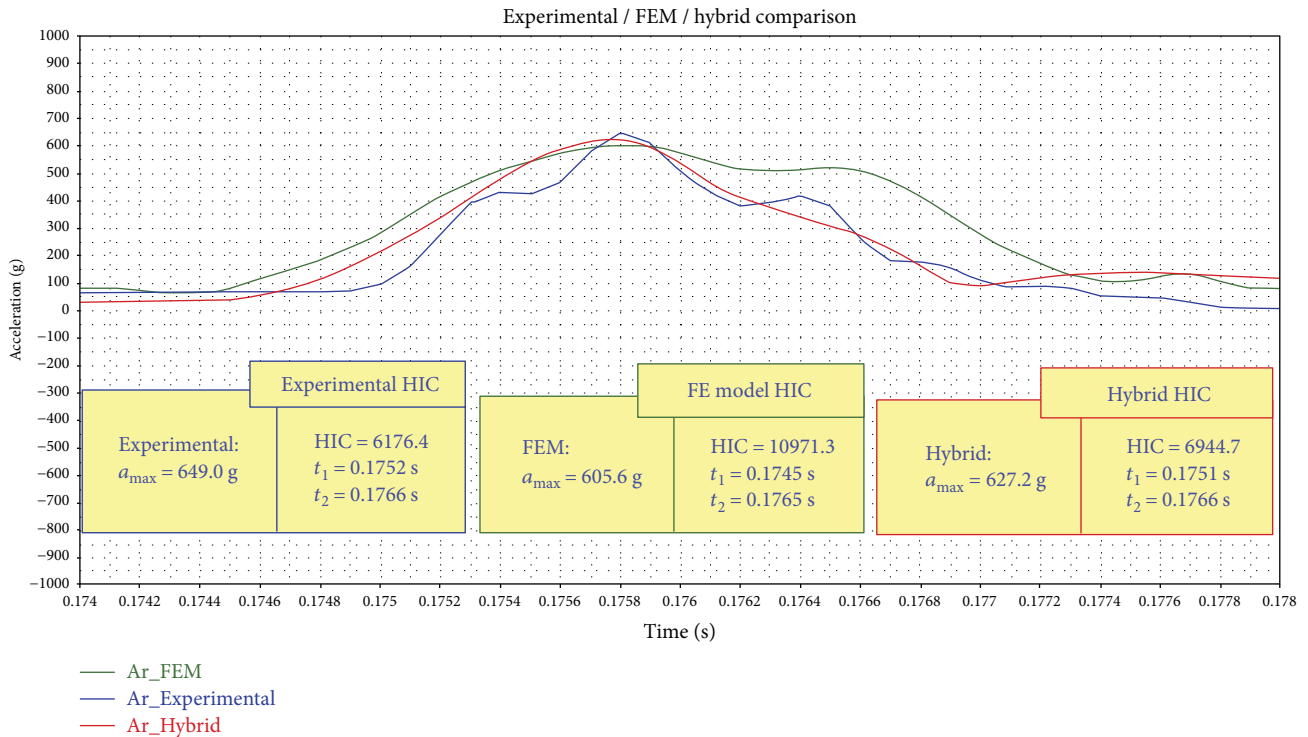


FIGURE 9: Head resultant accelerations.

#### 4. Conclusions

In this paper, a hybrid FE-MB model has been developed, and its reliability has been assessed against the experimental test results provided by the Geven S.p.A. company and the numerical results carried out by a full FE simulation, presented by the authors in previous papers [22, 23]. The hybrid model allowed simulating the seat sled test, reducing significantly the computational costs with respect to those requested by a full FE strategy and at the same time improving the level of accuracy that can be achieved by a full MB model which does not permit the modelling of the deformability of the seat system. As a result, the hybrid approach is a good solution to exploit both FE accuracy and MB lower computing time.

The performed numerical-experimental result correlation demonstrates the efficiency of the proposed hybrid model in simulating the phenomenon. Moreover, the correlation of the numerical results achieved by the hybrid model with the results carried out by the full FE simulation showed that the former is also able to simulate the kinematics of both seat and dummy during the crash event.

#### Data Availability

The data used to support the findings of this study are available from the corresponding author upon request.

#### Conflicts of Interest

The authors declare that there are no conflicts of interest regarding the publication of this paper.

#### Acknowledgments

The research activity has been developed within IMM (Interiors with Multifunctional Materials) Research Project funded by Regione Campania, Italy.

#### References

- [1] Federal Aviation Regulation FAR 25.562, "Emergency landing dynamic conditions," in *Federal Aviation Regulation*, Federal Aviation Administration FAA, 2006.
- [2] National Aerospace Standards - NAS 809, *Specification - Aircraft Seats and Berths*.
- [3] Federal Aviation Regulation, *Dynamic Evaluation of Seat Restraint Systems and Occupant Protection on Transport Airplanes*, Federal Aviation Administration, 2006.
- [4] N. Dhole, V. Yadav, and G. Olivares, *Certification by Analysis of a Typical Aircraft Seat*, National Institute for Aviation Research, Wichita, Kansas, 2012.
- [5] P. Bhonge, *A Methodology for Aircraft Seat Certification by Dynamic Finite Element Analysis*, Department of Mechanical Engineering, Wichita State University, 2008.
- [6] T. M. Hermann, M. W. Holmes, and D. Hartley, "Development of a dynamic aircraft seat analysis capability," in *SAE Technical Paper Series*, September 2001.
- [7] J. S. Ruan, C. Zhou, T. B. Khalil, and A. I. King, *Techniques and Applications of Finite Element Analysis of the Biomechanical Response of the Human Head to Impact*, CRC Press LLC, 2001.
- [8] R. Happee, A. Janssen, E. Fraterman, and J. Monster, "Application of MADYMO occupant models in DYNA/MADYMO coupling," in *4th European LS-DYNA Users Conference*, Ulm, Germany, 2003.

- [9] H. Boucher and C. D. Waagmeester, "Enhanced FAA-HYBRID III numerical dummy model in MADYMO for aircraft occupant safety assessment," in *SAE Technical Paper Series*, September 2003.
- [10] H. J. Mertz, P. Prasad, and G. Nusholtz, "Head injury risk assessment for forehead impacts," in *SAE Technical Paper Series*, February 1996.
- [11] J. S. H. M. Wismans, *Injury Biomechanics*, Eindhoven University of Technology, Division of Fundamentals (WFW), 1994.
- [12] D. H. Laananen, "Crashworthiness analysis of commuter aircraft seats and restraint systems," *Journal of Safety Research*, vol. 22, no. 2, pp. 83–95, 1991.
- [13] SAE Aerospace Standard AS8049B, *Performance Standard for Seats in Civil Rotorcraft, Transport Aircraft, and General Aviation Aircraft*, 2005.
- [14] Federal Aviation Administration, "Advisory Circular 25.562-1B," *Dynamic Evaluation of Seat, Restraint Systems and Occupant Protection on Transport Airplanes*, 2006.
- [15] Federal Aviation Regulation, *Methodology for Dynamic Seat Certification by Analysis for Use in Parts 23, 25, 27, and 29 Airplanes and Rotorcraft*, U.S. Department of Transportation, 2003.
- [16] P. Prasad and H. J. Mertz, "The position of the United States Delegation to the ISO Working Group 6 on the use of HIC in the automotive environment," in *SAE Technical Paper Series*, June 1985.
- [17] C. D. Waagmeester, E. Hassel, and C. G. Huijskens, "Design optimization and evaluation of a three point harness seat design for airbus A320 aircraft family," in *The Fourth Triennial International Aircraft Fire and Cabin Safety Research Conference*, November 2004.
- [18] C. Olschinka and A. Schumacher, "Dynamic simulation of flight passenger seats," in *Proceeding of the 5th LS-DYNA Anwenderforum*, Ulm, October 2006.
- [19] H. Lankarani and P. Bhone, "Finite element modelling strategies for dynamic aircraft seats," in *SAE Technical Paper Series*, August 2008.
- [20] H. Gaber, D. Browen, and C. Molnar, "Modelling of commuter category aircraft seat," in *U.S. Department of Transportation*, 2004.
- [21] J. Christl, S. Kunz, P. Bayrasy, I. Kalmykov, and J. Kleinert, "FEA-MBS-coupling approach for vehicle dynamics," in *Proceedings of 2nd European Conference on Coupled MBS-FE Applications*, pp. 29–32, Pembroke, Ontario, October 2015.
- [22] M. Guida, A. Manzoni, A. Zuppari, F. Caputo, F. Marulo, and A. De Luca, "Development of a multibody system for crashworthiness certification of aircraft seat," *Multibody System Dynamics*, 2018.
- [23] F. di Napoli, A. De Luca, F. Caputo, F. Marulo, M. Guida, and B. Vitolo, "Mixed FE-MB methodology for the evaluation of passive safety performances of aeronautical seats," *International Journal of Crashworthiness*, pp. 1–12, 2018.
- [24] TASS BV, *MADYMO Reference Manual Version 7.5*, 2013.
- [25] TASS BV, *MADYMO Coupling Manual Version 7.5*, 2013.
- [26] "Development of a seat cushion replacement component test method for dynamically certified seat," 2001, AGATE report, C-GEN-3433B-1 (Rev N/C).
- [27] Society of Automotive Engineers, *Recommended Practice: Instrumentation for Impact Test - Part I*, Electronic Instrumentation, SAE J211/1, 1995.

## Research Article

# Optimization of Hybrid Laminates with Extension-Shear Coupling

Da Cui  and Daokui Li 

*College of Aerospace Science and Engineering, National University of Defense Technology, Changsha 410073, China*

Correspondence should be addressed to Daokui Li; [lidaokui@nudt.edu.cn](mailto:lidaokui@nudt.edu.cn)

Received 25 February 2018; Revised 11 April 2018; Accepted 17 April 2018; Published 27 May 2018

Academic Editor: Roberto G. Citarella

Copyright © 2018 Da Cui and Daokui Li. This is an open access article distributed under the Creative Commons Attribution License, which permits unrestricted use, distribution, and reproduction in any medium, provided the original work is properly cited.

The introduction of hybrid composites into the structure with coupling effect can greatly reduce the cost of materials. The expressions of stiffness coefficient, thermal stress, and thermal moment for hybrid laminates are derived based on the geometrical factors of laminates, and the necessary and sufficient conditions for the hybrid extension-shear-coupled laminates with immunity to hygrothermal shear distortion (HTSD) are further derived. The extension-shear-coupled effect of hybrid laminates is optimized with improved differential evolution algorithm. Results are presented for the hybrid laminates that consist of carbon fiber and glass fiber composite materials. The hygrothermal effect and extension-shear-coupled effect are simulated and verified, meanwhile the robustness of hybrid laminates is analyzed by Monte Carlo method.

## 1. Introduction

Laminated composites are playing an important and irreplaceable role in designing structures with coupling effect. For example, the bending-twisting-coupled wing structure can be designed by using composite extension-shear-coupled laminates [1] and the bending-twisting-coupled wind turbine blades structure can be designed by using composite extension-twisting-coupled laminates [2]. However, with the large-scale use of these bending-twisting coupling structures, the common glass fiber composites have difficulties in meeting the requirements of structural reliability. On the other hand, the carbon fiber composites with good comprehensive properties [3, 4] cost about ten times more than glass fiber composites, which restricts its wide range of applications. Therefore, it is necessary to introduce hybrid fiber composites into the design of the bending-twisting-coupled structure to achieve the purpose that greatly reduces material cost under meeting the structural reliability requirements.

According to different hybrid modes, hybrid fiber composites are mainly divided into two types of composites, the in-layer composites and between-layer composites [5]. The in-layer hybrid composites consist of two or more fibers

which uniformly dispersed in the same matrix of the lamina; the between-layer hybrid composites are composed of two or more different laminae which consist of different single-fiber composites. In this paper, the bending-twisting-coupled structure is designed by between-layer hybrid laminates.

At present, the widely used materials in the study of the bending-twisting coupled structure are the single-fiber composite laminates [6–10], whose important design parameters contain paving angles merely. However, the important design parameters for hybrid laminates also include the paving materials [11]. Once the paving materials become variable, the design of laminates becomes more complicated and the number of optimization constraints even multiplies at the same time.

J. Li and D. Li [2] have designed a kind of single-fiber composite laminates with immunity to hygrothermal shear distortion (HTSD) with only extension-shear-coupled effect—the  $A_F B_0 D_S$  laminates (refer to the nomenclature of references [1, 2])—and the sequential quadratic programming (SQP) is used to optimize its coupled effect. However, we found that feasible solutions cannot be found when using the SQP algorithm to optimize the hybrid  $A_F B_0 D_S$  laminates with immunity to HTSD, for this algorithm cannot meet the strong constraints of hybrid laminates. Therefore, this paper

takes the improved differential evolution algorithm DE\_CMSBHS to optimize this problem.

The DE\_CMSBHS algorithm is an efficient global optimization algorithm, which has the characteristics of simple structure, easy realization, fast convergence, and strong robustness, and can effectively solve the single-objective optimization problems such as integer problems, real problems, and mixed integer-real problems [12]. The single-objective nonlinear optimization problems are able to be solved well by combining the penalty function's ability to handle constraints with the optimal performance of DE\_CMSBHS algorithm [13, 14]. The optimization problem of hybrid  $\mathbf{A}_F\mathbf{B}_0\mathbf{D}_S$  laminates with immunity to HTSD is a typical nonlinear mixed integer-real single-objective optimization problem.

In this paper, the model of hybrid laminates is firstly established. Then the expressions of stiffness coefficient, thermal stress, and thermal moment for laminates are derived with important parameter geometric factor [15, 16]. Secondly, the necessary and sufficient conditions for the hybrid extension-shear-coupled laminates with immunity to HTSD are derived. Thirdly, the DE\_CMSBHS algorithm combined with the penalty function is used to optimize the extension-shear-coupled effect of hybrid laminates with immunity to HTSD. Finally, the mechanical properties of optimized laminates are verified.

## 2. Stiffness Coefficient, Thermal Stress, and Thermal Moment of Hybrid Laminates

Introducing the geometrical factors into the design of laminates can effectively improve the efficiency of this progress. In this section, the model of hybrid laminates will be established. Based on the geometric factors, the expressions of stiffness coefficient, thermal stress, and thermal moment of hybrid laminates are derived.

The research object is set as a kind of hybrid laminates which are composed of two different types of lamina, and each lamina has the same thickness, as shown in Figure 1. Wherein,  $z_k$  is the position of the  $k$ -ply in the entire laminates,  $n$  is the number of plies of the laminates, and  $H$  is the entire thickness of the laminates. ① and ② represent two kinds of laminae with different material properties, respectively, and the number and layer order of each kind of lamina are variables.

**2.1. Stiffness Coefficient.** The off-axis stiffness coefficients of the  $k$ -ply in the entire hybrid laminates can be defined as

$$\begin{aligned} (\bar{Q}_{11})_k &= U_1^q + U_2^q \cos 2\theta_k + U_3^q \cos 4\theta_k, \\ (\bar{Q}_{12})_k &= -U_3^q \cos 4\theta_k + U_4^q, \\ (\bar{Q}_{16})_k &= \frac{U_2^q}{2} \sin 2\theta_k + U_3^q \sin 4\theta_k, \\ (\bar{Q}_{22})_k &= U_1^q - U_2^q \cos 2\theta_k + U_3^q \cos 4\theta_k, \\ (\bar{Q}_{26})_k &= \frac{U_2^q}{2} \sin 2\theta_k - U_3^q \sin 4\theta_k, \\ (\bar{Q}_{66})_k &= -U_3^q \cos 4\theta_k + U_5^q. \end{aligned} \quad (1)$$

Wherein,  $\theta_k$  is the paving angle of the  $k$ -ply of the laminates. The superscript “ $q$ ” is defined to mean which kind of lamina corresponds to:  $q = \textcircled{1}$  implies that the lamina corresponds to the type ① lamina and  $q = \textcircled{2}$  implies that the lamina corresponds to the type ② lamina. Moreover,  $U_i^q (i = 1, 2, \dots, 5)$  are the material constants of hybrid laminates, which are only related to the material parameters of the laminae, as shown in

$$\begin{aligned} U_1^q &= \frac{(3Q_{11}^q + 3Q_{22}^q + 2Q_{12}^q + 4Q_{66}^q)}{8}, \\ U_2^q &= \frac{(Q_{11}^q - Q_{22}^q)}{2}, \\ U_3^q &= \frac{(Q_{11}^q + Q_{22}^q - 2Q_{12}^q - 4Q_{66}^q)}{8}, \\ U_4^q &= \frac{(Q_{11}^q + Q_{22}^q + 6Q_{12}^q - 4Q_{66}^q)}{8}, \\ U_5^q &= \frac{(Q_{11}^q + Q_{22}^q - 2Q_{12}^q + 4Q_{66}^q)}{8} \\ &= \frac{1}{2}(U_1^q - U_4^q). \end{aligned} \quad (2)$$

In which,  $Q_{ij}^q$  are the stiffness coefficients of two types of lamina. The geometric factors  $\xi_j^q (j = 1, 2, \dots, 15, q = \textcircled{1}, \textcircled{2})$  of hybrid laminates, which are convenient to express the stiffness matrices, are defined as

$$\begin{aligned} (\xi_1^q \xi_2^q \xi_3^q \xi_4^q) &= \sum_{k=q} (\cos 2\theta_k \quad \cos 4\theta_k \quad \sin 2\theta_k \quad \sin 4\theta_k) \\ &\quad \cdot (z_k - z_{k-1}), \\ (\xi_5^q \xi_6^q \xi_7^q \xi_8^q) &= \sum_{k=q} (\cos 2\theta_k \quad \cos 4\theta_k \quad \sin 2\theta_k \quad \sin 4\theta_k) \\ &\quad \cdot (z_k^2 - z_{k-1}^2), \\ (\xi_9^q \xi_{10}^q \xi_{11}^q \xi_{12}^q) &= \sum_{k=q} (\cos 2\theta_k \quad \cos 4\theta_k \quad \sin 2\theta_k \quad \sin 4\theta_k) \\ &\quad \cdot (z_k^3 - z_{k-1}^3), \\ (\xi_{13}^q \xi_{14}^q \xi_{15}^q) &= \sum_{k=q} [(z_k - z_{k-1}) \quad (z_k^2 - z_{k-1}^2) \quad (z_k^3 - z_{k-1}^3)], \end{aligned} \quad (3)$$

where  $k = q$  means the sum of all the type ① or ② laminae on the right side of the equation. Obviously, the geometric factors are only related to the paving angle and location of each lamina.

**2.1.1. Extension Stiffness Matrix  $\mathbf{A}$ .** According to the classical theory of laminates, the extension stiffness matrix of laminates can be expressed as

$$\mathbf{A}_{ij} = \sum_{k=1}^n (\bar{Q}_{ij})_k (z_k - z_{k-1}), \quad i, j = 1, 2, 6. \quad (4)$$

Substituting (1), (2), and (3) into (4) can be used to obtain the expressions of the extension stiffness coefficients, which

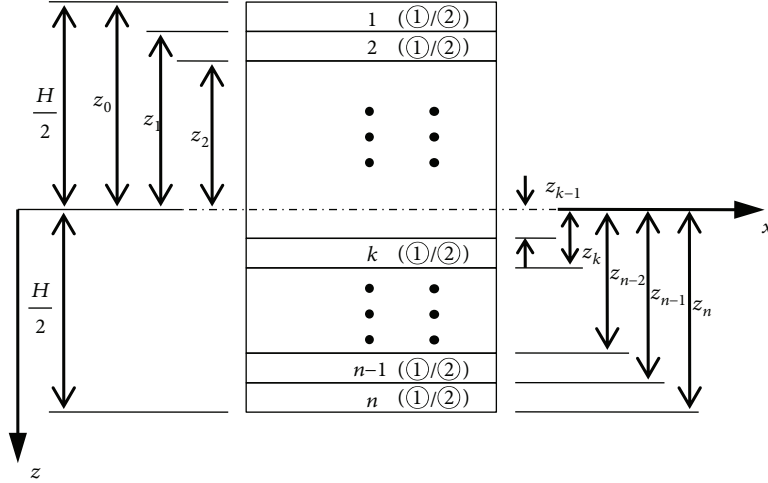


FIGURE 1: Model of hybrid laminates.

are only related to the material constants and geometric factors, as shown in

$$\begin{aligned}
 \mathbf{A}_{11} &= \sum_{k=1}^n (U_1^q + U_2^q \cos 2\theta_k + U_3^q \cos 4\theta_k) (z_k - z_{k-1}) \\
 &= U_1^{\ominus} \xi_{13}^{\ominus} + U_2^{\ominus} \xi_{51}^{\ominus} + U_3^{\ominus} \xi_{52}^{\ominus} + U_1^{\ominus} \xi_{13}^{\ominus} + U_2^{\ominus} \xi_{51}^{\ominus} + U_3^{\ominus} \xi_{52}^{\ominus}, \\
 \mathbf{A}_{12} = \mathbf{A}_{21} &= \sum_{k=1}^n [(-\cos 4\theta_k) U_3^q + U_4^q] (z_k - z_{k-1}) \\
 &= -U_3^{\ominus} \xi_{52}^{\ominus} + U_4^{\ominus} \xi_{13}^{\ominus} - U_3^{\ominus} \xi_{52}^{\ominus} + U_4^{\ominus} \xi_{13}^{\ominus}, \\
 \mathbf{A}_{16} = \mathbf{A}_{61} &= \sum_{k=1}^n \left[ U_2^q \left( \frac{\sin 2\theta_k}{2} \right) + U_3^q \sin 4\theta_k \right] (z_k - z_{k-1}) \\
 &= \frac{1}{2} U_2^{\ominus} \xi_{53}^{\ominus} + U_3^{\ominus} \xi_{54}^{\ominus} + \frac{1}{2} U_2^{\ominus} \xi_{53}^{\ominus} + U_3^{\ominus} \xi_{54}^{\ominus}, \\
 \mathbf{A}_{22} &= \sum_{k=1}^n (U_1^q - U_2^q \cos 2\theta_k + U_3^q \cos 4\theta_k) (z_k - z_{k-1}) \\
 &= U_1^{\ominus} \xi_{13}^{\ominus} - U_2^{\ominus} \xi_{51}^{\ominus} + U_3^{\ominus} \xi_{52}^{\ominus} + U_1^{\ominus} \xi_{13}^{\ominus} - U_2^{\ominus} \xi_{51}^{\ominus} + U_3^{\ominus} \xi_{52}^{\ominus}, \\
 \mathbf{A}_{26} = \mathbf{A}_{62} &= \sum_{k=1}^n \left[ U_2^q \left( \frac{\sin 2\theta_k}{2} \right) - U_3^q \sin 4\theta_k \right] (z_k - z_{k-1}) \\
 &= \frac{1}{2} U_2^{\ominus} \xi_{53}^{\ominus} - U_3^{\ominus} \xi_{54}^{\ominus} + \frac{1}{2} U_2^{\ominus} \xi_{53}^{\ominus} - U_3^{\ominus} \xi_{54}^{\ominus}, \\
 \mathbf{A}_{66} &= \sum_{k=1}^n (-U_3^q \cos 4\theta_k + U_5^q) (z_k - z_{k-1}) \\
 &= -U_3^{\ominus} \xi_{52}^{\ominus} + U_5^{\ominus} \xi_{13}^{\ominus} - U_3^{\ominus} \xi_{52}^{\ominus} + U_5^{\ominus} \xi_{13}^{\ominus}.
 \end{aligned} \tag{5}$$

2.1.2. *Coupling Stiffness Matrix B.* Similarly, the coupling stiffness matrix of the hybrid laminates can be expressed as

$$\mathbf{B}_{ij} = \sum_{k=1}^n (\bar{Q}_{ij})_k (z_k^2 - z_{k-1}^2), \quad i, j = 1, 2, 6. \tag{6}$$

Substituting (1), (2), and (3) into (6) can be used to obtain the expression of the coupling stiffness coefficients, which are only related to the material constants and geometric factors, as shown in

$$\begin{aligned}
 \mathbf{B}_{11} &= \frac{1}{2} \sum_{k=1}^n (U_1^q + U_2^q \cos 2\theta_k + U_3^q \cos 4\theta_k) (z_k^2 - z_{k-1}^2) \\
 &= \frac{1}{2} U_1^{\ominus} \xi_{14}^{\ominus} + \frac{1}{2} U_2^{\ominus} \xi_{55}^{\ominus} + \frac{1}{2} U_3^{\ominus} \xi_{56}^{\ominus} + \frac{1}{2} U_1^{\ominus} \xi_{14}^{\ominus} \\
 &\quad + \frac{1}{2} U_2^{\ominus} \xi_{55}^{\ominus} + \frac{1}{2} U_3^{\ominus} \xi_{56}^{\ominus}, \\
 \mathbf{B}_{12} = \mathbf{B}_{21} &= \frac{1}{2} \sum_{k=1}^n [(-\cos 4\theta_k) U_3^q + U_4^q] (z_k^2 - z_{k-1}^2) \\
 &= -\frac{1}{2} U_3^{\ominus} \xi_{56}^{\ominus} + \frac{1}{2} U_4^{\ominus} \xi_{14}^{\ominus} - \frac{1}{2} U_3^{\ominus} \xi_{56}^{\ominus} + \frac{1}{2} U_4^{\ominus} \xi_{14}^{\ominus}, \\
 \mathbf{B}_{22} &= \frac{1}{2} \sum_{k=1}^n (U_1^q - U_2^q \cos 2\theta_k + U_3^q \cos 4\theta_k) (z_k^2 - z_{k-1}^2) \\
 &= \frac{1}{2} U_1^{\ominus} \xi_{14}^{\ominus} - \frac{1}{2} U_2^{\ominus} \xi_{55}^{\ominus} + \frac{1}{2} U_3^{\ominus} \xi_{56}^{\ominus} + \frac{1}{2} U_1^{\ominus} \xi_{14}^{\ominus} - \frac{1}{2} U_2^{\ominus} \xi_{55}^{\ominus} \\
 &\quad + \frac{1}{2} U_3^{\ominus} \xi_{56}^{\ominus}, \\
 \mathbf{B}_{16} = \mathbf{B}_{61} &= \frac{1}{2} \sum_{k=1}^n \left[ U_2^q \left( \frac{\sin 2\theta_k}{2} \right) + U_3^q \sin 4\theta_k \right] (z_k^2 - z_{k-1}^2) \\
 &= \frac{1}{4} U_2^{\ominus} \xi_{57}^{\ominus} + \frac{1}{2} U_3^{\ominus} \xi_{58}^{\ominus} + \frac{1}{4} U_2^{\ominus} \xi_{57}^{\ominus} + \frac{1}{2} U_3^{\ominus} \xi_{58}^{\ominus}, \\
 \mathbf{B}_{26} = \mathbf{B}_{62} &= \frac{1}{2} \sum_{k=1}^n \left[ U_2^q \left( \frac{\sin 2\theta_k}{2} \right) - U_3^q \sin 4\theta_k \right] (z_k^2 - z_{k-1}^2) \\
 &= \frac{1}{4} U_2^{\ominus} \xi_{57}^{\ominus} - \frac{1}{2} U_3^{\ominus} \xi_{58}^{\ominus} + \frac{1}{4} U_2^{\ominus} \xi_{57}^{\ominus} - \frac{1}{2} U_3^{\ominus} \xi_{58}^{\ominus}, \\
 \mathbf{B}_{66} &= \frac{1}{2} \sum_{k=1}^n (-U_3^q \cos 4\theta_k + U_5^q) (z_k^2 - z_{k-1}^2) \\
 &= -\frac{1}{2} U_3^{\ominus} \xi_{56}^{\ominus} + \frac{1}{2} U_5^{\ominus} \xi_{14}^{\ominus} - \frac{1}{2} U_3^{\ominus} \xi_{56}^{\ominus} + \frac{1}{2} U_5^{\ominus} \xi_{14}^{\ominus}.
 \end{aligned} \tag{7}$$

2.1.3. *Bending Stiffness Matrix D.* The bending stiffness matrix of the hybrid laminates can be expressed as

$$\mathbf{D}_{ij} = \sum_{k=1}^n (\bar{Q}_{ij})_k (z_k^3 - z_{k-1}^3), \quad i, j = 1, 2, 6. \quad (8)$$

Substituting (1), (2), and (3) into (8) can be used to obtain the expressions of the bending stiffness coefficients, which are only related to the material constants and geometric factors, as shown in

$$\begin{aligned} \mathbf{D}_{11} &= \frac{1}{3} \sum_{k=1}^n (U_1^q + U_2^q \cos 2\theta_k + U_3^q \cos 4\theta_k) (z_k^3 - z_{k-1}^3) \\ &= \frac{1}{3} U_1^{\textcircled{1}} \xi_{15}^{\textcircled{1}} + \frac{1}{3} U_2^{\textcircled{1}} \xi_9^{\textcircled{1}} + \frac{1}{3} U_3^{\textcircled{1}} \xi_{10}^{\textcircled{1}} + \frac{1}{3} U_1^{\textcircled{2}} \xi_{15}^{\textcircled{2}} + \frac{1}{3} U_2^{\textcircled{2}} \xi_9^{\textcircled{2}} \\ &\quad + \frac{1}{3} U_3^{\textcircled{2}} \xi_{10}^{\textcircled{2}}, \end{aligned}$$

$$\begin{aligned} \mathbf{D}_{12} = \mathbf{D}_{21} &= \frac{1}{3} \sum_{k=1}^n [(-\cos 4\theta_k) U_3^q + U_4^q] (z_k^3 - z_{k-1}^3) \\ &= -\frac{1}{3} U_3^{\textcircled{1}} \xi_{10}^{\textcircled{1}} + \frac{1}{3} U_4^{\textcircled{1}} \xi_{15}^{\textcircled{1}} - \frac{1}{3} U_3^{\textcircled{2}} \xi_{10}^{\textcircled{2}} + \frac{1}{3} U_4^{\textcircled{2}} \xi_{15}^{\textcircled{2}}, \end{aligned}$$

$$\begin{aligned} \mathbf{D}_{16} = \mathbf{D}_{61} &= \frac{1}{3} \sum_{k=1}^n \left[ U_2^q \left( \frac{\sin 2\theta_k}{2} \right) + U_3^q \sin 4\theta_k \right] (z_k^3 - z_{k-1}^3) \\ &= \frac{1}{6} U_2^{\textcircled{1}} \xi_{11}^{\textcircled{1}} + \frac{1}{3} U_3^{\textcircled{1}} \xi_{12}^{\textcircled{1}} + \frac{1}{6} U_2^{\textcircled{2}} \xi_{11}^{\textcircled{2}} + \frac{1}{3} U_3^{\textcircled{2}} \xi_{12}^{\textcircled{2}}, \end{aligned}$$

$$\begin{aligned} \mathbf{D}_{22} &= \frac{1}{3} \sum_{k=1}^n (U_1^q - U_2^q \cos 2\theta_k + U_3^q \cos 4\theta_k) (z_k^3 - z_{k-1}^3) \\ &= \frac{1}{3} U_1^{\textcircled{1}} \xi_{15}^{\textcircled{1}} - \frac{1}{3} U_2^{\textcircled{1}} \xi_9^{\textcircled{1}} + \frac{1}{3} U_3^{\textcircled{1}} \xi_{10}^{\textcircled{1}} + \frac{1}{3} U_1^{\textcircled{2}} \xi_{15}^{\textcircled{2}} - \frac{1}{3} U_2^{\textcircled{2}} \xi_9^{\textcircled{2}} \\ &\quad + \frac{1}{3} U_3^{\textcircled{2}} \xi_{10}^{\textcircled{2}}, \end{aligned}$$

$$\begin{aligned} \mathbf{D}_{26} = \mathbf{D}_{62} &= \frac{1}{3} \sum_{k=1}^n \left[ U_2^q \left( \frac{\sin 2\theta_k}{2} \right) - U_3^q \sin 4\theta_k \right] (z_k^3 - z_{k-1}^3) \\ &= \frac{1}{6} U_2^{\textcircled{1}} \xi_{11}^{\textcircled{1}} - \frac{1}{3} U_3^{\textcircled{1}} \xi_{12}^{\textcircled{1}} + \frac{1}{6} U_2^{\textcircled{2}} \xi_{11}^{\textcircled{2}} - \frac{1}{3} U_3^{\textcircled{2}} \xi_{12}^{\textcircled{2}}, \end{aligned}$$

$$\begin{aligned} \mathbf{D}_{66} &= \frac{1}{3} \sum_{k=1}^n (-U_3^q \cos 4\theta_k + U_5^q) (z_k^3 - z_{k-1}^3) \\ &= -\frac{1}{3} U_3^{\textcircled{1}} \xi_{10}^{\textcircled{1}} + \frac{1}{3} U_5^{\textcircled{1}} \xi_{15}^{\textcircled{1}} - \frac{1}{3} U_3^{\textcircled{2}} \xi_{10}^{\textcircled{2}} + \frac{1}{3} U_5^{\textcircled{2}} \xi_{15}^{\textcircled{2}}. \end{aligned} \quad (9)$$

To sum up, the stiffness coefficients of the hybrid laminates, which are only related to the material constants and geometric factors, can be expressed as

$$\begin{bmatrix} \mathbf{A}_{11} \\ \mathbf{A}_{12} \\ \mathbf{A}_{16} \\ \mathbf{A}_{22} \\ \mathbf{A}_{26} \\ \mathbf{A}_{66} \end{bmatrix} = \sum_{q=\textcircled{1}, \textcircled{2}} \begin{bmatrix} \xi_{13}^q & \xi_1^q & \xi_2^q & 0 & 0 \\ 0 & 0 & -\xi_2^q & \xi_{13}^q & 0 \\ 0 & \frac{\xi_3^q}{2} & \xi_4^q & 0 & 0 \\ \xi_{13}^q & -\xi_1^q & \xi_2^q & 0 & 0 \\ 0 & \frac{\xi_3^q}{2} & -\xi_4^q & 0 & 0 \\ 0 & 0 & -\xi_2^q & 0 & \xi_{13}^{\textcircled{1}} \end{bmatrix} \begin{bmatrix} U_1^q \\ U_2^q \\ U_3^q \\ U_4^q \\ U_5^q \end{bmatrix}, \quad (10)$$

$$\begin{bmatrix} \mathbf{B}_{11} \\ \mathbf{B}_{12} \\ \mathbf{B}_{16} \\ \mathbf{B}_{22} \\ \mathbf{B}_{26} \\ \mathbf{B}_{66} \end{bmatrix} = \frac{1}{2} \sum_{q=\textcircled{1}, \textcircled{2}} \begin{bmatrix} \xi_{14}^q & \xi_5^q & \xi_6^q & 0 & 0 \\ 0 & 0 & -\xi_6^q & \xi_{14}^q & 0 \\ 0 & \frac{\xi_7^q}{2} & \xi_8^q & 0 & 0 \\ \xi_{14}^q & -\xi_5^q & \xi_6^q & 0 & 0 \\ 0 & \frac{\xi_7^q}{2} & -\xi_8^q & 0 & 0 \\ 0 & 0 & -\xi_6^q & 0 & \xi_{14}^q \end{bmatrix} \begin{bmatrix} U_1^q \\ U_2^q \\ U_3^q \\ U_4^q \\ U_5^q \end{bmatrix}, \quad (11)$$

$$\begin{bmatrix} \mathbf{D}_{11} \\ \mathbf{D}_{12} \\ \mathbf{D}_{16} \\ \mathbf{D}_{22} \\ \mathbf{D}_{26} \\ \mathbf{D}_{66} \end{bmatrix} = \frac{1}{3} \sum_{q=\textcircled{1}, \textcircled{2}} \begin{bmatrix} \xi_{15}^q & \xi_9^q & \xi_{10}^q & 0 & 0 \\ 0 & 0 & -\xi_{10}^q & \xi_{15}^q & 0 \\ 0 & \frac{\xi_{11}^q}{2} & \xi_{12}^q & 0 & 0 \\ \xi_{15}^q & -\xi_9^q & \xi_{10}^q & 0 & 0 \\ 0 & \frac{\xi_{11}^q}{2} & -\xi_{12}^q & 0 & 0 \\ 0 & 0 & -\xi_{10}^q & 0 & \xi_{15}^q \end{bmatrix} \begin{bmatrix} U_1^q \\ U_2^q \\ U_3^q \\ U_4^q \\ U_5^q \end{bmatrix}. \quad (12)$$

2.2. *Thermal Stress and Thermal Moment.* The thermal expansion coefficients of the  $k$ -ply in the entire hybrid laminates are

$$\begin{aligned} (\alpha_x)_k &= \alpha_1^q \cos^2 \theta_k + \alpha_2^q \sin^2 \theta_k, \\ (\alpha_y)_k &= \alpha_1^q \sin^2 \theta_k + \alpha_2^q \cos^2 \theta_k, \\ (\alpha_{xy})_k &= (\alpha_1^q - \alpha_2^q) 2 \sin \theta_k \cos \theta_k, \end{aligned} \quad (13)$$

wherein  $\alpha_1^q$  and  $\alpha_2^q$  ( $q = \textcircled{1}, \textcircled{2}$ ) are the thermal expansion coefficients of two different types of lamina. The variation of temperature can be expressed by  $\Delta T$ , and the thermal stress and thermal moment of laminates are expressed as

$$\begin{aligned}
N_x^T &= \sum_{k=1}^n \Delta T \left[ (\bar{Q}_{11})_k (\alpha_x)_k + (\bar{Q}_{12})_k (\alpha_y)_k + (\bar{Q}_{16})_k (\alpha_{xy})_k \right] (z_k - z_{k-1}), \\
N_y^T &= \sum_{k=1}^n \Delta T \left[ (\bar{Q}_{12})_k (\alpha_x)_k + (\bar{Q}_{22})_k (\alpha_y)_k + (\bar{Q}_{26})_k (\alpha_{xy})_k \right] (z_k - z_{k-1}), \\
N_{xy}^T &= \sum_{k=1}^n \Delta T \left[ (\bar{Q}_{16})_k (\alpha_x)_k + (\bar{Q}_{26})_k (\alpha_y)_k + (\bar{Q}_{66})_k (\alpha_{xy})_k \right] (z_k - z_{k-1}),
\end{aligned} \tag{14}$$

$$\begin{aligned}
M_x^T &= \frac{1}{2} \sum_{k=1}^n \Delta T \left[ (\bar{Q}_{11})_k (\alpha_x)_k + (\bar{Q}_{12})_k (\alpha_y)_k + (\bar{Q}_{16})_k (\alpha_{xy})_k \right] \\
&\quad \cdot (z_k^2 - z_{k-1}^2), \\
M_y^T &= \frac{1}{2} \sum_{k=1}^n \Delta T \left[ (\bar{Q}_{12})_k (\alpha_x)_k + (\bar{Q}_{22})_k (\alpha_y)_k + (\bar{Q}_{26})_k (\alpha_{xy})_k \right] \\
&\quad \cdot (z_k^2 - z_{k-1}^2), \\
M_{xy}^T &= \frac{1}{2} \sum_{k=1}^n \Delta T \left[ (\bar{Q}_{16})_k (\alpha_x)_k + (\bar{Q}_{26})_k (\alpha_y)_k + (\bar{Q}_{66})_k (\alpha_{xy})_k \right] \\
&\quad \cdot (z_k^2 - z_{k-1}^2).
\end{aligned} \tag{15}$$

Substituting (1) and (13) into (14) can be used to obtain the expressions of thermal stress, which are only related to the material constants and geometric factors, as shown in

$$\begin{aligned}
N_x^T &= \sum_{k=1}^n \Delta T \left( \frac{1}{2} U_1^{Tq} + \frac{1}{2} U_2^{Tq} \cos 2\theta_k \right) (z_k - z_{k-1}) \\
&= \frac{\Delta T}{2} \left( U_1^{T\ominus} \xi_{13}^{\ominus} + U_2^{T\ominus} \xi_1^{\ominus} + U_1^{T\oplus} \xi_{13}^{\oplus} + U_2^{T\oplus} \xi_1^{\oplus} \right), \\
N_y^T &= \sum_{k=1}^n \Delta T \left( \frac{1}{2} U_1^{Tq} - \frac{1}{2} U_2^{Tq} \cos 2\theta_k \right) (z_k - z_{k-1}) \\
&= \frac{\Delta T}{2} \left( U_1^{T\ominus} \xi_{13}^{\ominus} - U_2^{T\ominus} \xi_1^{\ominus} + U_1^{T\oplus} \xi_{13}^{\oplus} - U_2^{T\oplus} \xi_1^{\oplus} \right), \\
N_{xy}^T &= \frac{\Delta T}{2} \sum_{k=1}^n U_2^{Tq} \sin 2\theta_k (z_k - z_{k-1}) \\
&= \frac{\Delta T}{2} \left( \xi_3^{\ominus} U_2^{T\ominus} + \xi_3^{\oplus} U_2^{T\oplus} \right).
\end{aligned} \tag{16}$$

In which,  $U_1^{Tq}$  and  $U_2^{Tq}$  are defined as the thermal invariants of the hybrid laminates, which can be calculated from the thermal expansion coefficients and the invariants of laminates, as shown in

$$\begin{aligned}
U_1^{Tq} &= (\alpha_1^q + \alpha_2^q) (U_1^q + U_4^q) + (\alpha_1^q - \alpha_2^q) U_2^q, \\
U_2^{Tq} &= (\alpha_1^q + \alpha_2^q) U_2^q + (\alpha_1^q - \alpha_2^q) (U_1^q + 2U_3^q - U_4^q).
\end{aligned} \tag{17}$$

Substituting (1) and (13) into (15) can be used to obtain the expressions of the thermal moment, which are only related to the material constants and geometric factors, as shown in

$$\begin{aligned}
M_x^T &= \frac{1}{2} \sum_{k=1}^n \Delta T \left( \frac{1}{2} U_1^{Tq} + \frac{1}{2} U_2^{Tq} \cos 2\theta_k \right) (z_k^2 - z_{k-1}^2) \\
&= \frac{\Delta T}{4} \left( U_1^{T\ominus} \xi_{14}^{\ominus} + U_2^{T\ominus} \xi_5^{\ominus} + U_1^{T\oplus} \xi_{14}^{\oplus} + U_2^{T\oplus} \xi_5^{\oplus} \right), \\
M_y^T &= \frac{1}{2} \sum_{k=1}^n \Delta T \left( \frac{1}{2} U_1^{Tq} - \frac{1}{2} U_2^{Tq} \cos 2\theta_k \right) (z_k^2 - z_{k-1}^2) \\
&= \frac{\Delta T}{4} \left( U_1^{T\ominus} \xi_{14}^{\ominus} - U_2^{T\ominus} \xi_5^{\ominus} + U_1^{T\oplus} \xi_{14}^{\oplus} - U_2^{T\oplus} \xi_5^{\oplus} \right), \\
M_{xy}^T &= \frac{\Delta T}{4} \sum_{k=1}^n U_2^{Tq} \sin 2\theta_k (z_k - z_{k-1}) \\
&= \frac{\Delta T}{4} \left( \xi_7^{\ominus} U_2^{T\ominus} + \xi_7^{\oplus} U_2^{T\oplus} \right).
\end{aligned} \tag{18}$$

To sum up, the thermal stress and thermal moment of the hybrid laminates, which are only related to the thermal invariants and geometric factors, can be expressed as

$$\begin{bmatrix} N_x^T \\ N_y^T \\ N_{xy}^T \end{bmatrix} = \frac{\Delta T}{2} \sum_{q=\ominus, \oplus} \begin{bmatrix} U_1^{Tq} \xi_{13}^{qq} + U_2^{Tq} \xi_1^{qq} \\ U_1^{Tq} \xi_{13}^{qq} - U_2^{Tq} \xi_1^{qq} \\ U_2^{Tq} \xi_3^{qq} \end{bmatrix}, \tag{19}$$

$$\begin{bmatrix} M_x^T \\ M_y^T \\ M_{xy}^T \end{bmatrix} = \frac{\Delta T}{4} \sum_{q=\ominus, \oplus} \begin{bmatrix} U_1^{Tq} \xi_{14}^{qq} + U_2^{Tq} \xi_5^{qq} \\ U_1^{Tq} \xi_{14}^{qq} - U_2^{Tq} \xi_5^{qq} \\ U_2^{Tq} \xi_7^{qq} \end{bmatrix}. \tag{20}$$

### 3. The Hybrid $A_F B_0 D_S$ Laminates with Immunity to HTSD

**3.1. Necessary and Sufficient Conditions.** From (10), (11), and (12), for matrices  $\mathbf{A}$ ,  $\mathbf{B}$ , and  $\mathbf{D}$ , respectively, can we see that the stiffness coefficients of laminates are only related to geometrical factors and material constants. In order to make the designed laminates suitable for all materials, the necessary and sufficient conditions of geometric factors for the hybrid  $A_F B_0 D_S$  laminates with immunity to HTSD will be derived in this section. The stiffness coefficients of hybrid  $A_F B_0 D_S$  laminates should meet the following relationships [2].

$$\begin{aligned}
\mathbf{B}_{11} = \mathbf{B}_{12} = \mathbf{B}_{16} = \mathbf{B}_{22} = \mathbf{B}_{26} = \mathbf{B}_{66} &= 0, \\
\mathbf{D}_{16} = \mathbf{D}_{26} &= 0.
\end{aligned} \tag{21}$$

Substituting (11) and (12) into Eq. (21) can be used to obtain the necessary and sufficient conditions of geometric factors for the hybrid  $A_F B_0 D_S$  laminates.

$$\begin{aligned}
\xi_5^{\ominus} = \xi_6^{\ominus} = \xi_7^{\ominus} = \xi_8^{\ominus} = \xi_{11}^{\ominus} = \xi_{12}^{\ominus} = \xi_{14}^{\ominus} &= 0, \\
\xi_5^{\oplus} = \xi_6^{\oplus} = \xi_7^{\oplus} = \xi_8^{\oplus} = \xi_{11}^{\oplus} = \xi_{12}^{\oplus} = \xi_{14}^{\oplus} &= 0.
\end{aligned} \tag{22}$$

In order to ensure that the hybrid  $A_F B_0 D_S$  laminates will not cause hygrothermal shear distortion, its thermal shear strain should meet following relationship.

$$\gamma_{xy}^T = 0. \quad (23)$$

Moreover, the connection between thermal stress  $N^T$  and thermal shear strain  $\gamma_{xy}^T$  of  $\mathbf{A}_F\mathbf{B}_0\mathbf{D}_S$  hybrid laminates is

$$\begin{Bmatrix} \varepsilon_x^T \\ \varepsilon_y^T \\ \gamma_{xy}^T \end{Bmatrix} = \begin{bmatrix} \mathbf{A}_{11} & \mathbf{A}_{12} & \mathbf{A}_{16} \\ \mathbf{A}_{12} & \mathbf{A}_{22} & \mathbf{A}_{26} \\ \mathbf{A}_{16} & \mathbf{A}_{26} & \mathbf{A}_{66} \end{bmatrix}^{-1} \begin{Bmatrix} N_x^T \\ N_y^T \\ N_{xy}^T \end{Bmatrix} = \frac{\mathbf{A}^*}{|\mathbf{A}|} \begin{Bmatrix} N_x^T \\ N_y^T \\ N_{xy}^T \end{Bmatrix}, \quad (24)$$

where

$$\mathbf{A}^* = \begin{bmatrix} \mathbf{A}_{22}\mathbf{A}_{66} - \mathbf{A}_{26}^2 & \mathbf{A}_{16}\mathbf{A}_{26} - \mathbf{A}_{12}\mathbf{A}_{66} & \mathbf{A}_{12}\mathbf{A}_{26} - \mathbf{A}_{16}\mathbf{A}_{22} \\ \mathbf{A}_{16}\mathbf{A}_{26} - \mathbf{A}_{12}\mathbf{A}_{66} & \mathbf{A}_{11}\mathbf{A}_{66} - \mathbf{A}_{16}^2 & \mathbf{A}_{16}\mathbf{A}_{16} - \mathbf{A}_{11}\mathbf{A}_{26} \\ \mathbf{A}_{12}\mathbf{A}_{26} - \mathbf{A}_{16}\mathbf{A}_{22} & \mathbf{A}_{16}\mathbf{A}_{16} - \mathbf{A}_{11}\mathbf{A}_{26} & \mathbf{A}_{11}\mathbf{A}_{22} - \mathbf{A}_{12}^2 \end{bmatrix}. \quad (25)$$

Substituting (25) into (24) can be used to obtain the expression of thermal shear strain of the hybrid  $\mathbf{A}_F\mathbf{B}_0\mathbf{D}_S$  laminates.

$$\gamma_{xy}^T = \frac{1}{|\mathbf{A}|} \left[ (\mathbf{A}_{12}\mathbf{A}_{26} - \mathbf{A}_{16}\mathbf{A}_{22})N_x^T + (\mathbf{A}_{12}\mathbf{A}_{16} - \mathbf{A}_{11}\mathbf{A}_{26})N_y^T + (\mathbf{A}_{11}\mathbf{A}_{22} - \mathbf{A}_{12}^2)N_{xy}^T \right]. \quad (26)$$

Inserting (26) into (23) gives

$$\begin{aligned} & (\mathbf{A}_{12}\mathbf{A}_{26} - \mathbf{A}_{16}\mathbf{A}_{22})N_x^T + (\mathbf{A}_{12}\mathbf{A}_{16} - \mathbf{A}_{11}\mathbf{A}_{26})N_y^T \\ & + (\mathbf{A}_{11}\mathbf{A}_{22} - \mathbf{A}_{12}^2)N_{xy}^T = 0. \end{aligned} \quad (27)$$

Inserting (19) into (27) and simplifying gives

$$\begin{aligned} & [(\mathbf{A}_{12}\mathbf{A}_{26} - \mathbf{A}_{16}\mathbf{A}_{22}) + (\mathbf{A}_{12}\mathbf{A}_{16} - \mathbf{A}_{11}\mathbf{A}_{26})] \\ & \cdot \sum_{q=\textcircled{1},\textcircled{2}} U_1^{Tq} \xi_{13}^q + [(\mathbf{A}_{12}\mathbf{A}_{26} - \mathbf{A}_{16}\mathbf{A}_{22}) - (\mathbf{A}_{12}\mathbf{A}_{16} - \mathbf{A}_{11}\mathbf{A}_{26})] \\ & \cdot \sum_{q=\textcircled{1},\textcircled{2}} U_2^{Tq} \xi_1^q + (\mathbf{A}_{11}\mathbf{A}_{22} - \mathbf{A}_{12}^2) \sum_{q=\textcircled{1},\textcircled{2}} U_2^{Tq} \xi_3^q = 0. \end{aligned} \quad (28)$$

If (28) is constantly established, the previous coefficient of thermal material constant  $U_1^{Tq}$  and  $U_2^{Tq}$  ( $q = \textcircled{1}, \textcircled{2}$ ) must be zero.

$$[(\mathbf{A}_{12}\mathbf{A}_{26} - \mathbf{A}_{16}\mathbf{A}_{22}) + (\mathbf{A}_{12}\mathbf{A}_{16} - \mathbf{A}_{11}\mathbf{A}_{26})] \xi_{13}^q = 0 (q = \textcircled{1}, \textcircled{2}), \quad (29)$$

$$\begin{aligned} & [(\mathbf{A}_{12}\mathbf{A}_{26} - \mathbf{A}_{16}\mathbf{A}_{22}) - (\mathbf{A}_{12}\mathbf{A}_{16} - \mathbf{A}_{11}\mathbf{A}_{26})] \xi_1^q \\ & + (\mathbf{A}_{11}\mathbf{A}_{22} - \mathbf{A}_{12}^2) \xi_3^q = 0 (q = \textcircled{1}, \textcircled{2}). \end{aligned} \quad (30)$$

According to (30) can we find out that

$$\xi_1^q = \xi_3^q = 0 (q = \textcircled{1}, \textcircled{2}). \quad (31)$$

Inserting (31) into (10) gives

$$\begin{bmatrix} \mathbf{A}_{11} \\ \mathbf{A}_{12} \\ \mathbf{A}_{16} \\ \mathbf{A}_{22} \\ \mathbf{A}_{26} \\ \mathbf{A}_{66} \end{bmatrix} = \sum_{q=\textcircled{1},\textcircled{2}} \begin{bmatrix} \xi_{13}^q & 0 & \xi_2^q & 0 & 0 \\ 0 & 0 & -\xi_2^q & \xi_{13}^q & 0 \\ 0 & 0 & \xi_4^q & 0 & 0 \\ \xi_{13}^q & 0 & \xi_2^q & 0 & 0 \\ 0 & 0 & -\xi_4^q & 0 & 0 \\ 0 & 0 & -\xi_2^q & 0 & \xi_{13}^q \end{bmatrix} \begin{bmatrix} U_1^q \\ U_2^q \\ U_3^q \\ U_4^q \\ U_5^q \end{bmatrix}. \quad (32)$$

Then inserting (32) into (29) further gives

$$\begin{aligned} & (\mathbf{A}_{12}\mathbf{A}_{26} - \mathbf{A}_{16}\mathbf{A}_{22}) + (\mathbf{A}_{12}\mathbf{A}_{16} - \mathbf{A}_{11}\mathbf{A}_{26}) \\ & = (\mathbf{A}_{26} + \mathbf{A}_{16})(\mathbf{A}_{12} - \mathbf{A}_{11}). \end{aligned} \quad (33)$$

Furthermore, because of  $(\mathbf{A}_{26} + \mathbf{A}_{16}) = 0$  and  $\xi_{13}^q \neq 0$ , (29) is also established. Considering that if  $\xi_4^q = 0$ ,  $\mathbf{A}_{16}$  and  $\mathbf{A}_{26}$  of laminates are both zero and the laminates will not have extension-shear-coupled effect. Therefore, geometric factor  $\xi_4^q$  cannot be zero; thus, the necessary and sufficient conditions for “with immunity to HTSD” can be expressed as

$$\xi_1^{\textcircled{1}} = \xi_3^{\textcircled{1}} = \xi_1^{\textcircled{2}} = \xi_3^{\textcircled{2}} = 0, \xi_4^{\textcircled{1}} \neq 0, \xi_4^{\textcircled{2}} \neq 0. \quad (34)$$

In summary, the necessary and sufficient conditions of the hybrid  $\mathbf{A}_F\mathbf{B}_0\mathbf{D}_S$  laminates with immunity to HTSD can be expressed as

$$\begin{aligned} & \xi_1^{\textcircled{1}} = \xi_3^{\textcircled{1}} = \xi_1^{\textcircled{2}} = \xi_3^{\textcircled{2}} = 0, \xi_4^{\textcircled{1}} \neq 0, \xi_4^{\textcircled{2}} \neq 0, \\ & \xi_5^{\textcircled{1}} = \xi_6^{\textcircled{1}} = \xi_7^{\textcircled{1}} = \xi_8^{\textcircled{1}} = \xi_{11}^{\textcircled{1}} = \xi_{12}^{\textcircled{1}} = \xi_{14}^{\textcircled{1}} = 0, \\ & \xi_5^{\textcircled{2}} = \xi_6^{\textcircled{2}} = \xi_7^{\textcircled{2}} = \xi_8^{\textcircled{2}} = \xi_{11}^{\textcircled{2}} = \xi_{12}^{\textcircled{2}} = \xi_{14}^{\textcircled{2}} = 0. \end{aligned} \quad (35)$$

**3.2. Curing Deformation.** Considering that the curing deformation phenomenon will occur during the process of molding, which may bring about deformation difference between the expected design shape and the free shape after taking off the model at room temperature, now, the thermal strain of the hybrid  $\mathbf{A}_F\mathbf{B}_0\mathbf{D}_S$  laminates with immunity to HTSD will be derived by the necessary and sufficient conditions during the process of curing deformation.

Due to the similarity of influence between humidity changes and temperature changes on composite materials, it only needs to replace the thermal expansion coefficients by humidity expansion coefficients. In order to simplify the analysis and derivation process, the analysis for hygrothermal distortion contains the thermal effect merely.

Substituting (25) into (24) can be used to obtain the expressions of thermal strain of the hybrid  $\mathbf{A}_F\mathbf{B}_0\mathbf{D}_S$  laminates with immunity to HTSD.

$$\begin{aligned}
\varepsilon_x^T &= \frac{1}{|\mathbf{A}|} \left[ (\mathbf{A}_{22}\mathbf{A}_{66} - \mathbf{A}_{26}^2)N_x^T + (\mathbf{A}_{16}\mathbf{A}_{26} - \mathbf{A}_{12}\mathbf{A}_{66})N_y^T \right. \\
&\quad \left. + (\mathbf{A}_{12}\mathbf{A}_{26} - \mathbf{A}_{16}\mathbf{A}_{22})N_{xy}^T \right], \\
\varepsilon_y^T &= \frac{1}{|\mathbf{A}|} \left[ (\mathbf{A}_{16}\mathbf{A}_{26} - \mathbf{A}_{12}\mathbf{A}_{66})N_x^T + (\mathbf{A}_{11}\mathbf{A}_{66} - \mathbf{A}_{16}^2)N_y^T \right. \\
&\quad \left. + (\mathbf{A}_{16}\mathbf{A}_{16} - \mathbf{A}_{11}\mathbf{A}_{26})N_{xy}^T \right].
\end{aligned} \tag{36}$$

Substituting (35) into (19) can give the expressions of thermal stress of the hybrid  $\mathbf{A}_F\mathbf{B}_0\mathbf{D}_S$  laminates with immunity to HTSD.

$$\begin{bmatrix} N_x^T \\ N_y^T \\ N_{xy}^T \end{bmatrix} = \frac{\Delta T}{2} \begin{bmatrix} U_1^{T\ominus}\xi_{13}^\ominus \\ U_1^{T\ominus}\xi_{13}^\ominus \\ 0 \end{bmatrix} + \frac{\Delta T}{2} \begin{bmatrix} U_1^{T\ominus}\xi_{13}^\ominus \\ U_1^{T\ominus}\xi_{13}^\ominus \\ 0 \end{bmatrix}. \tag{37}$$

Inserting (10), (35), and (37) into (36) gives

$$\begin{aligned}
\varepsilon_x^T = \varepsilon_y^T &= \frac{\Delta T}{2} [\mathbf{A}_{16}(\mathbf{A}_{26} - \mathbf{A}_{16}) + \mathbf{A}_{66}(\mathbf{A}_{11} - \mathbf{A}_{12})] \\
&\quad \cdot (U_1^{T\ominus}\xi_{13}^\ominus + U_1^{T\ominus}\xi_{13}^\ominus).
\end{aligned} \tag{38}$$

Therefore, the thermal strains of two main directions of the hybrid  $\mathbf{A}_F\mathbf{B}_0\mathbf{D}_S$  laminates with immunity to HTSD are equal to each other and the value of the thermal strain is not only related to the material constants and temperature variation but also changing with geometric factors  $\xi_2^q$ ,  $\xi_4^q$ , and  $\xi_{13}^q$ .

#### 4. Optimized Design of Laminates

Considering that the extension-shear-coupled effect of hybrid  $\mathbf{A}_F\mathbf{B}_0\mathbf{D}_S$  laminates with immunity to HTSD is the main performance index, the maximum extension-shear-coupled effect is therefore the major objective. Regarding the ply materials and ply angles of each lamina as variables, take the ply materials and ply angles as the optimized design variables. The optimized constraint conditions can be obtained by (35), which ensures that the final optimized laminates are hybrid  $\mathbf{A}_F\mathbf{B}_0\mathbf{D}_S$  laminates with immunity to HTSD. Take the flexibility coefficient  $a_{16}$  as the parameter to test the extension-shear-coupled effect of laminates, which can be obtained by inverting the stiffness matrix of laminates, as shown in (39).

$$\begin{bmatrix} a_{11} & a_{12} & a_{16} & b_{11} & b_{12} & b_{16} \\ a_{12} & a_{22} & a_{26} & b_{12} & b_{22} & b_{26} \\ a_{16} & a_{26} & a_{66} & b_{16} & b_{26} & b_{66} \\ b_{11} & b_{12} & b_{16} & d_{11} & d_{12} & d_{16} \\ b_{12} & b_{22} & b_{26} & d_{12} & d_{22} & d_{26} \\ b_{16} & b_{26} & b_{66} & d_{16} & d_{26} & d_{66} \end{bmatrix} = \begin{bmatrix} \mathbf{A}_{11} & \mathbf{A}_{12} & \mathbf{A}_{16} & \mathbf{B}_{11} & \mathbf{B}_{12} & \mathbf{B}_{16} \\ \mathbf{A}_{12} & \mathbf{A}_{22} & \mathbf{A}_{26} & \mathbf{B}_{12} & \mathbf{B}_{22} & \mathbf{B}_{26} \\ \mathbf{A}_{16} & \mathbf{A}_{26} & \mathbf{A}_{66} & \mathbf{B}_{16} & \mathbf{B}_{26} & \mathbf{B}_{66} \\ \mathbf{B}_{11} & \mathbf{B}_{12} & \mathbf{B}_{16} & \mathbf{D}_{11} & \mathbf{D}_{12} & \mathbf{D}_{16} \\ \mathbf{B}_{12} & \mathbf{B}_{22} & \mathbf{B}_{26} & \mathbf{D}_{12} & \mathbf{D}_{22} & \mathbf{D}_{26} \\ \mathbf{B}_{16} & \mathbf{B}_{26} & \mathbf{B}_{66} & \mathbf{D}_{16} & \mathbf{D}_{26} & s_{66} \end{bmatrix}^{-1}. \tag{39}$$

TABLE 1: Material properties of carbon fiber lamina and glass fiber lamina.

Performance parameters		Carbon fiber lamina	Glass fiber lamina
Elastic modulus (GPa)	$E_1$	181.0	38.6
	$E_2$	10.2	8.3
Shear modulus (GPa)	$G_{12}$	7.2	4.14
Poisson's ratio	$\nu_{12}$	0.28	0.26
Thickness (mm)	$t$	0.1	0.1
Thermal expansion coefficient ( $\mu\text{f}^\circ\text{C}$ )	$\alpha_1$	-0.1	8.6
	$\alpha_2$	25.6	22.1

However, taking into account the actual engineering demands, which should be combined with the good comprehensive properties of carbon fiber composites and the low cost of glass fiber composites, the proportion of two kinds of material must have a minimum requirement. On the one hand, if the proportion of carbon fiber composites is too small, the structural stability of the hybrid laminates cannot be guaranteed. On the other hand, if the proportion of glass fiber composites is too small, the cost reduction effect is not obvious. Therefore, in this paper, the minimum proportions of two types of material are both set as 30% and the mathematical model of optimization problem can be formulated as

$$\begin{aligned}
\min \quad & F(q_1, q_2, \dots, q_n, \theta_1, \theta_2, \dots, \theta_n) = -|a_{16}|, \\
\text{s.t.} \quad & \begin{cases} 1.3n \leq \sum_{i=1}^n q_k \leq 1.7n, \\ -90^\circ < \theta_k \leq 90^\circ, \quad k = 1, 2, \dots, n, \\ \sum_{q_k=1} \cos 2\theta_k (z_k - z_{k-1}) = \sum_{q_k=2} \cos 2\theta_k (z_k - z_{k-1}) = 0, \\ \sum_{q_k=1} \sin 2\theta_k (z_k - z_{k-1}) = \sum_{q_k=2} \sin 2\theta_k (z_k - z_{k-1}) = 0, \\ \sum_{q_k=1} \cos 2\theta_k (z_k^2 - z_{k-1}^2) = \sum_{q_k=2} \cos 2\theta_k (z_k^2 - z_{k-1}^2) = 0, \\ \sum_{q_k=1} \cos 4\theta_k (z_k^2 - z_{k-1}^2) = \sum_{q_k=2} \cos 4\theta_k (z_k^2 - z_{k-1}^2) = 0, \\ \sum_{q_k=1} \sin 2\theta_k (z_k^2 - z_{k-1}^2) = \sum_{q_k=2} \sin 2\theta_k (z_k^2 - z_{k-1}^2) = 0, \\ \sum_{q_k=1} \sin 4\theta_k (z_k^2 - z_{k-1}^2) = \sum_{q_k=2} \sin 4\theta_k (z_k^2 - z_{k-1}^2) = 0, \\ \sum_{q_k=1} \sin 2\theta_k (z_k^3 - z_{k-1}^3) = \sum_{q_k=2} \sin 2\theta_k (z_k^3 - z_{k-1}^3) = 0, \\ \sum_{q_k=1} \sin 4\theta_k (z_k^3 - z_{k-1}^3) = \sum_{q_k=2} \sin 4\theta_k (z_k^3 - z_{k-1}^3) = 0, \\ \sum_{q_k=1} (z_k^2 - z_{k-1}^2) = \sum_{q_k=2} (z_k^2 - z_{k-1}^2) = 0, \\ \sum_{q_k=1} \sin 4\theta_k (z_k - z_{k-1}) \neq 0, \sum_{q_k=2} \sin 4\theta_k (z_k - z_{k-1}) \neq 0. \end{cases}
\end{aligned} \tag{40}$$

TABLE 2: Hybrid  $A_F B_0 D_S$  laminates with immunity to HTSD.

Number of plies	Stacking sequence <sup>o</sup>	$ a_{16} /m \cdot N^{-1}$
1-11	No feasible solution	
12	[1.2623 <sub>c</sub> /-88.1563 <sub>c</sub> /86.2219 <sub>c</sub> /-4.7557 <sub>c</sub> /90 <sub>gl</sub> /0 <sub>gl</sub> /0 <sub>gl</sub> /90 <sub>gl</sub> /85.2442 <sub>c</sub> /-3.7780 <sub>c</sub> /1.8436 <sub>c</sub> /-88.7376 <sub>c</sub> ] <sub>T</sub>	$2.28 \times 10^{-9}$
13	[78.6287 <sub>c</sub> /2.5518 <sub>c</sub> /-62.5528 <sub>c</sub> /-4.4571 <sub>c</sub> /0 <sub>gl</sub> /90 <sub>gl</sub> /57.6811 <sub>c</sub> /90 <sub>gl</sub> /0 <sub>gl</sub> /-22.1785 <sub>c</sub> /74.0623 <sub>c</sub> /-77.5022 <sub>c</sub> /5.4030 <sub>c</sub> ] <sub>T</sub>	$2.15 \times 10^{-9}$
14	[-82.7030 <sub>c</sub> /3.4955 <sub>c</sub> /-9.5277 <sub>c</sub> /68.6342 <sub>c</sub> /-87.1720 <sub>gl</sub> /-4.8666 <sub>gl</sub> /44.7270 <sub>gl</sub> /-44.7270 <sub>gl</sub> /4.8666 <sub>gl</sub> /87.1720 <sub>gl</sub> /-86.6975 <sub>c</sub> /-18.9236 <sub>c</sub> /84.4406 <sub>c</sub> /9.1474 <sub>c</sub> ] <sub>T</sub>	$2.62 \times 10^{-9}$
15	[13.7114 <sub>c</sub> /79.6085 <sub>c</sub> /-25.7171 <sub>c</sub> /-74.2581 <sub>c</sub> /85.3581 <sub>gl</sub> /7.4729 <sub>gl</sub> /-44.4060 <sub>gl</sub> /15.8105 <sub>c</sub> /44.4060 <sub>gl</sub> /-7.4729 <sub>gl</sub> /-85.3581 <sub>gl</sub> /-88.3194 <sub>c</sub> /-87.3471 <sub>c</sub> /24.6320 <sub>c</sub> /-19.9766 <sub>c</sub> ] <sub>T</sub>	$1.68 \times 10^{-9}$
16	[-82.2580 <sub>c</sub> /3.4541 <sub>c</sub> /-7.8035 <sub>c</sub> /71.9029 <sub>c</sub> /0.0178 <sub>gl</sub> /-0.0360 <sub>gl</sub> /-89.9848 <sub>gl</sub> /89.9417 <sub>gl</sub> /-89.9861 <sub>gl</sub> /89.9911 <sub>gl</sub> /-0.0421 <sub>gl</sub> /0.0222 <sub>gl</sub> /-86.5215 <sub>c</sub> /-16.3448 <sub>c</sub> /84.9501 <sub>c</sub> /9.0614 <sub>c</sub> ] <sub>T</sub>	$2.10 \times 10^{-9}$
17	[-86.7602 <sub>c</sub> /86.2949 <sub>c</sub> /-3.1492 <sub>c</sub> /3.7823 <sub>c</sub> /-4.3788 <sub>gl</sub> /35.9403 <sub>gl</sub> /-50.2104 <sub>gl</sub> /89.9014 <sub>gl</sub> /-72.6480 <sub>gl</sub> /41.0040 <sub>gl</sub> /-73.7900 <sub>gl</sub> /27.9322 <sub>gl</sub> /-16.0242 <sub>gl</sub> /-3.7823 <sub>c</sub> /3.1492 <sub>c</sub> /-86.2949 <sub>c</sub> /86.7602 <sub>c</sub> ] <sub>T</sub>	$8.26 \times 10^{-10}$
18	[-0.0130 <sub>gl</sub> /-89.9908 <sub>gl</sub> /0.0171 <sub>gl</sub> /89.9876 <sub>gl</sub> /-80.5781 <sub>c</sub> /79.3162 <sub>c</sub> /7.2684 <sub>c</sub> /-20.7364 <sub>c</sub> /13.9886 <sub>c</sub> /12.0891 <sub>c</sub> /-86.7465 <sub>c</sub> /-66.9711 <sub>c</sub> /0.1373 <sub>c</sub> /80.6754 <sub>c</sub> /-89.9869 <sub>gl</sub> /-0.0163 <sub>gl</sub> /89.9904 <sub>gl</sub> /0.0125 <sub>gl</sub> ] <sub>T</sub>	$1.93 \times 10^{-9}$
19	[-3.8195 <sub>c</sub> /-1.6516 <sub>c</sub> /-87.2690 <sub>c</sub> /-86.3382 <sub>c</sub> /39.6427 <sub>c</sub> /-81.7483 <sub>c</sub> /-0.0004 <sub>gl</sub> /-89.9971 <sub>gl</sub> /89.9928 <sub>gl</sub> /-14.8789 <sub>c</sub> /-0.0071 <sub>gl</sub> /0.0028 <sub>gl</sub> /89.9995 <sub>gl</sub> /25.4403 <sub>c</sub> /-72.0969 <sub>c</sub> /-83.9994 <sub>c</sub> /-0.8820 <sub>c</sub> /79.5202 <sub>c</sub> /-2.8331 <sub>c</sub> ] <sub>T</sub>	$1.93 \times 10^{-9}$
20	[88.5760 <sub>gl</sub> /38.9195 <sub>gl</sub> /-76.4222 <sub>gl</sub> /-17.7876 <sub>gl</sub> /-8.6194 <sub>gl</sub> /12.7407 <sub>c</sub> /-21.3605 <sub>c</sub> /-87.3614 <sub>c</sub> /64.3117 <sub>c</sub> /-30.3418 <sub>c</sub> /-87.4610 <sub>c</sub> /48.9897 <sub>c</sub> /89.9981 <sub>c</sub> /-24.1090 <sub>c</sub> /7.9710 <sub>c</sub> /14.9679 <sub>gl</sub> /69.9391 <sub>gl</sub> /0.3258 <sub>gl</sub> /-50.8020 <sub>gl</sub> /86.2064 <sub>gl</sub> ] <sub>T</sub>	$2.20 \times 10^{-9}$

TABLE 3: Maximum extension-shear-coupled effect of two single-composite laminates.

Number of plies	12	13	14	15	16	17	18	19	20
Carbon fiber laminates ( $10^{-9} m \cdot N^{-1}$ )	2.80	2.71	2.36	2.10	3.01	0.809	1.93	2.19	1.26
Glass fiber laminates ( $10^{-9} m \cdot N^{-1}$ )	12.3	13.0	11.0	8.76	11.0	10.4	9.40	8.53	7.59

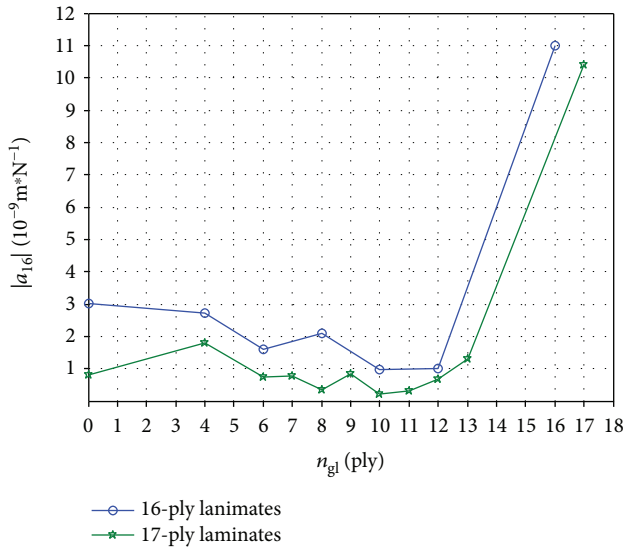


FIGURE 2: Maximal extension-shear-coupled effect of hybrid laminates with different proportions of two materials.

Wherein,  $q_k = 1, 2 (k = 1, 2, \dots, n)$  represents the values of “ $q$ ” for the  $k$ -ply,  $q_k = 1$  shows that the lamina corresponds to the type ① lamina, and  $q_k = 2$  shows that the lamina corresponds to the type ② lamina. If  $\sum_{k=1}^n q_k = n$ , it means that all lamina are made of type ① material, and similarly, if  $\sum_{k=1}^n q_k = 2n$ , it means that all lamina are made of type ② material.

$\theta_k$  represents the paving angle of the  $k$ -ply, whose initial value is selected randomly from the range of  $[-90^\circ, 90^\circ]$ .

The improved differential evolution algorithm DE\_CMSBHS is used to optimize this problem. Because of the strong constraints of optimization problems, which have 18 equality constraints and 2 inequality constraints, the penalty function is applied to deal with the constraints. The type ① lamina and type ② lamina are made up of carbon fiber composites and glass fiber composites, respectively, and the corresponding material parameters are shown in Table 1.

Table 2 shows the 12–20-ply hybrid  $A_F B_0 D_S$  laminates with immunity to HTSD which are optimized by using DE\_CMSBHS algorithm to maximize the extension-shear-coupled effect. The subscripts “c” and “gl” in the table indicate that the lamina is made of carbon fiber composites and glass fiber composites, respectively. As can be seen from the table, (1) there is no hybrid  $A_F B_0 D_S$  laminates with immunity to HTSD for 1–11-ply laminates; (2) for 12–20-ply hybrid  $A_F B_0 D_S$  laminates with immunity to HTSD, the proportions of two kinds of lamina are both not less than 30%; and (3) for optimized laminates with the maximum extension-shear-coupled effect, paving materials are symmetrical about the geometric middle plane and have a relatively uniform distribution, which is the one in the middle and the other on both sides.

In order to reflect the influence of the hybrid form on the extension-shear-coupled effect of laminates more intuitively, this paper further optimizes the extension-shear-coupled

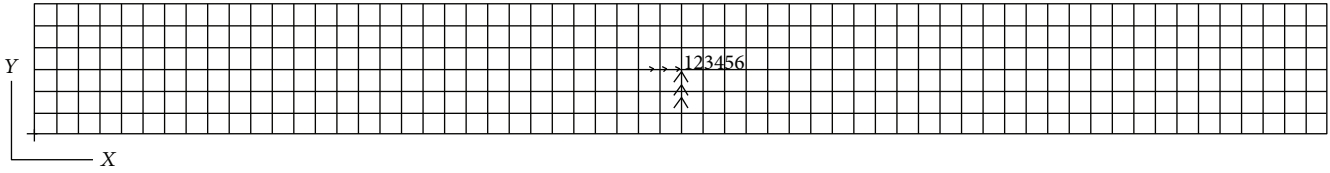


FIGURE 3: Finite element model of the laminates for hygrothermal effect verification.

TABLE 4: Simulation results of hybrid  $A_F B_0 D_S$  laminates on thermal distortion.

Type of laminates	$\varepsilon_x^T$	$\varepsilon_y^T$	$\gamma_{xy}^T$	$\kappa_x^T$	$\kappa_y^T$	$\kappa_{xy}^T$
16-ply laminates	$-6.54 \times 10^{-4}$	$-6.54 \times 10^{-4}$	0	0	0	0
17-ply laminates	$-6.90 \times 10^{-4}$	$-6.90 \times 10^{-4}$	0	0	0	0

effect of single-material laminates and laminates with different proportions of two materials. Table 3 shows the optimization results of two kinds of single-material laminates. Taking 16-ply laminates and 17-ply laminates as an example, the optimized results of laminates with different proportions of two materials are exhibited in Figure 2.

It can be obtained from Table 3 that the maximum extension-shear-coupled effect of glass fiber composite laminates is greater than that of carbon fiber composite laminates in the case of the same number of plies. In the process of optimization by DE\_CMSBHS algorithm, if the minimum proportion limits of the two materials are removed, which means the paving material is free, the final optimal results are totally the same as those of single-glass fiber composite laminates of Table 3. Furthermore, the data in Tables 2 and 3 suggests that the maximum extension-shear-coupled effects of the 14-ply, 17-ply, and 20-ply hybrid laminates are greater than those of single-carbon fiber composite laminates, which indicates that the introduction of glass fiber composite materials into carbon fiber composite laminates can improve the extension-shear-coupled effect of partial numbers of plies laminates.

The abscissa " $n_{gl}$ " in Figure 2 represents the number of glass fiber lamina. As can be seen from Figure 2, (1) for hybrid laminates with different proportions of two materials, there is no feasible solution when  $n_{gl}$  takes some values, for which the geometrical factors of those kinds of laminates cannot satisfy the necessary and sufficient condition of (35) and (2) compared with single-carbon material composite laminates, some hybrid laminates can not only significantly reduce costs but also increase the maximum extension-shear-coupled effect.

## 5. Verification of Mechanical Properties of Laminates

**5.1. Verification of Hygrothermal Effect.** The finite element method is used to verify the distortion caused by the temperature change of the hybrid  $A_F B_0 D_S$  laminates with immunity to HTSD. In this paper, the hygrothermal effect of laminates in Table 2 is verified by the example of 16-ply and 17-ply

laminates and the conclusion of other laminates is the same as that of these laminates.

Based on the finite element software MSC.Patran, the  $10\text{ m} \times 1\text{ m}$  finite element model is established and 360 shell units are divided. In order to simulate the displacement boundary condition of the composite laminates, the geometric center of the finite element model is fixed, as shown in Figure 3. The typical temperature difference of the high-temperature curing process is  $-180^\circ\text{C}$  to this finite element model. Then the finite element software MSC.Nastran is used to compute with the linear statics calculation function.

The calculated results of two kinds of hybrid  $A_F B_0 D_S$  laminates with immunity to HTSD are shown in Table 4. In which,  $\varepsilon_x^T$  and  $\varepsilon_y^T$  are the thermal strain of two main directions,  $\gamma_{xy}^T$  is the thermal shear strain of the laminates, and  $\kappa_x^T$ ,  $\kappa_y^T$ , and  $\kappa_{xy}^T$  are expressed as the surface curvature and distortion of the laminates caused by temperature changes. It can be seen from the table that the shear strain of these laminates are all zero during the high-temperature curing process, which means two kinds of laminates will not cause hygrothermal distortion. The thermal strains of two directions are equal to each other, but this regulation is not suitable for laminates with different numbers of plies. Furthermore, their bending curvature and twist rate are all zero, which indicates that two kinds of laminates will not cause hygrothermal warping distortion.

**5.2. Verification of Extension-Shear-Coupled Effect.** In order to verify the extension-shear-coupled effect of two kinds of hybrid  $A_F B_0 D_S$  laminates in Table 2, the finite element method is also used based on the finite element software MSC.Patran and the finite element model of a rectangular plate with  $12\text{ m} \times 1\text{ m}$  is established. A total of 800 shell units and 891 nodes (six degrees of freedom) are divided, and a multipoint constraint element (RBE2) is used to connect the nodes in the  $1.2\text{ m} \times 1\text{ m}$  region at both ends of the model. The axial tension  $F = 1000\text{ N}$  is applied to the multipoint confinement unit to ensure that the intermediate  $9.6\text{ m} \times 1\text{ m}$  area bears a uniform load. The geometric center of the finite element model is fixed, as shown in Figure 4. The finite element software MSC.Nastran is used to compute with the linear statics calculation function.

The calculated displacement nephogram of two kinds of hybrid  $A_F B_0 D_S$  laminates with immunity to HTSD under axial extension force is shown in Figure 5, and the concrete results of distortion are shown in Table 5. It can be seen from the table that under the axial extension force of 1000 N, the two kinds of hybrid  $A_F B_0 D_S$  laminates not only have axial distortion but also shear distortion and

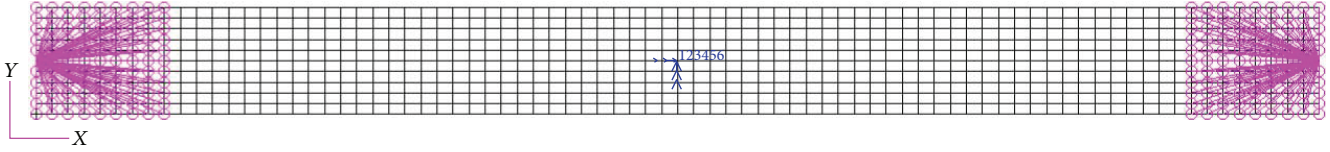


FIGURE 4: Finite element model of the laminates for extension-shear-coupled effect verification.

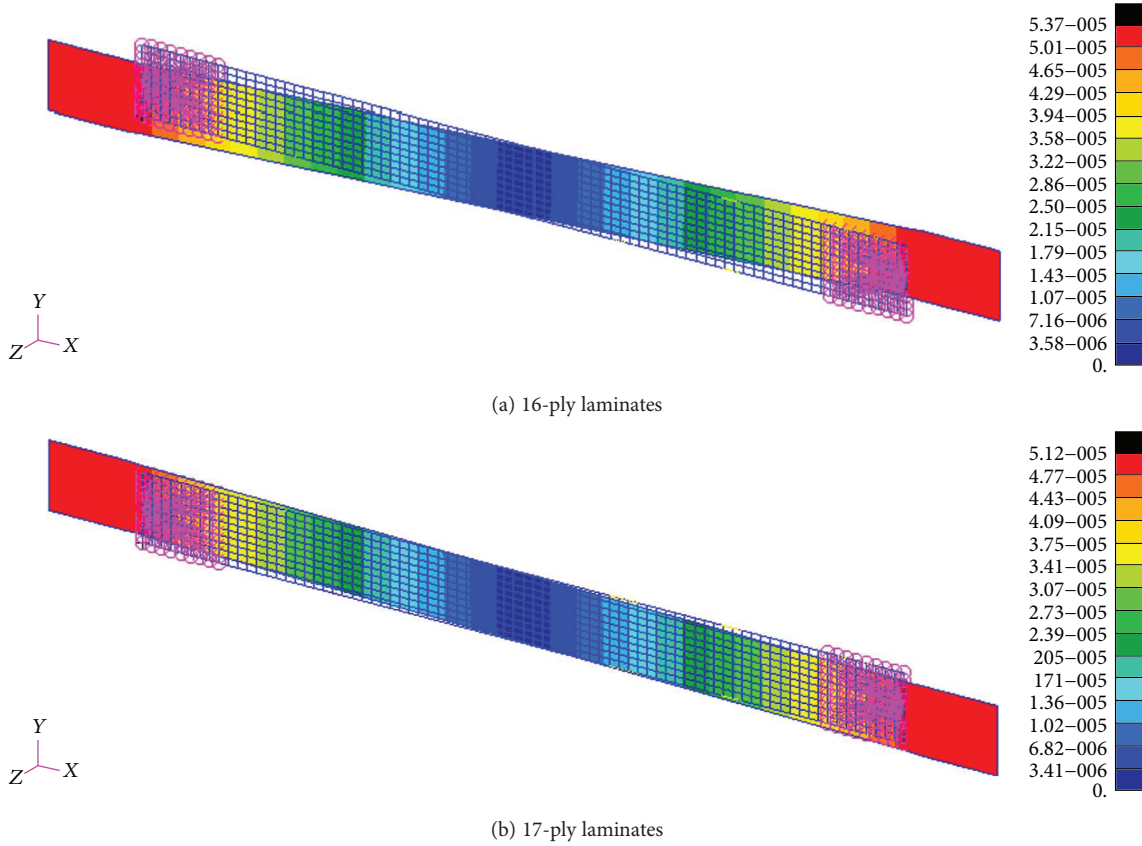


FIGURE 5: Deformation of two kinds of hybrid  $A_F B_0 D_S$  laminates due to extension load.

TABLE 5: Simulation results of hybrid  $A_F B_0 D_S$  laminates on extension-shear distortion.

Type of laminates	Simulation result $\epsilon_x$	Theoretical result $\epsilon_x$	Error of $\epsilon_x$	Simulation result $\gamma_{xy}$	Theoretical result $\gamma_{xy}$	Error of $\gamma_{xy}$
16-ply laminates	$1.08 \times 10^{-5}$	$1.10 \times 10^{-5}$	1.82%	$2.23 \times 10^{-6}$	$2.27 \times 10^{-6}$	1.76%
17-ply laminates	$1.04 \times 10^{-5}$	$1.06 \times 10^{-5}$	1.89%	$8.20 \times 10^{-7}$	$8.26 \times 10^{-7}$	0.73%

the extension-shear-coupled effect of 16-ply laminates is obviously more than that of 17-ply laminates.

Table 5 also shows the theoretical calculation results of two kinds of hybrid  $A_F B_0 D_S$  laminates subjected to axial extension distortion, and through comparison, it is found that the results of finite element analysis agree well with the theoretical results. The error is controlled within 2%, and the extension-shear-coupled effect of laminates is validated. The reason for the error is that the finite element simulation is loaded on the unit node and cannot be completely equivalent to the linear loading method.

5.3. *Robustness Analysis.* Considering that there may be human error and equipment error in the actual process of paving the laminates, which may have a negative effect on the extension-shear-coupled effect, in order to ensure the practicability of the composite laminates, the slight angle deviation should not have an obvious influence on the extension-shear-coupled effect of the hybrid  $A_F B_0 D_S$  laminates with immunity to HTSD. Now, the extension-shear-coupled effect of laminates is analyzed under the ply angle existing deviation, which is based on the Monte Carlo composite laminates robustness analysis method.

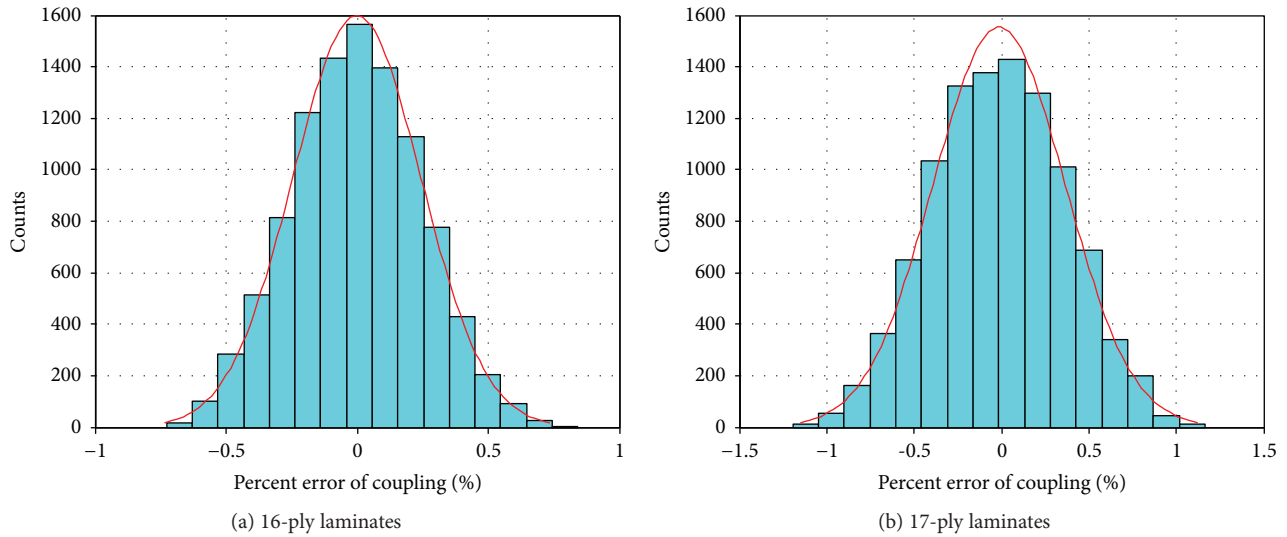


FIGURE 6: Robustness analysis of hybrid  $A_F B_0 D_S$  laminates on extension-shear distortion.

Assume that the paving angle of the  $k$ -ply for the hybrid  $A_F B_0 D_S$  laminates with immunity to HTSD is  $(\theta_k \pm \Delta\theta_k)$ , in which  $\theta_k$  is the theoretical paving angle of the  $k$ -ply and  $\Delta\theta_k$  is the angle deviation and with the value of  $\Delta\theta_k = 2^\circ$  [17]. Figure 6 shows the error distribution of the extension-shear-coupled effect for the 16-ply laminates and the 17-ply laminates in Table 2 under 10,000 random samples. The figure suggests that when there exists a random error in the paving angle of the laminates, the error of extension-shear-coupled effect is in accordance with the normal distribution law and can be controlled within 2%.

## 6. Summary

In this paper, the model of hybrid laminates is established and the expressions of stiffness coefficient, thermal stress, and thermal moment of laminates are derived based on the geometric factor and the necessary and sufficient conditions for hybrid extension-shear-coupled laminates with immunity to HTSD are further derived. The method of combing the improved differential evolution algorithm DE\_CMSBHS with the penalty function is used to optimize the extension-shear-coupled effect of the hybrid  $A_F B_0 D_S$  laminates with immunity to HTSD. The hygrothermal effect, extension-shear-coupled effect, and robustness of laminates are verified. Some conclusions of optimization and simulation can be obtained as follows.

- (1) Although the optimized constraints is enhanced, which is mainly due to the introduction of variable parameter paving materials, the feasible solutions of the hybrid  $A_F B_0 D_S$  laminates with immunity to HTSD can still be obtained by using the DE\_CMSBHS algorithm combined with the penalty function. The optimal solution can be obtained according to the different requirements of different proportions of two materials, which achieved the synchronous optimization of paving angle and paving materials.

- (2) The maximum extension-shear-coupled effect of the single-glass fiber composite laminates is greater than that of single-carbon fiber composite laminates in the case of the same number of plies, and the introduction of glass fiber composite material into single-carbon fiber composite laminates can improve the extension-shear-coupled effect of the partial number of plies laminates.
- (3) The optimized laminates are able to meet the conditions of no hygrothermal shearing distortion and no hygrothermal warping distortion. When there exists a random error in the paving angle of the laminates, the error of extension-shear-coupled effect is in accordance with the normal distribution law and can be controlled within 2%.

The expressions for parameters of the hybrid laminates can also be applied to laminates with other coupling effects. The DE\_CMSBHS algorithm combined with the penalty function can also optimize the different objectives of other types of laminates.

## Data Availability

The data used to support the findings of this study are available from the corresponding author upon request.

## Conflicts of Interest

The authors declare that they have no conflicts of interest.

## Acknowledgments

The authors gratefully acknowledge the support of the National Natural Science Foundation of China (Grant no. 11472003).

## References

- [1] C. B. York, "On extension–shearing coupled laminates," *Composite Structures*, vol. 120, pp. 472–482, 2015.
- [2] J. Li and D. Li, "Extension-shear coupled laminates with immunity to hygro-thermal shearing distortion," *Composite Structures*, vol. 123, pp. 401–407, 2015.
- [3] D. Berry and T. Ashwill, "Design of 9-meter carbon-fiberglass prototype blades: CX-100 and TX-100," SAND2007-0201, Sandia National Laboratories, Warren, RI, USA, 2007.
- [4] C. J. Wang and Y. F. Dai, "Application of carbon fiber composite in aerospace," *Development & Innovation of Machinery & Electrical Products*, vol. 2, 2010.
- [5] R. M. Jones, *Mechanics of Composite Materials*, Scripta Book Company, Washington, DC, USA, 1975.
- [6] M. Moore and D. Frei, "X-29 forward swept wing aerodynamic overview," in *Applied Aerodynamics Conference*, Danvers, MA, USA, 1983.
- [7] N. J. Krone Jr., "Divergence elimination with advanced composites," in *Aircraft Systems and Technology Meeting*, Los Angeles, CA, USA, 1974.
- [8] V. Tischer and V. Venkayya, "Ply-orientation as a variable in multidisciplinary optimization," in *4th Symposium on Multidisciplinary Analysis and Optimization*, Cleveland, OH, USA, 1992.
- [9] M. Patil and M. Patil, "Aeroelastic tailoring of composite box beams," in *35th Aerospace Sciences Meeting and Exhibit*, Reno, NV, USA, 1997.
- [10] S. Guo, "Aeroelastic optimization of an aerobatic aircraft wing structure," *Aerospace Science and Technology*, vol. 11, no. 5, pp. 396–404, 2007.
- [11] S. Adali and V. E. Verijenko, "Optimum stacking sequence design of symmetric hybrid laminates undergoing free vibrations," *Composite Structures*, vol. 54, no. 2-3, pp. 131–138, 2001.
- [12] Y. Zhu, H. Wang, and J. Zhang, "Spacecraft multiple-impulse trajectory optimization using differential evolution algorithm with combined mutation strategies and boundary-handling schemes," *Mathematical Problems in Engineering*, vol. 2015, Article ID 949480, 13 pages, 2015.
- [13] J. A. Snyman, N. Stander, and W. J. Roux, "A dynamic penalty function method for the solution of structural optimization problems," *Applied Mathematical Modelling*, vol. 18, no. 8, pp. 453–460, 1994.
- [14] G. Di Pillo and L. Grippo, "An exact penalty function method with global convergence properties for nonlinear programming problems," *Mathematical Programming*, vol. 36, no. 1, pp. 1–18, 1986.
- [15] C. York, "Unified approach to the characterization of coupled composite laminates: hygro-thermally curvature-stable configurations," *International Journal of Structural Integrity*, vol. 2, no. 4, pp. 406–436, 2011.
- [16] C. B. York, "Tapered hygro-thermally curvature-stable laminates with non-standard ply orientations," *Composites Part A: Applied Science and Manufacturing*, vol. 44, pp. 140–148, 2013.
- [17] R. J. Cross, R. A. Haynes, and E. A. Armanios, "Families of hygrothermally stable asymmetric laminated composites," *Journal of Composite Materials*, vol. 42, no. 7, pp. 697–716, 2008.

## Research Article

# Aeronautical and Aerospace Material and Structural Damages to Failures: Theoretical Concepts

**Andriy Viktorovich Goncharenko** 

*Aircraft Airworthiness Retaining Department, Educational and Research Airspace Institute, National Aviation University, 1 Kosmonavta Komarova Avenue, Kyiv 03058, Ukraine*

Correspondence should be addressed to Andriy Viktorovich Goncharenko; andygoncharenko@yahoo.com

Received 29 December 2017; Revised 5 March 2018; Accepted 1 April 2018; Published 22 April 2018

Academic Editor: Paulo M. S. T. de Castro

Copyright © 2018 Andriy Viktorovich Goncharenko. This is an open access article distributed under the Creative Commons Attribution License, which permits unrestricted use, distribution, and reproduction in any medium, provided the original work is properly cited.

The goal of this paper is to investigate the possible directions of some specified methods for aeronautical and aerospace material and structure effectiveness modeling and optimization. Multioptionality hybrid function uncertainty conditional optimization doctrine application is supposed to be implemented for a degrading failure problem optimal solution determination. The optimal solution is assumed to deliver the maximum value to the probability of damage but not the failure state of the studied material behavior. The principal supposition is that there should be some certain objectively existing value extremized in the conditions of the hybrid optional function uncertainty. There is a scientific proof for the choice of a good maintenance optimal periodicity method that fits the customer's needs, taking into account the effectiveness functions pertaining to the options. The described doctrine allows obtaining the objectively existing optimal values not with the help of a probabilistic but rather with a multioptimal concept. The subjective entropy maximum principle is the other paradigm concept involved in the considered problem solution, which is an equivalent for the uncertainty conditional optimization at the optimal hybrid function distribution determination. By applying simplified, however possible, models and expressions for effectiveness, plausible results are obtained and illustrated in diagrams visualizing the situation and allowing for the selection of a good choice. The ideas of the required material method choice optimization with respect to only two simple parameters, nevertheless, develop numerous particular combinations. Moreover, an increase in the number of parameters and further complication of the problem setting will not change the principle of the problem solution.

## 1. Introduction

The complex process of choosing materials for the airspace industry commonly follows a systematic approach based on multiple requirements and specifications and supported by extensive studies. The executors' individual preferences are an essential factor at this process. It is also important to note that the selection and use of one or another type of material for aerospace use, development of aeronautical engineering and aircraft element structural design, and contemplation of the appropriate fabrication methods are a matter of someone's choice. Therefore, ensuring maximum reliability and efficiency in the field of aeronautics and aerospace, while controlling related costs, faces great pressure for ever

increasing performance. Thus, the problem of optimization plays a central role among many different contributions for achieving those objectives and goes far beyond the framework of basic engineering optimization.

The theory of subjective analysis [1] deals with the scientific explanations of the human's behavior in situations of multialternativeness uncertainty. The theory is developed especially for an evaluation of the individuals' subjective preferences. The preference functions in their turn are found in an explicit view. Moreover, the distribution of the preference functions is obtained with the help of an optimization on the basis of an entropy paradigm. The key point is the so-called subjective entropy maximum principle (SEMP). The core of SEMP is the statement postulating the optimality

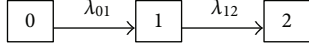


FIGURE 1: Graph of the states of a system with a degrading failure.

of the individual's subjective preference distribution with regard to the achievable alternative uncertainty degree measured by subjective entropy [1, Section 3.5, pp. 141–149].

The doctrine proposed in this paper uses a similar mathematical apparatus; however, an original objective [2–4] versus subjective theoretical concept is described, applied, and discussed in [1, 5] for finding certain extremal values of reliability measures (probabilities). In those cases, studied in the works of [1, 5], the use of SEMP is essential for optimal decision making.

Possible fields of the proposed approach application are morphing aeronautical structures [6, 7], different investigations on the influence of process parameters [8], and effects of heat treatment on fatigue [9] crack growth. Also, the models can be used at modeling the volume-based strain energy density approach [10], as well as fatigue strength subject to cyclic loading [11] and modifications of the activation energy, like for the material purposes discussed in the Sixth World Congress report in [12].

The presented paper's theoretical concept is centered upon material degradation issues.

## 2. Mathematical Modeling and Developed Methods

**2.1. Multioptionality Hybrid Function Uncertainty Conditional Optimization Doctrine Application.** In previous publications [2–4], a multioptional way for determining the optimal solution for a degrading failure problem was shown.

It is proposed to consider modeling and optimizing structural behavior and damage of advanced materials for aerospace use with the help of a graph presented in Figure 1.

In Figure 1, “0” denotes the up state of the system, “1” denotes damage, and “2” denotes failure. The corresponding system state transition intensities are depicted as  $\lambda_{01}$  and  $\lambda_{12}$ .

The situation portrayed with the graph illustrated in Figure 1 is a simplified case for calculating the probabilities of the relating states “0”, “1”, and “2”:  $P_0$ ,  $P_1$ , and  $P_2$ , developing in time  $t$ .

In order to determine the “0”, “1”, and “2” states' probabilities, it is proposed to implement the specially introduced works in [2–4] on hybrid optional-probabilistic approach function distribution entropy conditional optimization doctrine.

The principal supposition is that there should be some certain objectively existing value extremized in conditions of the hybrid optional function uncertainty. This is a radically different ideology from that of subjective analysis [1, 5], where it is postulated that an individual's subjective optimal distribution of her/his preference functions accordingly with the achievable set of alternatives that she/he has taken into consideration, that is, SEMP.

With the use of the supposed multioptional optimality, likewise in subjective analysis [1, 5] conditional optimality

of the individual's subjective preference distribution with extremizing subjective entropy, that is, applying the doctrine analogous to the SEMP concept, we have the right to write down the postulated functional in view of [2–4]:

$$\Phi_h = - \sum_{i=1}^2 h_i(F_i, x) \ln h_i(F_i, x) + t_p^* \sum_{i=1}^2 h_i(F_i, x) F_i(\cdot) + \gamma \left[ \sum_{i=1}^2 h_i(F_i, x) - 1 \right], \quad (1)$$

where  $h_i(F_i)$  are specific hybrid optional effectiveness functions of the option effectiveness functions:  $F_i$  and  $h_i(F_i)$  are similar to the preference functions of [1, 5], however, in this problem setting the assumed specific hybrid optional effectiveness functions  $h_i(F_i)$  are not related with anybody's preferences or choice;  $x$  is unknown, an uncertain multiplier of the Lagrange type;  $t_p^*$  is the system's (see Figure 1) and the system's described process intrinsic parameter, suspected to be an optimal (in such a problem setting,  $t_p^*$ , which is accepted by an assumption optimal value of maintenance periodicity, is going to deliver the maximal value to the probability  $P_1(t)$  of the damaged but still not fractured (failure) state “1” of a material, [2–4]);  $\gamma$  is the normalizing coefficient (function).

The solution  $t_p^*$  of the objective functional in (1) is obtained on the basis of the necessary conditions for the extremum existence of the functional in (1):

$$\frac{\partial \Phi_h}{\partial h_i(F_i, x)} = 0. \quad (2)$$

The condition of (2) yields

$$\frac{\partial \Phi_h}{\partial h_i(\cdot)} = -\ln h_i(\cdot) - 1 + t_p^* F_i(\cdot) + \gamma = 0, \quad \forall i = \overline{1, 2}. \quad (3)$$

This inevitably means in turn

$$\ln h_1(\cdot) - t_p^* F_1(\cdot) = \gamma - 1 = \ln h_2(\cdot) - t_p^* F_2(\cdot). \quad (4)$$

From where

$$\ln h_1(\cdot) - \ln h_2(\cdot) = t_p^* [F_1(\cdot) - F_2(\cdot)]. \quad (5)$$

And in analogous way to (2),

$$t_p^* = \frac{\ln h_1(\cdot) - \ln h_2(\cdot)}{F_1(\cdot) - F_2(\cdot)}. \quad (6)$$

The two considered optional processes (see Figure 1) are as follows:

- (i) Option number 1 is to go out from state “0” or to come into state “1” (in the presented circumstances, both are the same).
- (ii) Option number 2 is to go out from state “1” or to come into state “2” (in the presented circumstances, both are the same).

Hence, it is obvious that the effectiveness functions relating with the options are supposed as follows:

$$F_1 = \lambda_{01}. \quad (7)$$

For the second option,

$$F_2 = \lambda_{12}. \quad (8)$$

The corresponding hybrid optional effectiveness function would be

$$h_1 = xF_1 = x\lambda_{01}, \quad (9)$$

$$h_2 = xF_2 = x\lambda_{12}. \quad (10)$$

Substituting the relevant interrelationships of (7), (8), (9), and (10) for their values into the sought expression in (6) of the optimal periodicity  $t_p^*$ , one obtains

$$t_p^* = \frac{\ln(x\lambda_{01}) - \ln(x\lambda_{12})}{\lambda_{01} - \lambda_{12}} = \frac{\ln(x\lambda_{01}/x\lambda_{12})}{\lambda_{01} - \lambda_{12}}. \quad (11)$$

Finally, (11) yields

$$t_p^* = \frac{\ln(\lambda_{01}) - \ln(\lambda_{12})}{\lambda_{01} - \lambda_{12}}. \quad (12)$$

One has to emphasize here that optimal periodicity  $t_p^*$  in view of (12) and also obtained in [2] has been found not in a probabilistic way but rather in an optimal multioptional way.

The sense of the uncertain multiplier  $x$  becomes obvious with the use of the normalizing condition of the initial functional in (1). That is, with the use of the presupposed relations of (7), (8), (9), and (10)

$$\sum_{i=1}^2 h_i(F_i, x) = 1 = (h_1 = x\lambda_{01}) + (h_2 = x\lambda_{12}), \quad (13)$$

which yields

$$x = \frac{1}{\lambda_{01} + \lambda_{12}}. \quad (14)$$

Therefore, from the expressions for the corresponding hybrid optional effectiveness functions in (9) and (10) it follows that

$$h_1 = \frac{\lambda_{01}}{\lambda_{01} + \lambda_{12}}. \quad (15)$$

Hence,

$$h_2 = \frac{\lambda_{12}}{\lambda_{01} + \lambda_{12}}. \quad (16)$$

**2.2. SEMP Paradigm Concept Equivalent Uncertainty Conditional Optimization Hybrid Function Distribution Determination.** Concerning the objective functional in (1), it is possible to find an optimal distribution of the hybrid optional effectiveness functions starting with the functional (1) extremum existence conditions of (2) and (3).

This gives

$$\ln h_i(\cdot) = \gamma - 1 + tF_i(\cdot). \quad (17)$$

Here in (17), the parameter of time  $t$  is implemented. It is put into the objective functional in (1) instead of  $t_p^*$ . This was done because time now is deemed to be an independent variable. Therefore, this parameter has to be reckoned with as the variable to be optimized.

Then from (17),

$$h_i(\cdot) = \exp[\gamma - 1 + tF_i(\cdot)]. \quad (18)$$

The normalizing condition application, likewise expressed with (13), yields

$$h_1(\cdot) + h_2(\cdot) = 1 = \exp(\gamma - 1)\{\exp[tF_1(\cdot)] + \exp[tF_2(\cdot)]\}. \quad (19)$$

From where

$$\exp(\gamma - 1) = \frac{1}{\exp[tF_1(\cdot)] + \exp[tF_2(\cdot)]}. \quad (20)$$

At last,

$$h_i^{opt}(\cdot) = \frac{\exp[tF_i(\cdot)]}{\sum_{j=1}^2 \exp[tF_j(\cdot)]}. \quad (21)$$

The obtained optimal distribution, described with (21) of the hybrid optional functions, ensures the conditional extremum (maximum) for the hybrid optional function entropy or the maximum to the objective functional in (1).

Indeed, one can easily make sure that the extremum existence conditions of the second order, from (3), are as follows:

$$\frac{\partial^2 \Phi_h}{\partial h_i(F_i, x)^2} = -\frac{1}{h_i(F_i, x)} < 0. \quad (22)$$

This inequality of (22) is satisfied at any "point", since the hybrid optional functions always have positive values ]0 ... 1[ in the postulated view functional for multioptional consideration, like (1), including the "point" suspected for the extremum on the condition of (2).

Moreover, although the optimally distributed hybrid optional functions expressed with (21) are different from the hybrid optional functions described with (9) and (10), as well as their developed transformed versions in the view of (15) and (16), in the case of (6), (7), (8), (9), (10), (11), (12), (13), (14), (15), and (16), the functions of (21) and (15) and (16) have the same value.

**2.3. An Idea of Combining the Concepts.** It can be easily seen that if the optimal periodicity  $t_p^*$ , in view of (12), is substituted for the value of time into the optimal distribution of hybrid optional functions represented by (21), then (15) and (16) will be derived.

Indeed,

$$h_1^{\text{opt}}(\cdot) \Big|_{t=t_p^*} = \frac{\exp \left[ t_p^* F_1(\cdot) \right]}{\exp \left[ t_p^* F_1(\cdot) \right] + \exp \left[ t_p^* F_2(\cdot) \right]}. \quad (23)$$

Then,

$$\exp \left[ t_p^* F_1(\cdot) \right] = \exp \left[ \frac{\ln(\lambda_{01}) - \ln(\lambda_{12})}{\lambda_{01} - \lambda_{12}} \lambda_{01} \right]. \quad (24)$$

And equally,

$$\exp \left[ t_p^* F_2(\cdot) \right] = \exp \left[ \frac{\ln(\lambda_{01}) - \ln(\lambda_{12})}{\lambda_{01} - \lambda_{12}} \lambda_{12} \right], \quad (25)$$

$$\exp \left[ t_p^* F_1(\cdot) \right] = \exp \left[ \ln \left( \frac{\lambda_{01}}{\lambda_{12}} \right) \right]^{\lambda_{01}/(\lambda_{01}-\lambda_{12})}, \quad (26)$$

$$\exp \left[ t_p^* F_2(\cdot) \right] = \exp \left[ \ln \left( \frac{\lambda_{01}}{\lambda_{12}} \right) \right]^{\lambda_{12}/(\lambda_{01}-\lambda_{12})}, \quad (27)$$

$$\exp \left[ t_p^* F_1(\cdot) \right] = \left( \frac{\lambda_{01}}{\lambda_{12}} \right)^{\lambda_{01}/(\lambda_{01}-\lambda_{12})}, \quad (28)$$

$$\exp \left[ t_p^* F_2(\cdot) \right] = \left( \frac{\lambda_{01}}{\lambda_{12}} \right)^{\lambda_{12}/(\lambda_{01}-\lambda_{12})}. \quad (29)$$

From (23),

$$h_1^{\text{opt}}(\cdot) \Big|_{t=t_p^*} = \frac{1}{1 + \left( \exp \left[ t_p^* F_2(\cdot) \right] / \exp \left[ t_p^* F_1(\cdot) \right] \right)}. \quad (30)$$

Therefore,

$$h_1^{\text{opt}}(\cdot) \Big|_{t=t_p^*} = \frac{1}{1 + \left( (\lambda_{01}/\lambda_{12})^{\lambda_{12}/(\lambda_{01}-\lambda_{12})} / (\lambda_{01}/\lambda_{12})^{\lambda_{01}/(\lambda_{01}-\lambda_{12})} \right)}, \quad (31)$$

$$h_1^{\text{opt}}(\cdot) \Big|_{t=t_p^*} = \frac{1}{1 + \left( (\lambda_{01}/\lambda_{12})^{\lambda_{12}/(\lambda_{01}-\lambda_{12}) - \lambda_{01}/(\lambda_{01}-\lambda_{12})} \right)}, \quad (32)$$

$$h_1^{\text{opt}}(\cdot) \Big|_{t=t_p^*} = \frac{1}{1 + (\lambda_{01}/\lambda_{12})^{-1}}, \quad (33)$$

$$h_1^{\text{opt}}(\cdot) \Big|_{t=t_p^*} = \frac{1}{1 + (\lambda_{12}/\lambda_{01})}. \quad (34)$$

This inevitably gives

$$h_1^{\text{opt}}(\cdot) \Big|_{t=t_p^*} = \frac{\lambda_{01}}{\lambda_{01} + \lambda_{12}}. \quad (35)$$

The parallel to the derivation of (23), (24), (25), (26), (27), (28), (29), (30), (31), (32), (33), (34), and (35) leads to

$$h_2^{\text{opt}}(\cdot) \Big|_{t=t_p^*} = \frac{\lambda_{12}}{\lambda_{01} + \lambda_{12}}. \quad (36)$$

Now, it raises the problem of the combinational concept of both the multioptional doctrine [2–4] (for the objectively existing phenomena) and the multialternative entropy paradigm [1, 5] (for the subjectively preferred choices and decision making).

The part of the general problem dealing with the objectively existing maximum of probability  $P_1(t)$  is solved with the help of the multioptional doctrine, whereas the options for the part of the material improvement for the diversity of the objective parameters  $\lambda_{01}$  and  $\lambda_{12}$  is finally going to be made with the use of SEMP.

**2.4. Simulation.** A numerical case study is proposed in order to illustrate the theoretical concepts and clarify mathematical derivations of (1), (2), (3), (4), (5), (6), (7), (8), (9), (10), (11), (12), (13), (14), (15), (16), (17), (18), (20), (21), (22), (23), (24), (25), (26), (27), (28), (29), (30), (31), (32), (33), (34), (35), and (36). The conducted simulation detailing the case study performs the role of an aid for the possible applications of the multioptional doctrine.

The usefulness of this methodology depends upon the individual subjective preferences of the persons conducting the experimentation procedure, and details may vary in instruments, materials, sets or sequences, and so on.

Also, for example, for data collection, the simplest forms may be used, like basic spreadsheets or something similar. It is not so important for the given stage of the developed theoretical approach.

The purpose of the modeling carried out here is to manifest the damages presented herein which were due to the failures of the ability of theoretical concepts to be applied to a wide range of material-degrading phenomena.

For the computer simulation in the framework of the approaches of (1), (2), (3), (4), (5), (6), (7), (8), (9), (10), (11), (12), (13), (14), (15), (16), (17), (18), (20), (21), (22), (23), (24), (25), (26), (27), (28), (29), (30), (31), (32), (33), (34), (35), and (36), there have been calculation data used which are visible in the diagrams plotted in Figures 2–4.

Figure 2 shows the curves of state “1” (see Figure 1) probability  $P_1(t)$ .  $P_{101}(\lambda_{01}, 1 \cdot 10^{-3})$  stands for  $P_1(t)$  maximums in the case of the transition intensity  $\lambda_{01}$  variation and  $\lambda_{12} = 1 \cdot 10^{-3}$  plotted as the function of  $T_{01}(\lambda_{01}, 1 \cdot 10^{-3})$  when the objective parameters  $\lambda_{01}$  and  $\lambda_{12}$  have corresponding values.  $T_{01}(\lambda_{01}, 1 \cdot 10^{-3})$  was computed with help of (12).  $P_{112}(5 \cdot 10^{-3}, \lambda_{12})$  stands for  $P_1(t)$  maximums in the case of the transition intensity  $\lambda_{12}$  variation and  $\lambda_{01} = 5 \cdot 10^{-3}$ .  $P_{112}(5 \cdot 10^{-3}, \lambda_{12})$  was plotted as the function of  $T_{12}(5 \cdot 10^{-3}, \lambda_{12})$  similar to the method of a phase portrait ( $P_{101}(\lambda_{01}, 1 \cdot 10^{-3}) - T_{01}(\lambda_{01}, 1 \cdot 10^{-3})$ ). The next seven curves of  $P_1(t)$ ,  $P_1(0.6 \cdot 10^{-3} \dots 4 \cdot 10^{-3}, 1 \cdot 10^{-3}, t)$ , indicate the situation of the transition intensity  $\lambda_{01}$  variation and  $\lambda_{12} = 1 \cdot 10^{-3}$  with the corresponding maximum values crossed with the  $P_{101}(\lambda_{01}, 1 \cdot 10^{-3})$  line. The last seven curves

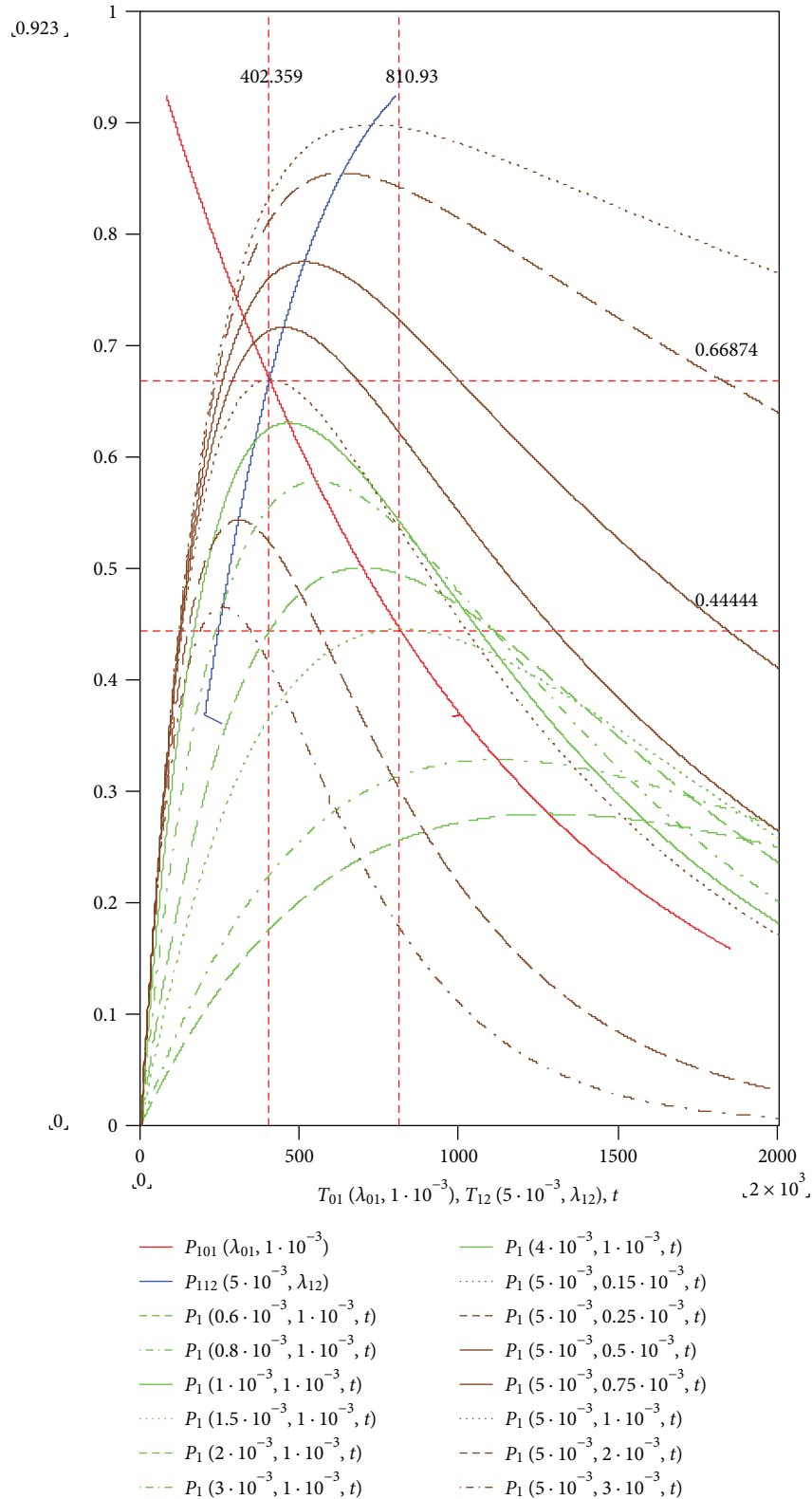


FIGURE 2: Divergence of the objectively existing maximum for the probability of the materials damaged; however, there is no fractured state in the case of the transition intensity variations.

of the probability  $P_1(t)$ ,  $P_1(5 \cdot 10^{-3}, 0.15 \cdot 10^{-3} \dots 3 \cdot 10^{-3}, t)$ , are plotted for the other alternative case of the transition intensity  $\lambda_{12}$  variation and  $\lambda_{01} = 5 \cdot 10^{-3}$ .

Also, there are two points with the coordinates of (402.359, 0.66874) and (810.93, 0.44444) denoted for the specified examples in Figure 2.

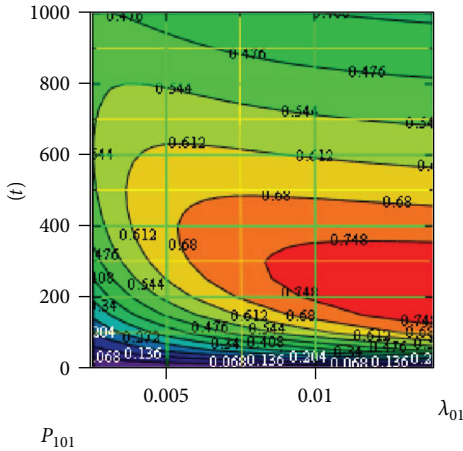


FIGURE 3: Change of the probability of the materials possible and assumed by the damaged state of the experimental data. However, in the illustrated diagram the materials are not fractured. By supposition, the represented change occurs with the variation of the transition intensity from the normal state, with the transition intensity to the fractured state being steady.

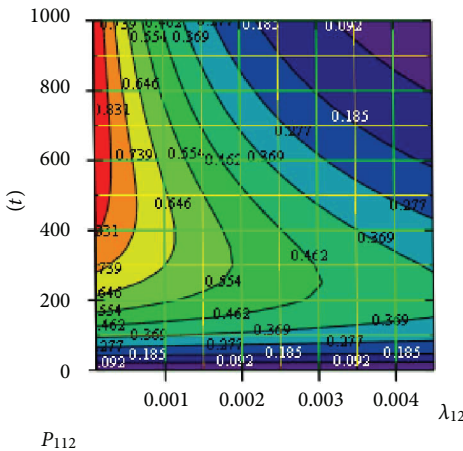


FIGURE 4: Change of the probability of the materials possible and assumed by the damaged state of experimental data in time. However, in the illustrated diagram the materials are not fractured. By supposition, the represented change occurs with the variation of the transition intensity from the damaged state, with the transition intensity from the normal state being steady.

The results of numerical modeling shown in Figure 3 represent a contour plot for the probability  $P_1(t)$  of the damaged but not ruined state “1” denoted as  $P_{101}$  and correspond to the situation described above.

Figure 4 illustrates the situation when  $P_1(t)$  changes in time as a result of the transition intensity  $\lambda_{12}$  variation and  $\lambda_{01} = 5 \cdot 10^{-3}$ .

### 3. Results and Discussion

3.1. *Analysis of the Obtained Results.* The obtained results represented by the diagrams shown in Figures 2–4 brightly distinguish the two major options for the improvement of

the material described above, increasing its reliability measures: the required change of the transition intensities  $\lambda_{12}$  and  $\lambda_{01}$ . If the case is not so simple, certain additional assumptions can be made.

3.2. *Discussion.* The demonstrated hereinafter possibility of the multioptional optimality doctrine application in the areas of exclusively objective options in contrast to that which is subjectively preferred by somebody’s alternatives gives the same result as that one found on the basis of the probabilistic approach [2–4]. This is an undoubtedly fragmented piece of evidence proving the substantiation of the proposed doctrine.

The optimal maintenance periodicity can be predetermined not necessarily with the probability  $P_1(t)$  maximum value. In such a case, a more complicated approach perhaps should be used; however, the application of SEMP still looks even more attractive since it implies taking into account someone’s individual subjective preference distribution. Therefore, the role of the theoretical evolutions as well as subjective analysis [1, 5] is apparently going to be increased.

With regard to material science and its theory and applications traced with the references of [6–12], the presented herewith entropy approach also gives some plausible results.

### 4. Conclusions

The case study, analyzed in this paper on aeronautical and aerospace materials and structural damages due to the failures of theoretical concepts, proves that the described doctrine allows obtaining the objectively existing optimal values not with the help of probabilistic but rather with multioptimal hybrid effectiveness functions.

Conditions of uncertainty embodied in the corresponding entropies are crucial to the two following aspects: objective hybrid optional and subjective preference function optimal distributions.

The preference functions give the possibility of the considered alternative material assessment with respect to the preference entropy uncertainty measure.

In further research, some other effectiveness functions and their variables should be considered. Also, it would be useful to find more theoretical results and applicable areas of the hybrid optional optimality doctrine as well as the theory of subjective analysis.

### Conflicts of Interest

The author declares that there is no conflict of interests regarding the publication of this paper.

### References

- [1] V. Kasianov, *Subjective Entropy of Preferences. Subjective Analysis: Monograph*, Institute of Aviation, Warsaw, Poland, 2013, <http://kasianovv.wixsite.com/entropyofpreferences>.
- [2] A. V. Goncharenko, “Optimal managerial and control values for active operation,” *Electronics and control systems*, vol. 3, no. 49, pp. 112–115, 2016.
- [3] A. V. Goncharenko, “Optimal UAV maintenance periodicity obtained on the multi-optional basis,” in *2017 IEEE 4th*

- International Conference Actual Problems of Unmanned Aerial Vehicles Developments (APUAVD)*, pp. 65–68, IEEE, Kyiv, Ukraine, October 2017.
- [4] A. V. Goncharenko, “A hybrid approach to the optimal aeronautical engineering maintenance periodicity determination,” *Proceedings of the National Aviation University*, vol. 72, no. 3, pp. 42–47, 2017.
- [5] A. V. Goncharenko, “Aircraft operation depending upon the uncertainty of maintenance alternatives,” *Aviation*, vol. 21, no. 4, pp. 126–131, 2017.
- [6] S. M. O. Tavares, S. J. Moreira, P. M. S. T. de Castro, and P. V. Gamboa, “Morphing aeronautical structures: a review focused on UAVs and durability assessment,” in *2017 IEEE 4th International Conference Actual Problems of Unmanned Aerial Vehicles Developments (APUAVD)*, pp. 49–52, IEEE, Kyiv, Ukraine, October 2017.
- [7] S. J. Moreira, S. M. O. Tavares, and P. M. S. T. de Castro, “Morphing structures and fatigue: the case of an unmanned aerial vehicle wing leading edge,” *Fatigue & Fracture of Engineering Materials & Structures*, vol. 40, no. 10, pp. 1601–1611, 2017.
- [8] R. G. Citarella, P. Carlone, M. Lepore, and G. S. Palazzo, “A FEM-DBEM investigation of the influence of process parameters on crack growth in aluminum friction stir welded butt joints,” *Key Engineering Materials*, vol. 554-557, pp. 2118–2126, 2013.
- [9] O. Fergani, A. Bratli Wold, F. Berto, V. Brotan, and M. Bambach, “Study of the effect of heat treatment on fatigue crack growth behaviour of 316L stainless steel produced by selective laser melting,” *Fatigue & Fracture of Engineering Materials & Structures*, vol. 41, no. 5, pp. 1102–1119, 2018.
- [10] F. Berto and P. Lazzarin, “A review of the volume-based strain energy density approach applied to V-notches and welded structures,” *Theoretical and Applied Fracture Mechanics*, vol. 52, no. 3, pp. 183–194, 2009.
- [11] A. Tugarinov, E. Yurchenko, A. Pogrebniak, and M. Regulski, “Calculation method of aerotechnics products fatigue strength subject to cyclic loading,” *Proceedings of the National Aviation University*, vol. 61, no. 4, pp. 111–116, 2014.
- [12] A. I. Bogdanovych, “Estimation of kinetic characteristics and modification activation energy of “ИИХ15” in aviation fuel “TC-1”,” in *Materials of the Sixth World Congress “Aviation in the XXI-st Century”*, vol. 3, pp. 1.6.9–1.6.13, Kyiv, Ukraine, September 2014.

## Research Article

# Effective Mechanical Property Estimation of Composite Solid Propellants Based on VCFEM

Liu-Lei Shen, Zhi-Bin Shen , Yan Xie, and Hai-Yang Li 

*College of Aeronautics and Astronautics, National University of Defense Technology, Changsha, Hunan, China*

Correspondence should be addressed to Zhi-Bin Shen; zb\_shen@yeah.net

Received 20 November 2017; Revised 22 January 2018; Accepted 11 February 2018; Published 12 April 2018

Academic Editor: Filippo Berto

Copyright © 2018 Liu-Lei Shen et al. This is an open access article distributed under the Creative Commons Attribution License, which permits unrestricted use, distribution, and reproduction in any medium, provided the original work is properly cited.

A solid rocket motor is one of the critical components of solid missiles, and its life and reliability mostly depend on the mechanical behavior of a composite solid propellant (CSP). Effective mechanical properties are critical material constants to analyze the structural integrity of propellant grain. They are estimated by a numerical method that combines the Voronoi cell finite element method (VCFEM) and the homogenization method in the present paper. The correctness of this combined method has been validated by comparing with a standard finite element method and conventional theoretical models. The effective modulus and the effective Poisson's ratio of a CSP varying with volume fraction and component material properties are estimated. The result indicates that the variations of the volume fraction of inclusions and the properties of the matrix have obvious influences on the effective mechanical properties of a CSP. The microscopic numerical analysis method proposed in this paper can also be used to provide references for the design and the analysis of other large volume fraction composite materials.

## 1. Introduction

A composite solid propellant (CSP), a highly packed particulate composite, is a prime structural material of a solid rocket motor in addition to an energetic material. A CSP consists of polymeric binder matrix (e.g., HTPB) and particle inclusions. The particle materials are usually ammonium perchlorate (AP) and aluminum (Al) [1].

Parametric variations of effective material constants have been studied by numerical and analytical methods in the past [2, 3] and present [4–6]. There are a few studies on the microstructural morphology of the CSP. The effective mechanical properties of CSP are critical to study the deformation and fracture characteristics of propellant grain. Various experimental and numerical studies demonstrate that the mechanical properties of the CSP can be highly sensitive to the microstructural morphology such as the dimension, shape, distribution, and properties of the inclusion. It is a kind of natural choice to study the mechanical properties of the CSP from the aspects of microscopic mechanical. In the early stage, some classical theoretical models of conventional composites have been tailored to

estimate the effective properties of the CSP. These theoretical investigations are always limited to simple geometries but are often incapable of reflecting the realistic microstructure of the CSP. Instead, the numerical method becomes increasingly popular because its analysis is based on the realistic geometric simulation model. Zhang et al. [7] employed a homogenization theory and the displacement finite element method (FEM) to compute the mean temperature and heat flux of the CSP's representative volume element (RVE). The effect of orientation and shape of oxidizer particles on the burning rate was examined by a direct numerical simulation approach developed by Plaud et al. [8]. Another group of models published devoted to estimate mechanical properties of propellants in recent years. Yang and Liu [9] use coarse triangle meshes and ANSYS to predict the elastic modulus of the composite solid propellant. Zhi et al. [10] use ABAQUS to study the effects of the critical contact stress, initial contact stiffness, and contact failure distance on the damaged interface model. Matous and Geubelle [11] and Matous et al. [12] develop a damage analysis tool at multiple scales from particle packing to failure use of a numerical framework.

However, the conventional finite element method requires complex grid element and huge computational costs, which limits replication and application in microstructure analysis; furthermore, very small elements may occur owing to the fact that the space among the inclusion is too narrow to create a perfect mesh. For example, they have to shrink particles in contact with other particles or reduce the volume fraction to create high-quality meshes [7, 12]. To overcome some of the limitations discussed above, Ghosh and his coworkers proposed a new numerical method known as the Voronoi cell finite element model (VCFEM) to analyze heterogeneous materials. In 1990, they [13] proposed a two-dimensional automatic mesh generation technique to discretize the composite domain to yield an aggregate of convex Voronoi polygons. An assumed stress hybrid formulation has been implemented to utilize the resulting Voronoi polygons as elements in a finite element model in 1993 [14]. In the following years, the developments of VCFEM were presented for linear elastic problems [15] and elastic-plasticity problems [16], as well as failure analysis [17]. Over the last few years, the VCFEM was further developed to address some engineering problems [18, 19]. In addition, some contributions had been devoted by other researchers to develop this method to analyze the thermomechanical [20] and the effective properties [21] of heterogeneous materials. However, very few works have been attempted to tailor the VCFEM to estimate effective mechanical properties of the CSP. Shen et al. [1] introduced a noninclusion VCFEM to analyze material viscoelastic constants.

The feasibility study on the application of VCFEM in the estimation of effective mechanical properties of the CSP is carried out in this paper. We focus on establishing a numerical model for the analysis of composites with high particle volume fraction. A displacement comparison between the results of VCFEM and those of commercial FEM software is carried out to indicate the correctness of the program code. And the validity of the proposed combined method is obtained by employing two classical theory methods from the literature. In addition, a simple case is analyzed to understand the influence of microstructural morphology on the effective modulus and effective Poisson ratio of the CSP.

## 2. Computational Procedure

**2.1. Microstructure Model of CSP.** The CSP is one of the highly particulate composite materials, always with particle volume fraction between 70% and 80%, or even higher [7]. Figure 1 is a SEM image of the HTPB propellant. Spherical particles are bonded together tightly by the polymer matrix. It is necessary to model a RVE to reflect their microstructure features before obtaining effective material constants of the CSP numerically. Voronoi tessellation is a simple but effective geometric representation for charactering the microstructures of the composite. The tessellation can subdivide a plane into many Voronoi cells determined by a set of centers. Each cell may be perceived as the intersection of open half-planes bounded by the perpendicular bisectors of lines joining one inclusion center with each of its neighbors. However, the inclusion will be dissected into multiple segments by

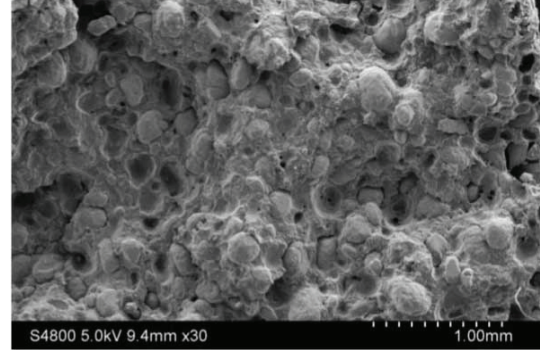


FIGURE 1: SEM image of the HTPB propellant.

element boundaries of the mesh, when the radius of a circular inclusion in a Voronoi cell is greater than the minimum distance from its center to the center of other cells. The centers generated randomly may lead the model to be inhomogeneous usually. If an element center is closed to one adjacent center than any other adjacent centers, the room between the two centers cannot be filled with inclusion. It will result in the failure to get a large volume fraction of circular inclusion.

In fact, the coordinates of circular inclusions are almost determined when the volume fraction of circular inclusions is large and their sizes are almost equal. A new center-generated project is proposed here. In this project, the locations of centers are generated on the basis of the corresponding existing optimal equal circle packing schemes when the center's number is determined. Those circles will be homogeneous in a RVE model. And the distances between any center and other adjacent centers are almost equal.

The procedure to build the microstructure model with a large volume fraction of inclusions is described below.

- (1) The size of RVE ( $L_{RVE}$ ) is determined based on the inclusion size and material property. RVE sizes are defined as the minimum size of a microstructural model that meets the requirement of statistical homogeneity [22].
- (2) The number of inclusion is generated randomly from the range of  $n_{min}$  to  $n_{max}$ .  $n_{min}$  and  $n_{max}$  can be obtained using the equation:

$$\begin{aligned} n_{min} &= \frac{V_f L_{RVE}^2}{\pi r_{max}^2}, \\ n_{max} &= \frac{V_f L_{RVE}^2}{\pi r_{min}^2}, \end{aligned} \quad (1)$$

where  $r_{max}$  and  $r_{min}$  are the maximum value and the minimum value of mean values of inclusion radius, respectively, and  $V_f$  is the volume fraction of inclusion.

- (3) The radius and center positions of the circle inclusion are read from the corresponding existing optimal equal circle packing schemes. The RVE is meshed

with the convex Voronoi polygons according to the centers of the system.

- (4) Transform the circles into ellipses. The random number generator is used to generate the lengths of major axes, ratio of major to minor axis length, and orientation (angle) of the major axis of each inclusion. The nonoverlapping constraint has to be imposed. To establish this, each inclusion is contained inside a circle having a diameter equal to the length of the major axis.

Figure 2 describes an example. The length and width are 6 mm. The mean values of the radius of inclusions are ranging from  $300 \mu\text{m}$  to  $310 \mu\text{m}$ . Since the volume fraction is about 83%, the  $n_{\min}$  and  $n_{\max}$  are 95 and 101, respectively. We set the number of inclusion to 100. And the RVE model is meshed following the second step and third step. The radius of inclusions is  $308 \mu\text{m}$ , and the volume fraction is 80%. Further, the inclusions are transformed into ellipses randomly following the fourth step. We can get a model with a volume fraction of 61%.

**2.2. Hybrid Element Formulation.** In this section, the finite element formulation with Voronoi polygons will be reviewed briefly. Figure 3 shows an example of a hybrid element, used in the VCFEM method, with an embedded inclusion. Each node of inclusion may be perceived as the intersection of the circular inclusion and the line joining the inclusion center with each matrix node. The element formulation, as reported in [14], is based upon the stationary of total complementary energy principle. The total complementary energy of the element with an embedded heterogeneity is the addition of the energy of the matrix and inclusion:

$$\begin{aligned} \Pi_{mc} = & \int_{A_e^M} \frac{1}{2} (\boldsymbol{\sigma}_e^M)^T \mathbf{S}^M \boldsymbol{\sigma}_e^M dA_e^M \\ & + \int_{A_e^I} \frac{1}{2} (\boldsymbol{\sigma}_e^I)^T \mathbf{S}^I \boldsymbol{\sigma}_e^I dA_e^I \\ & - \oint_{l_E} (\mathbf{n}^E \boldsymbol{\sigma}_e^M)^T \tilde{\mathbf{u}}_e^E dl \\ & + \oint_{l_{MI}} (\mathbf{n}^{MI} (\boldsymbol{\sigma}_e^M - \boldsymbol{\sigma}_e^I))^T \tilde{\mathbf{u}}_e^I dl \\ & + \oint_{l_T} \bar{\mathbf{T}}^T \tilde{\mathbf{u}}_e^E dl, \end{aligned} \quad (2)$$

where the variables with the superscripts M and I correspond to the interior of the matrix and inclusion phases, respectively, while those with superscripts E and MI refer to the variables on the element boundary and internal matrix-inclusion interface, respectively.  $\boldsymbol{\sigma}$  is the stress field within the matrix or the inclusion.  $\mathbf{S}$  is the elastic compliance matrix;  $A$  represents the area of the matrix or the inclusion.  $l_E$ ,  $l_{MI}$ , and  $l_T$  represent the displacement boundary of the element, the interface of matrix-inclusion, and traction boundary, respectively.  $\tilde{\mathbf{u}}$  represents the compatible displacement fields on the boundary of element or inclusion.  $\bar{\mathbf{T}}$  represents the prescribed tractions on the boundary  $l_T$ .  $\mathbf{n}$  is the outward

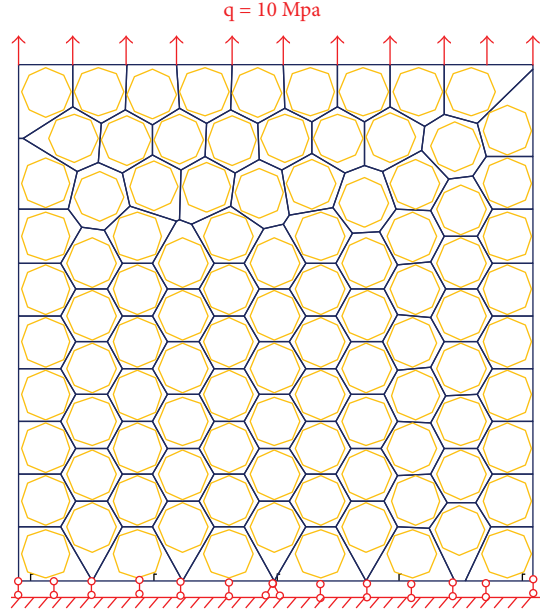


FIGURE 2: A RVE with 100 inclusions.

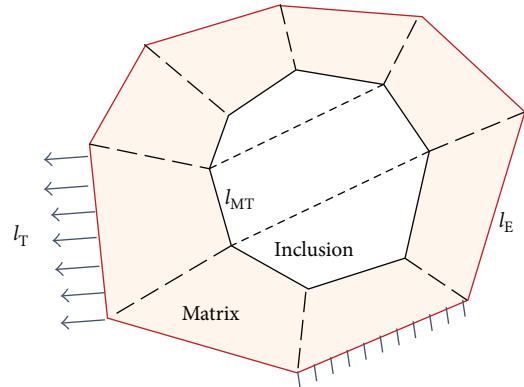


FIGURE 3: A typical Voronoi cell element with an octagonal inclusion.

normal unit vector of the element boundary or matrix-inclusion interface.

The displacement field  $\mathbf{u}$  is interpolated by using the nodal displacements  $\mathbf{q}$  and the boundary displacement interpolation functions  $\mathbf{L}(\mathbf{u} = \mathbf{L}\mathbf{q})$ , while the stress components within the element are assumed to be compatible with the prescribed boundary tractions and satisfy the equilibrium conditions into the region neglecting the body forces. The stress field  $\boldsymbol{\sigma}$  is expressed as the polynomial functions of the  $x$  and  $y$  coordinates, by using complete forms of the stress airy functions. This results in the product of an interpolation matrix  $\mathbf{P}$ , which contains polynomial terms in the  $x$  and  $y$  coordinates variables as reported in [14], and unknown vectors of coefficients  $\boldsymbol{\beta}(\boldsymbol{\sigma}^{M/I} = \mathbf{P}^{M/I} \boldsymbol{\beta}^{M/I})$ . The  $\Pi_{mc}$  can be simplified as

$$\Pi_{mc}(\boldsymbol{\beta}, \mathbf{q}) = \frac{1}{2} \boldsymbol{\beta}^T \mathbf{H} \boldsymbol{\beta} - \boldsymbol{\beta}^T \mathbf{G} \mathbf{q}. \quad (3)$$

The matrices  $\mathbf{H}$  and  $\mathbf{G}$  are defined as

$$\mathbf{H} = \begin{bmatrix} \mathbf{H}^M & \mathbf{0} \\ \mathbf{0} & \mathbf{H}^I \end{bmatrix}, \quad (4)$$

$$\mathbf{G} = \begin{bmatrix} \mathbf{G}^M & -\mathbf{G}^{MI} \\ \mathbf{0} & \mathbf{G}^I \end{bmatrix},$$

where

$$\mathbf{H}^{M/I} = \int_{A_{M/I}} [\mathbf{P}^{M/I}]^T \mathbf{S}^{M/I} \mathbf{P}^{M/I} dA, \quad (5)$$

$$\mathbf{G}^{E/MI/II} = \int_{I_{E/M/I}} [\mathbf{P}^{M/M/I}]^T [\mathbf{n}^{E/MI/I}]^T \mathbf{L}^{E/MI/I} dS. \quad (6)$$

Considering the stationary condition of the total complementary energy, we can get  $\partial \Pi_{mc} / \partial \boldsymbol{\beta} = 0$ . Consequently, the vector  $\boldsymbol{\beta}$  is expressed as

$$\boldsymbol{\beta} = \mathbf{H}^{-1} \mathbf{G} \mathbf{q}. \quad (7)$$

Substituting (7) into (3), with respect to the displacement  $\mathbf{q}$ , the expression of the stiffness matrix of the element is obtained as

$$\mathbf{K}_e = \mathbf{G}^T \mathbf{H}^{-1} \mathbf{G}. \quad (8)$$

Assembling stiffness matrices of each element,

$$\mathbf{K} = \sum_{i=1}^n (\mathbf{K}_e)_i. \quad (9)$$

The nodal displacements are the solutions to the following:

$$\mathbf{K} \mathbf{q} = \mathbf{Q}. \quad (10)$$

The Lagrange multiplier method is used to impose additional constraints to avoid rigid body displacement at the interface  $I_{MT}$ . The inner node displacements  $\mathbf{q}^I$  can be represented by the element boundary nodal displacements  $\mathbf{q}^E$ , while the inner node displacements are not affected by other elements directly. Therefore, the stiffness matrix of elements and corresponding mechanical load vectors can be eliminated to reduce the computing scale as follows:

$$\mathbf{K}_E^* = \mathbf{K}_{11} - \mathbf{K}_{12} \mathbf{K}_{22}^{-1} \mathbf{K}_{12}^T, \quad (11)$$

$$\mathbf{Q}^* = \mathbf{F}_{out} - \mathbf{K}_{12} \mathbf{K}_{22}^{-1} \mathbf{F}_{in},$$

where

$$\mathbf{K}_{11} = [(\mathbf{G}^E)^T (\mathbf{H}^M)^{-1} \mathbf{G}^E],$$

$$\mathbf{K}_{12} = [-(\mathbf{G}^E)^T (\mathbf{H}^M)^{-1} \mathbf{G}^{MI} \left\{ \left\{ (\boldsymbol{\varphi}^E)^T \boldsymbol{\varphi}^E \right\}^{-1} (\boldsymbol{\varphi}^E)^T \right\}],$$

$$\mathbf{K}_{22} = [(\mathbf{G}^{MI})^T (\mathbf{H}^M)^{-1} \mathbf{G}^{MI} + (\mathbf{G}^{II})^T (\mathbf{H}^I)^{-1} \mathbf{G}^{II} - \left\{ (\boldsymbol{\varphi}^I)^T \boldsymbol{\varphi}^I \right\}^{-1} (\boldsymbol{\varphi}^I)^T], \quad (12)$$

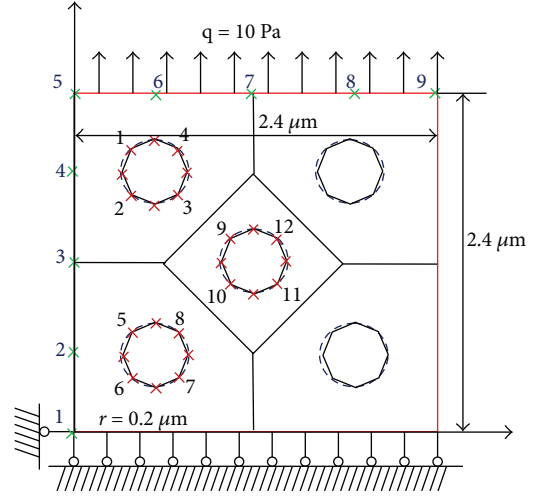


FIGURE 4: RVE model with five inclusions.

where  $\boldsymbol{\varphi}$  is the matrix to restrain the rigid body displacements and can be expressed as

$$\boldsymbol{\varphi} = \begin{bmatrix} 1 & 0 & 1 & 0 & \cdots & 1 & 0 \\ 0 & 1 & 0 & 1 & \cdots & 0 & 1 \\ -y_1 & x_1 & -y_2 & x_2 & \cdots & -y_n & x_n \end{bmatrix}^T. \quad (13)$$

**2.3. Homogenization Methods.** As shown in Figure 3, the inclusion and matrix domains of a 2D Voronoi cell element can be divided into triangular and quadrilateral integration regions, respectively. The mean stress and the mean strain are related to the values of every integration cell and can be obtained from the homogenization theory [7]:

$$\bar{\sigma}_{ij} = \sum_{m=1}^{N_{tri}} \bar{\sigma}_m^{tri} \frac{S_m^{tri}}{S_{RVE}} + \sum_{n=1}^{N_{quad}} \bar{\sigma}_n^{quad} \frac{S_n^{quad}}{S_{RVE}}, \quad (14)$$

$$\bar{\epsilon}_{ij} = \sum_{m=1}^{N_{tri}} \bar{\epsilon}_m^{tri} \frac{S_m^{tri}}{S_{RVE}} + \sum_{n=1}^{N_{quad}} \bar{\epsilon}_n^{quad} \frac{S_n^{quad}}{S_{RVE}},$$

where  $N_{tri}$  ( $N_{quad}$ ) is the quantity of triangular (quadrangular) elements,  $\bar{\sigma}_m^{tri} / \bar{\epsilon}_m^{tri}$  ( $\bar{\sigma}_n^{quad} / \bar{\epsilon}_n^{quad}$ ) is the mean stress/strain of each single triangular (quadrangular) element,  $S_m^{tri}$  ( $S_n^{quad}$ ) is the area of the  $m$ th ( $n$ th) triangular (quadrilateral) integration cell, and  $S_{RVE}$  is the total area of the RVE.

#### 2.4. Numerical Procedures

*Remark 1.* Octagons are used to simulate the circular inclusions. To construct the matrix  $\mathbf{H}$ , an integration subdivision scheme is needed to achieve the numerical area integration in (5). An integration subdivision scheme is proposed to reduce the number of integration regions and enhance the precision of numerical integration. As can be seen in Figure 3, the inclusion phase and the matrix phase is subdivided into 3 and 8 quadrilateral regions, respectively.

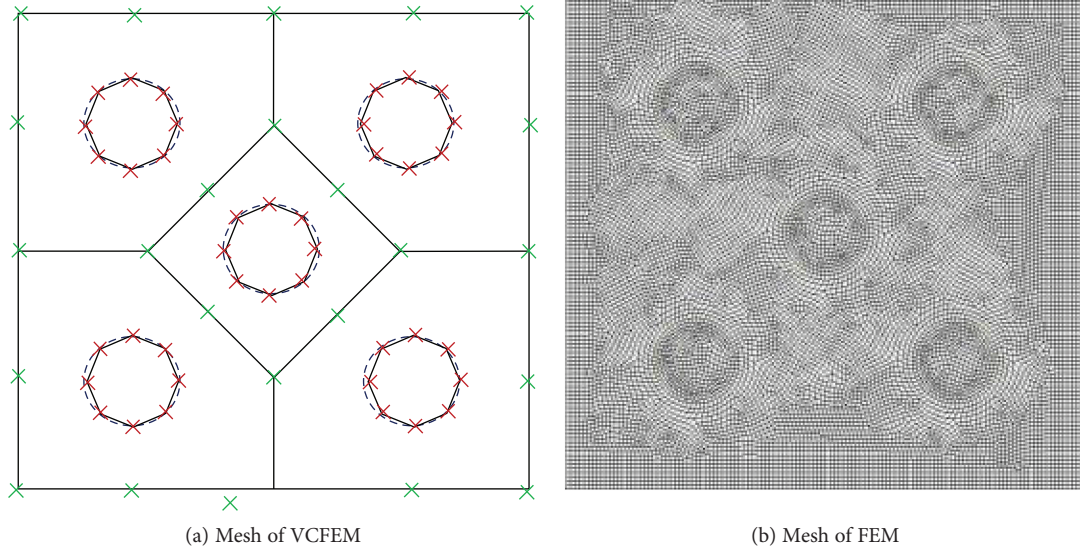


FIGURE 5: Mesh of two numerical methods.

*Remark 2.* The rank of the stiffness matrix is determined by the rank of matrix  $\mathbf{H}$  (refer to (8)). And the rank of matrix  $\mathbf{H}$  is equal to the number of the columns of matrix  $\mathbf{P}n_p$  (refer to (5)). For elements with more nodes, it is necessary to increase  $n_p$  to obtain enough rank. The value of  $n_p$  is adopted 25 to analyze octagon element. When  $n_p$  is equal to 25, the highest order of the power of matrix  $\mathbf{P}$  is equal to 4. As shown in (5), the Gauss integral with eight points is used in the calculation of matrix  $\mathbf{H}$  to conquer the ill-conditioned problem of the stiffness matrix [23].

### 3. Numerical Examples

#### 3.1. Result Validation

*3.1.1. Displacement Analysis.* In order to verify the applicability of the Voronoi cell element method developed, the displacement of a heterogeneous material with five inclusions subjected to uniformly tensile load is considered in this example (Figure 4). It is computed using VCFEM, and the results are compared with those obtained from the displacement-based FEM software Nastran. The matrix material is the following: Young’s modulus  $E = 1000$  Pa and Poisson’s ratio  $\nu = 0.2$ . The inclusion material is the following: Young’s modulus  $E = 3000$  Pa and Poisson’s ratio  $\nu = 0.2$ . A uniform tensile stress  $q = 10$  Pa at the top of the model is considered. Displacement constraints are imposed on the bottom side of the plate in the vertical direction. The center coordinates of five inclusions are the following:  $(0.6 \mu\text{m}, 0.6 \mu\text{m})$ ,  $(1.8 \mu\text{m}, 0.6 \mu\text{m})$ ,  $(1.2 \mu\text{m}, 1.2 \mu\text{m})$ ,  $(0.6 \mu\text{m}, 1.8 \mu\text{m})$ , and  $(1.8 \mu\text{m}, 1.8 \mu\text{m})$ .

The RVE model is subdivided into 5 cells used in Voronoi tessellation as shown in Figure 5(a). The RVE model is meshed by FEM in the commerce procedure Patran as well. There are 15,062 quadrilateral elements as shown in Figure 5(b).

TABLE 1: Comparison of two methods’ displacement results in load direction.

Node	VCFEM ( $\mu\text{m}$ )	FEM ( $\mu\text{m}$ )	Error*
Matrix node			
1	0	0	—
2	0.005820	0.005598	3.97%
3	0.011190	0.010841	3.22%
4	0.016790	0.016027	4.76%
5	0.022840	0.021831	4.62%
6	0.021620	0.020608	4.91%
7	0.021960	0.020928	4.93%
8	0.021620	0.020608	4.91%
9	0.022840	0.021831	4.62%
Matrix-inclusion interface node			
1	0.01584	0.01568	1.03%
2	0.01514	0.01472	2.89%
3	0.01594	0.01539	3.57%
4	0.01662	0.01634	1.72%
5	0.00543	0.00519	4.56%
6	0.00442	0.00426	3.88%
7	0.00493	0.00504	2.17%
8	0.00592	0.00591	0.14%
9	0.01058	0.01017	4.00%
10	0.00980	0.00937	4.54%
11	0.01063	0.01017	4.49%
12	0.01130	0.01100	2.73%

\*Error =  $|\text{VCFEM} - \text{FEM}|/\text{FEM} \times 100\%$ .

Table 1 shows the comparisons of the displacements of nodes on matrix boundary and matrix-inclusion interface in the loading direction. The results computed by the VCFEM and Nastran show a good agreement with each

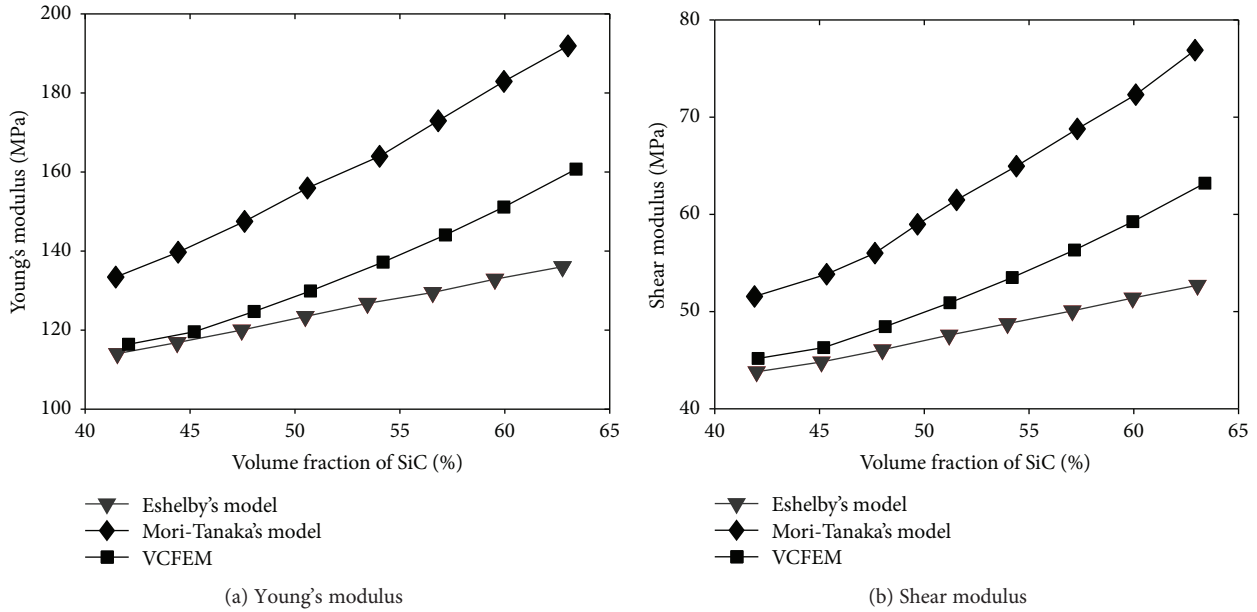


FIGURE 6: Effective modulus of aluminum-SiC composites versus the  $V_f$  of SiC.

other. The maximum relative error is less than 5.0%. In consideration, the stiffness matrix obtained by the displacement finite element method based on the minimum principle of potential energy is greater than the real stiffness matrix. So its displacement results are smaller than real displacement results. VCFEM is based on the minimum principle of residual energy. The stiffness matrix obtained by VCFEM is smaller than the real stiffness matrix. So its displacement results are greater than real displacement results. The error between the two displacement results is acceptable.

**3.1.2. Modulus Analysis.** Furthermore, another example is adopted to verify the correctness of the combined method. The effective Young's modulus and shear modulus are analyzed for several volume fractions of the aluminum-SiC composites using two theoretical models and the proposed method [24]. The VCFEM models were generated by using the program introduced in Section 2 and consisted of 100 hybrid elements containing polygonal inclusions as shown in Figure 2. A uniform tensile stress  $q = 10$  MPa at the top of the model is considered. Appropriate displacement constraints are imposed on the bottom side of the plate in the vertical direction. The material of the matrix is aluminum:  $E = 70.576$  GPa and  $\nu = 0.33$ . The material of the inclusion is SiC:  $E = 450.0$  GPa and  $\nu = 0.17$ .

It is clear from Figure 6 that those curves, respectively, obtained by these three methods have the same change trend. Eshelby's model and Mori-Tanaka's model are based on simplifying assumptions. They can only determine a region of real solution. And the result obtained by VCFEM is between the results of two models. It indicates that the method can obtain an effective result and shows its potential in the prediction of mechanical properties of solid propellants.

**3.2. Effective Mechanical Properties of CSP.** In the following case, the effective mechanical properties of the CSP are

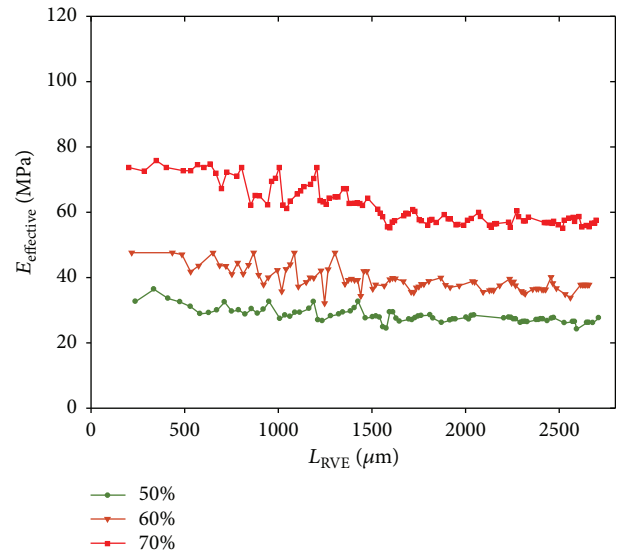


FIGURE 7: Effect of RVE size on effective modulus.

analyzed for different volume fractions of inclusion and component material properties with the RVE model of Section 3.1.2. The matrix will be assumed as an elastic material: Young's modulus  $E_M = 10$  MPa and Poisson's ratio  $\nu_M = 0.495$ . The AP particle material: Young's modulus,  $E_{\text{AP}} = 32.4$  GPa, Poisson's ratio  $\nu_{\text{AP}} = 0.14$ . The Al material: Young's modulus  $E_{\text{Al}} = 68.3$  GPa, Poisson's ratio  $\nu_{\text{Al}} = 0.33$ . The volume fraction of AP and Al particles, the modulus and Poisson's ratio of the matrix and inclusions, will be changed below to understand their relationship with effective mechanical properties. As shown in Figure 7, the effective moduli of different RVEs are calculated here to verify that the RVE size used is large enough. Keep the effective radius of particles ( $100 \mu\text{m}$ ) the same; increase the number

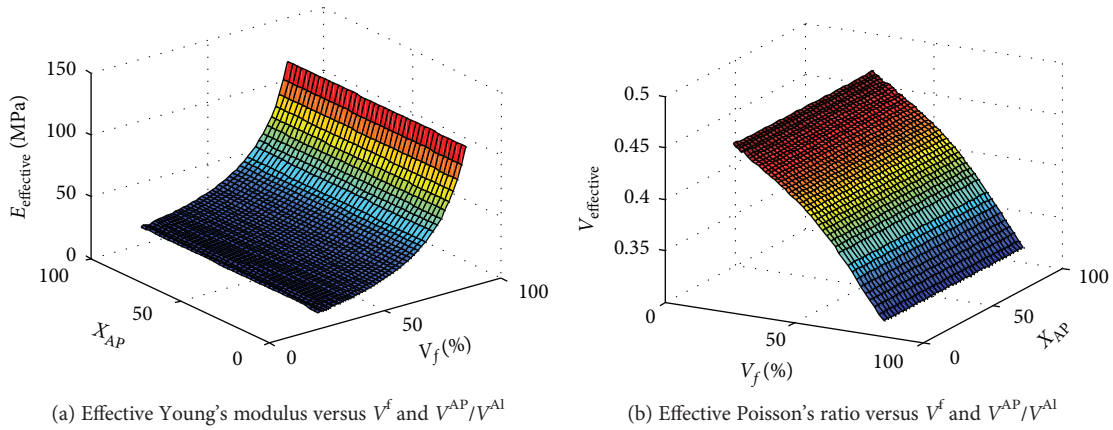


FIGURE 8: Effective properties of solid propellants versus  $V_f$  and  $V_{AP}/V_{Al}$ .

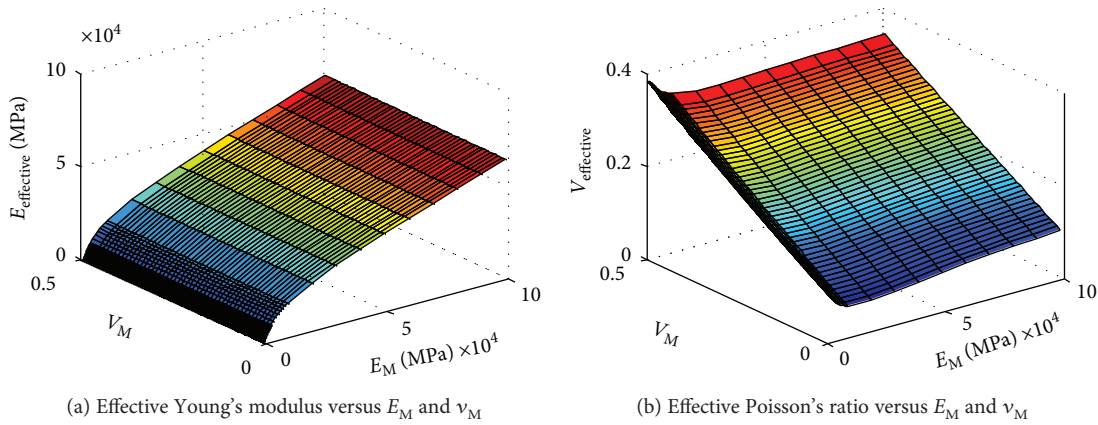


FIGURE 9: Effective properties of solid propellants versus  $E_M$  and  $\nu_M$ .

of particles to obtain RVEs with different sizes. The results showed that when the RVE size is greater than  $1500 \mu\text{m}$  (contains 48 inclusion particles when the volume fraction is 60%), its effective modulus remained stable. The model used below contains 100 inclusions (as shown in Figure 2), whose size is large enough to ignore the size effect of RVE here. A uniform tensile stress  $q = 10 \text{ MPa}$  at the top of the model is considered. Appropriate displacement constraints are imposed on the bottom side of the plate in the vertical direction.

**3.2.1. Effect of Inclusions' Volume Fraction.** The mechanical properties of composites with different volume fractions of AP and Al particles are calculated to study the effect of particle volume fraction. The changing of volume fraction depends on the changing of the size of RVE. The value of  $V_{AP}/V_{Al}$  varies with the quantity of AP cell elements  $x_{AP}$ . The 3D graphs in Figure 7 display the relationship between the effective properties and the volume fraction of inclusions  $V_f$  and  $V_{AP}/V_{Al}$ .

Figure 8(a) illustrates an upward trend with the increase of volume fraction of inclusion  $V_f$ . Upon further analysis, we can note that the effective modulus is closed to the modulus of the matrix when the  $V_f$  is less than 60% and, with the increase of  $V_f$ , the effective modulus increases more rapidly. Figure 8(b) illustrates a downward trend with the increase of

$V_f$ . The ratio of  $V_{AP}/V_{Al}$  describes little influence on the effective properties.

With the increase of the volume fraction of inclusion, the mechanical properties of composites, such as a composite solid propellant, is closing to properties of the inclusion materials. When the differences between the properties of two inclusion materials are smaller than the differences between theirs and the matrix's, the variation of the proportion of different inclusions is not obvious.

**3.2.2. Effect of Matrix's Material Properties.** The mechanical properties of composites with different modulus and Poisson's ratio of the matrix are calculated to study the effect of the matrix material. The particle volume fraction remains at 65% invariability in this case. The 3D graphs in Figure 8 display the relationship between the effective properties and the matrix modulus  $E_M$  and matrix Poisson's ratio  $\nu_M$ .

It can be seen in Figure 9(a) that the effective modulus has a positive relation with  $E_M$ , while the influence of  $\nu_M$  can be ignored. Figure 9(b) shows that the effective Poisson's ratio has a positive linear relation with  $E_M$ . Furthermore, the effective Poisson's ratio decreases slightly with the increase of  $E_M$ . But with the increase of the matrix modulus, the decreasing trend is more and more inconspicuous.

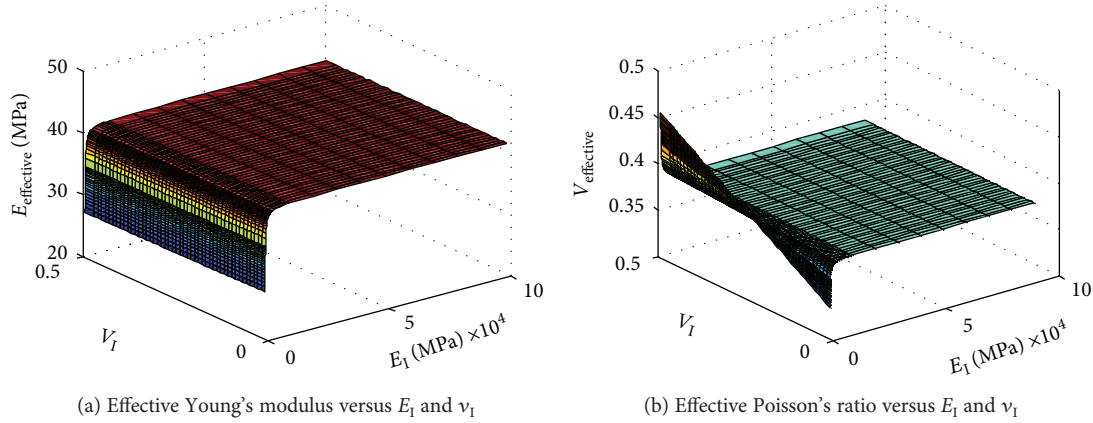


FIGURE 10: Effective properties of solid propellants versus  $E_I$  and  $\nu_I$ .

The variation of the modulus of the matrix has an effect on both the effective modulus and the effective Poisson's ratio of the CSP, when the variation of the Poisson's ratio of the matrix has a linear effect on the effective Poisson's ratio of the CSP mainly.

**3.2.3. Effect of Inclusion's Material Properties.** The mechanical properties of composites with different modulus and Poisson's ratio of inclusion are calculated to study the effect of the inclusion material. The particle volume fraction remains at 65% invariability in this case. The 3D graphs in Figure 10 display the relationship between the effective properties and the inclusion modulus  $E_I$  and the inclusion Poisson's ratio  $\nu_I$ .

From Figure 10(a), the effective modulus increases sharply with the increase of  $E_I$  when the ratio of  $E_I/E_M$  is less than 10. As  $E_I$  continues to increase, the effective modulus keeps constant steadily. The variation of  $\nu_I$  has no significant effect on effective modulus. From Figure 10(b), we can see clearly that a dramatical change has taken place in the growth process of  $E_I$ . The effective Poisson's ratio increases linearly with  $\nu_I$ . But the slope of the effective Poisson's ratio and  $\nu_I$  is declining with the increase of  $E_I$ .

Only when the modulus of inclusion is matched by the modulus of the matrix, the effective modulus and effective Poisson's ratio are affected by the modulus of inclusion significantly. However, the modulus of inclusion of the CSP is larger than the matrix's. Hence, the variation of modulus of inclusion does not have as obvious influence as expected.

## 4. Conclusion

The effective modulus and Poisson's ratio of the CSP, which are closely related to the volume fraction and material property of each component, are the critical material parameters to analyze the structural integrity of propellant grains. A strategy for constructing RVE models of highly packed particulate composites is presented here, which is adopted by VCFEM appropriately. A numerical programming method combined with the VCFEM and homogenization method is proposed to investigate the relationship between the microstructural morphology and the effective properties of the

CSP. Based on the examples mentioned in the above sections, the following conclusions can be drawn:

- (1) The mechanical properties of the CSP are significantly affected by the volume fraction of inclusions, with the increase of the volume fraction of inclusion; the mechanical properties of composites, such as a composite solid propellant, are closing to the properties of the inclusion materials. However, the variation of the proportion of different inclusions has a minor influence. Since the properties different between the inclusion and the matrix are very large, a small change of inclusion's properties does not have a significant effect on the overall effective properties.
- (2) Except that the modulus and Poisson's ratio of the matrix directly influence the effective modulus and Poisson's ratio of the CSP, respectively, the variation of the matrix modulus has modest influences on the effective Poisson's ratio of the CSP.
- (3) The effective properties are affected by the modulus of inclusion significantly only when the moduli of the inclusion and matrix are close. However, as for the CSP, when the modulus of the inclusion is much larger than that of the matrix, the effects of inclusion's material properties are not obvious as expected.

## Conflicts of Interest

The authors declare that they have no conflicts of interest.

## Acknowledgments

This study was supported by the Science Project of the National University of Defense Technology.

## References

- [1] L.-L. Shen, Z.-B. Shen, H.-Y. Li, and Z.-Y. Zhang, "A Voronoi cell finite element method for estimating effective mechanical properties of composite solid propellants," *Journal of Mechanical Science and Technology*, vol. 31, no. 11, pp. 5377–5385, 2017.

- [2] Z. Hashin and S. Shtrikman, "A variational approach to the theory of the elastic behaviour of multiphase materials," *Journal of the Mechanics and Physics of Solids*, vol. 11, no. 2, pp. 127–140, 1963.
- [3] T. Steinkopff and M. Sautter, "Simulating the elasto-plastic behavior of multiphase materials by advanced finite element techniques part II: simulation of the deformation behavior of Ag-Ni composites," *Computational Materials Science*, vol. 4, no. 1, pp. 15–22, 1995.
- [4] A. Malyarenko and M. Ostoja-Starzewski, "A random field formulation of Hooke's law in all elasticity classes," *Journal of Elasticity*, vol. 127, no. 2, pp. 269–302, 2017.
- [5] A. Malyarenko and M. Ostoja-Starzewski, "Spectral expansions of homogeneous and isotropic tensor-valued random fields," *Zeitschrift für angewandte Mathematik und Physik*, vol. 67, no. 3, 2016.
- [6] J. Szafran and M. Kamiński, "Bridges for pedestrians with random parameters using the stochastic finite elements analysis," *International Journal of Applied Mechanics and Engineering*, vol. 22, no. 1, pp. 175–197, 2017.
- [7] J. W. Zhang, S. J. Zhi, and B. Sun, "Estimation of thermophysical properties of solid propellants based on particle packing model," *Science China Technological Sciences*, vol. 56, no. 12, pp. 3055–3069, 2013.
- [8] M. Plaud, S. Gallier, and M. Morel, "Simulations of heterogeneous propellant combustion : effect of particle orientation and shape," *Proceedings of the Combustion Institute*, vol. 35, no. 2, pp. 2447–2454, 2015.
- [9] J. Yang and C. Liu, "A numerical approach for the simulation of composite solid propellant," in *2009 Second International Conference on Information and Computing Science*, pp. 50–52, Manchester, UK, 2009.
- [10] S. J. Zhi, B. Sun, and J. W. Zhang, "Multiscale modeling of heterogeneous propellants from particle packing to grain failure using a surface-based cohesive approach," *Acta Mechanica Sinica*, vol. 28, no. 3, pp. 746–759, 2012.
- [11] K. Matous and P. H. Geubelle, "Multiscale modelling of particle debonding in reinforced elastomers subjected to finite deformations," *International Journal for Numerical Methods in Engineering*, vol. 65, no. 2, pp. 190–223, 2006.
- [12] K. Matous, H. Inglis, X. Gu, D. Rypl, T. Jackson, and P. Geubelle, "Multiscale modeling of solid propellants: from particle packing to failure," *Composites Science and Technology*, vol. 67, no. 7-8, pp. 1694–1708, 2007.
- [13] S. Ghosh and S. N. Mukhopadhyay, "A two-dimensional automatic mesh generator for finite element analysis for random composites," *Computers & Structures*, vol. 41, no. 2, pp. 245–256, 1991.
- [14] S. Ghosh and S. N. Mukhopadhyay, "A material based finite element analysis of heterogeneous media involving Dirichlet tessellations," *Computer Methods in Applied Mechanics and Engineering*, vol. 104, no. 2, pp. 211–247, 1993.
- [15] S. Ghosh, K. Lee, and S. Moorthy, "Multiple scale analysis of heterogeneous elastic structures using homogenization theory and Voronoi cell finite element method," *International Journal of Solids and Structures*, vol. 32, no. 1, pp. 27–62, 1995.
- [16] S. Ghosh and S. Moorthy, "Elastic-plastic analysis of arbitrary heterogeneous materials with the Voronoi cell finite element method," *Computer Methods in Applied Mechanics and Engineering*, vol. 121, no. 1–4, pp. 373–409, 1995.
- [17] S. Ghosh and S. Moorthy, "Particle fracture simulation in non-uniform microstructures of metal–matrix composites," *Acta Materialia*, vol. 46, no. 3, pp. 965–982, 1998.
- [18] S. Ghosh, J. Bai, and D. Paquet, "Homogenization-based continuum plasticity-damage model for ductile failure of materials containing heterogeneities," *Journal of the Mechanics and Physics of Solids*, vol. 57, no. 7, pp. 1017–1044, 2009.
- [19] S. Ghosh, "Adaptive hierarchical-concurrent multiscale modeling of ductile failure in heterogeneous metallic materials," *JOM*, vol. 67, no. 1, pp. 129–142, 2015.
- [20] L. Bruno, F. M. Furguele, and C. Maletta, "A hybrid method for the thermo-mechanical analysis of elastic cracks in two-dimensional heterogeneous materials," *Finite Elements in Analysis and Design*, vol. 43, no. 6-7, pp. 444–452, 2007.
- [21] M. Grujicic and Y. Zhang, "Determination of effective elastic properties of functionally graded materials using Voronoi cell finite element method," *Materials Science and Engineering: A*, vol. 251, no. 1-2, pp. 64–76, 1998.
- [22] M. Jiang, K. Alzebdeh, I. Jasiuk, and M. Ostoja-Starzewski, "Scale and boundary conditions effects in elastic properties of random composites," *Acta Mechanica*, vol. 148, no. 1-4, pp. 63–78, 2001.
- [23] S. Moorthy and S. Ghosh, "A model for analysis of arbitrary composite and porous microstructures with Voronoi cell finite elements," *International Journal for Numerical Methods in Engineering*, vol. 39, no. 14, pp. 2363–2398, 1996.
- [24] X. Liu and J. Zhang, "The study of finite element method to predict effective elastic modulus of composites," *Journal of Shenyang Institute of Engineering (Natural Science)*, vol. 5, no. 2, pp. 175–179, 2009.

## Research Article

# Analytical Study on Deformation and Structural Safety of Parafoil

Longfang Wang  and Weiliang He 

*School of Astronautics, Beihang University, Beijing 100191, China*

Correspondence should be addressed to Weiliang He; [heweiliang@buaa.edu.cn](mailto:heweiliang@buaa.edu.cn)

Received 29 December 2017; Revised 26 February 2018; Accepted 13 March 2018; Published 1 April 2018

Academic Editor: Filippo Berto

Copyright © 2018 Longfang Wang and Weiliang He. This is an open access article distributed under the Creative Commons Attribution License, which permits unrestricted use, distribution, and reproduction in any medium, provided the original work is properly cited.

This study focuses on the cell bump distortion and bearing capacity of parafoil structure. Based on the mechanical properties of the membrane structure, the spanwise model of parafoil inflation was established and verified by comparing with the fluid-structure interaction (FSI) results. Because the internal pressure is very low, the chordwise stiffness is mainly generated by suspending lines. The chordwise model of inflated parafoil was established in consideration of elastic force and aerodynamic force. The results show that the cell is slenderer; the canopy surface is smoother; the aerodynamic load has a light effect on the shrinkage and bump ratios; when the cell width is constant, the critical dynamic pressure reduces  $k$  times with the  $k$  times increasing in parafoil area; and the design parameters of the first-row line OA have significant effects on the structural stiffness of inflated parafoil. The analytical model is useful for the weakening deformation design and the safety discussion of large parafoil for rocket booster recovery.

## 1. Introduction

The parafoil is a flexible wing maintaining the aerodynamic shape with ram air in cells and decelerating the payload drop with aerodynamic lift. The aerodynamic force on canopy can be changed by pulling down the steering ropes to achieve steerable flight. As a kind of steerable aerodynamic decelerator, parafoil gets extensive attention in the rocket booster recovery. The parafoil is made by flexible textile material and presents large deformation during flight. When used in booster recovery, the parafoil has a tremendous area and bears a large wing load. This puts forward higher requirements for the bearing capacity of parafoil structure. Therefore, it is necessary to investigate the deformation and structural stiffness of large parafoils to improve their performance and safety.

The deformed surface geometry of a parafoil was presented by a video-based photogrammetry during tethered testing in a low-speed tunnel [1, 2]. Due to the fact that this kind of test presents a high cost, numerical simulation has become a popular way to analyze the deformation of parafoils. Kalro et al. set the shape of deformed canopy according to the drop test and analyzed the motion of

opening process [3]. Eslambolchi and Johari extracted the inflated canopy geometry from close-up images of the MC-4 canopy during a flight and computed the flow field around the deformed canopy [4]. Ibos et al. simulated the fluid-structure interaction problem of a parafoil using SINPA software [5]. Kalro and Tezduyar calculated the shape of a parafoil in a steady flight using the parallel coupling algorithm for fluid-structure coupling using finite element methods [6]. Fogell et al. analyzed the fluid-structure interaction problem of a single-cell parafoil model [7]. Altmann studied the deformation of canopy by the potential flow theory and the cable finite element [8, 9]. Peralta and Johari investigated the geometry of a fully inflated canopy in steady flight using a prescribed pressure distribution [10]. Mosseev developed a series of software to simulate the aerodynamic deformation of a canopy [11]. The results indicate that the projected area of an inflated canopy is 18% smaller than the area of the initial geometry.

The numerical simulation of the fluid-structure interaction in the parafoil is very complicated and time-consuming. It is difficult to carry out a numerical simulation while designing a parafoil. Besides, the trade studies on design variables cannot be clearly discussed only by the

analysis of simulation examples. The deformation and safety of the parafoil structure during the flight should be included in the design process in order to improve the flight performance of the parafoil. It is important to find a design theory which is able to guide the manufacture process of large parafoils. The novelty of the current study is to establish the theoretical spanwise and chordwise model for the design of parafoil. Further, the effect of design variables is studied.

## 2. Spanwise Structure Model

As is shown in Figure 1, the inflating deformation of parafoil is mainly embodied as the spanwise bumps. This is determined by the mechanical properties of the membrane structure. The widthwise projection of the ideal cell is flat, but the lengthwise projection is curved. When the cell is ballooning, the widthwise curvature changes more than the lengthwise curvature to bear pressure load. The failure of spanwise structure is the primary failure mode of wingtip collapse. Hence, the chordwise deformation and stress can be neglected in the two-dimensional deformation model of canopy structure.

The stress of membrane structure is expressed below [12]:

$$\frac{\sigma_1}{r_1} + \frac{\sigma_2}{r_2} = \frac{P}{t}, \quad (1)$$

where  $\sigma_1$  and  $\sigma_2$  are the radial and latitudinal stresses, respectively;  $r_1$  and  $r_2$  are the radial and latitudinal radius of curvature, respectively;  $P$  is the differential pressure; and  $t$  is the thickness. In the two-dimensional model, (1) is simplified:

$$\frac{\sigma}{r} = \frac{P}{t}, \quad (2)$$

where  $\sigma$  is the canopy stress, and  $r$  is the widthwise radius of curvature. The widthwise variation of pressure is neglected, and the canopy stress is constant in each cell, so the cells must be inflated to a circular arc.

Figure 2 presents the 2D geometrical configuration of balloon cells. The ribs are simplified as straight lines and the upper and lower surfaces are simplified as a circular arc with radius  $r$ . The cell coordinate system is established to analyze the deformation of the cell. The  $y$ -axis is parallel to the rib and the  $x$ -axis is perpendicular to the rib. When the parafoil is in steady flight, every cell structure is in equilibrium, and the vector sum of the forces acting upon it is zero. Because the lift of the parafoil is mainly provided by the upper surface, the aerodynamic pressure load is entirely applied on the upper surface. The pressure on the lower surface is equal to the stagnation pressure. By analyzing the forces on the rib, upper and lower surface, the equations are listed as follows:

$$T_1 \cos \varphi + T_2 \cos \varphi = P_2 h, \quad (3)$$

$$2T_1 \sin \varphi = P_1 w, \quad (4)$$

$$2T_2 \sin \varphi = P_2 w, \quad (5)$$



FIGURE 1: Photograph of parafoil in flight.

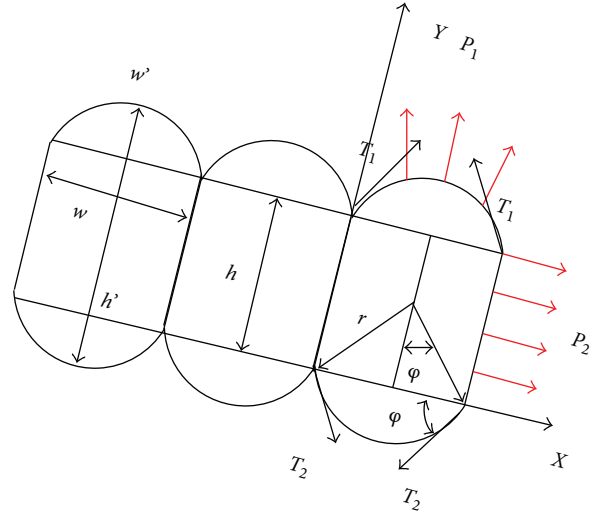


FIGURE 2: Two-dimensional model of balloon cells.

where  $T_1$  and  $T_2$  represent the tensions per unit chord of upper and lower surface, respectively;  $P_1$  and  $P_2$  represent the differential pressure on upper surface and the stagnation pressure, respectively;  $h$  and  $w$  represent the height and width of the cell, respectively; and  $\varphi$  represents the half of the central angle.

As is mentioned above, the difference between  $P_1$  and  $P_2$  is the aerodynamic pressure load:

$$P_1 = P_2 + \frac{1}{2} CL' \rho V^2 = \left(1 + CL'\right) \frac{1}{2} \rho V^2 = \left(1 + CL'\right) P_2. \quad (6)$$

Here,  $\rho$  is the air density;  $V$  is the parafoil velocity; and  $CL'$  is the lift coefficient defined in the cell coordinate system.

Equation (5) is subtracted from (4) and combined with (6), resulting in (7) below:

$$T_1 = T_2 + \frac{(P_1 - P_2)w}{2 \sin \varphi} = T_2 + CL' \frac{P_2 w}{2 \sin \varphi} = \left(1 + CL'\right) T_2. \quad (7)$$

Equation (7) is substituted into (3), resulting in (8) below:

$$\left(2 + CL'\right) T_2 \cos \varphi = P_2 h. \quad (8)$$

Equation (9) can be derived by the division operation of (8) and (5):

$$\varphi = \text{atan} \left( \frac{w' 2 + CL'}{h} \right). \quad (9)$$

According to the geometric relationship shown in Figure 2, the ratio between the arc length  $w'$  and the width  $w$  can be indicated as follows:

$$r = \frac{w'}{2\varphi} = \frac{w}{2 \sin \varphi}, \quad (10)$$

$$\eta_1 = 1 - \frac{w}{w'} = 1 - \frac{\sin \varphi}{\varphi}, \quad (11)$$

$$\eta_2 = \frac{h' - h}{h} = \frac{2r(1 - \cos \varphi)}{h}, \quad (12)$$

where  $\eta_1$  and  $\eta_2$  are defined as the shrinkage ratio and the bump ratio of the cell, respectively. Because the cell height is mainly concentrated around the rib peak, the cell height of the parafoil is set as the thickness of the rib. The flexible lines can only restrict the relative position of the intersection point of the lines and the connection point of the ribs; therefore, the ribs can move easily on the arc whose center is the intersection point and radius is the line length. The move is similar to the contraction of the accordion and leads to a large difference between the deformed shape and the design shape of the parafoil.

To validate the spanwise model, the fluid-structure interaction (FSI) simulation using the commercial solver ANSYS has been carried out in our previous work [13]. The grid of the parafoil system is shown in Figure 3. The canopy is divided into triangular membrane elements. The two intersection points of the suspending lines are fixed, and in order to avoid the rigid body motion, the symmetrical boundary condition is applied in the middle of the parafoil. The internal and external pressure distributions on the canopy, which were calculated at the angle of attack of  $5^\circ$  using CFD method, were transferred to the canopy structure through mapping interpolation. To avoid divergence, the load was applied on the canopy in a way that it increased linearly with the substeps.

The deformed parafoil obtained from the fluid-structure interaction (FSI) simulation is presented in Figure 4. The deformation is not amplified, and its scale is in accordance with the geometric dimensioning of canopy. The bumps of cells are clearly visible. It can be seen from Figure 4(a) that the inflated canopy reduces the span which is equal to the width of two cells. The actual span in the flight reduced by 13% compared to the designed span. The maximum thickness of the airfoil Clark-Y18 is 18%*c*, but it will increase to 26%*c* after the bumps appear.

The cell ratio  $h/w$ , stagnation pressure  $P_2$ , thickness  $t$ , and cell lift coefficient  $CL'$  in the case shown in Figure 3 are 0.9, 61.25 Pa, 1 mm, and 0.55, respectively. These parameters are substituted into (9), (10), and (11), then the shrinkage ratio is 14.6% and has little

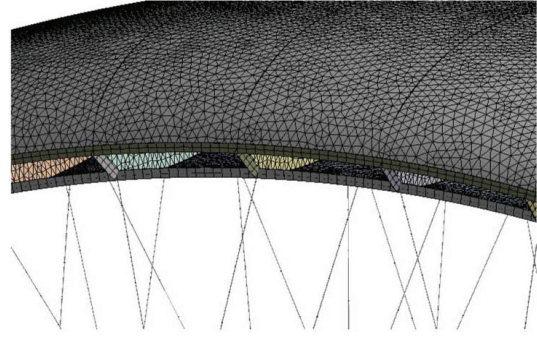


FIGURE 3: Meshes of the parafoil.

difference with the value of 13% presented earlier. The radius of curvature  $r$  for the cell is 0.1 m. The bump height  $h'$  is 26%*c* and is equal to the previous value of 26%*c*. A comparison of the two sets of shrinkage ratio and bump height validates the two-dimensional simplified model. The stress of the lower surface calculated by (2) is 6000 Pa, so the strain of the canopy is very small. The parafoil is a typical large deformation small-strain structure, and the deformation is determined by geometrical configuration rather than material characteristics.

The relationship between the shrinkage/bump ratios and the cell ratio  $h/w$  with different  $CL'$  values is plotted in Figure 5. When the cell ratio is 1.8, the bump ratio is very close to the wind tunnel test result 18%*c* to 23%*c* [7]. As can be seen from the curves, the cell is slenderer, the shrinkage ratio and bump ratio are smaller, and the canopy surface is smoother. This is why some high-performance paragliders are composed of numerous cells. When the cell ratio is greater than 2, the bump ratio changes little, so the design value of 2 is recommended. The cell ratio is decreased, and the shrinkage ratio is increased from the peak to the trailing edge, so the angle of sweepback shows up. The shrinkage and the bump ratios are increased a bit with the increase of  $CL'$ , and the effect of  $CL'$  is great at the medium cell ratio. It means that the aerodynamic shape of the parafoil will change a little with different angles of attack.

The shrinkage and bump ratios are ineradicable. Form rib peak to trailing edge, the cell ratio is monotonously decreasing, consequently, so is the shrinkage ratio. The canopy is made of pieces of cloth. If the pieces of upper and lower surface are designed to be the strips of uniform width, the parafoil is likely to be malformed. The ideal cells of uniform width become wide in the front and narrow in the back after ballooning. This generates the angle of sweepback described previously. In order to guarantee the spanwise appearance, the design of every cell upper and lower surfaces needs to provide margin. A piece of upper or lower surfaces is no longer a rectangular shape. The surcharge is computed by the shrinkage ratio along the chordwise for a  $CL'$  value of 0.55. A piece of wider and ideal lower surface for parafoil described previously is shown in Figure 6.

The ribs are made of textile material, so they can only bear tension. The expression for calculating the tension

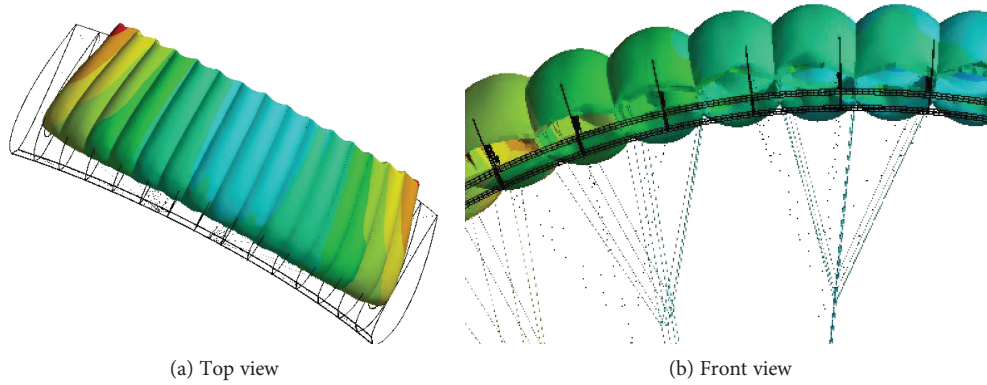


FIGURE 4: Deformed configuration of a parafoil.

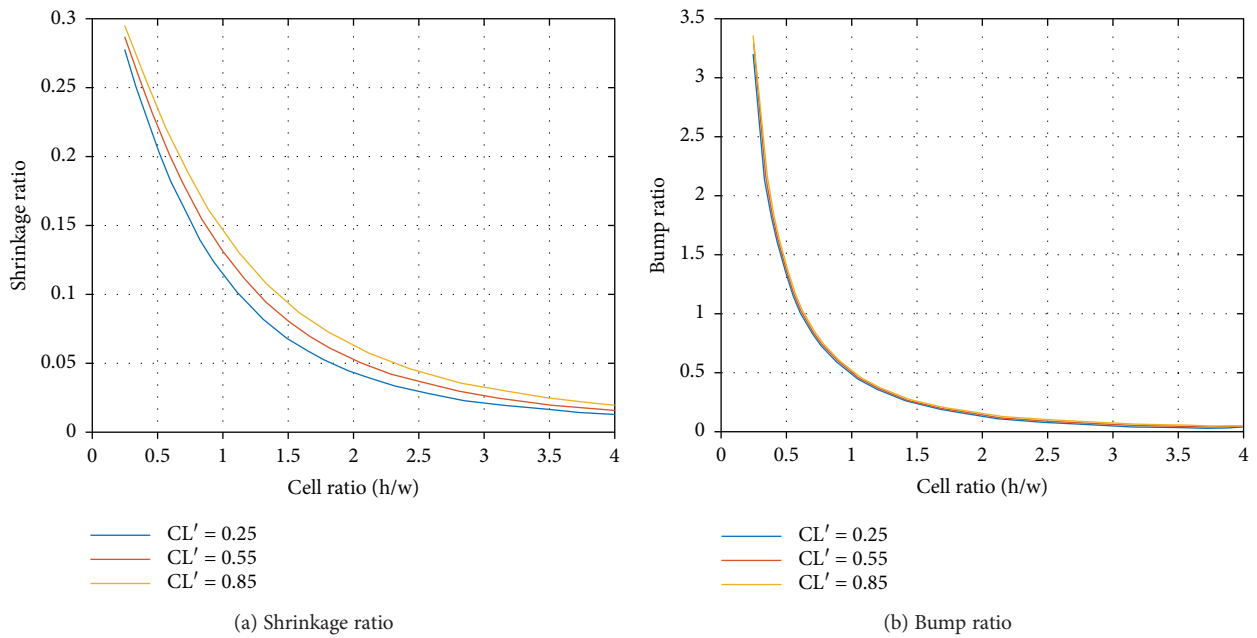


FIGURE 5: Relationship between shrinkage/bump ratio and cell ratio.

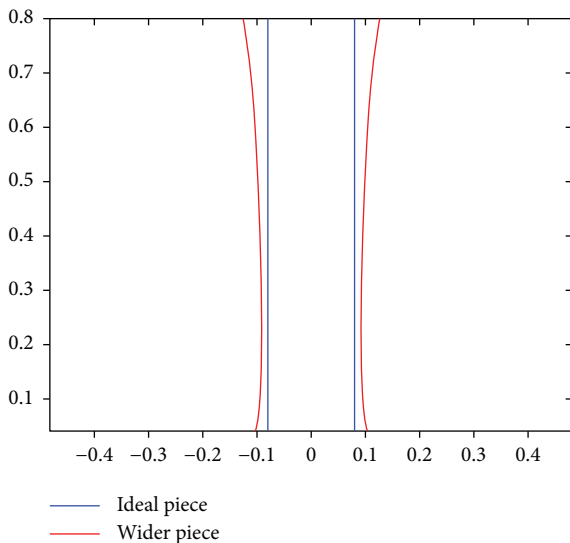


FIGURE 6: Pieces of ideal and wider lower surface.

per unit chord of the rib  $T_3$  can be derived from (4) and (5):

$$T_3 = 2T_1 \sin \varphi - 2T_2 \sin \varphi = (P_1 - P_2)w = CL'P_2w. \quad (13)$$

Apparently, the tension of the rib is the lift defined in the cell coordinate system. The physical significance is that the ribs and suspending lines are medium for the lift transmission from the upper surface to payload. Compared with the inflated wing [14], the internal pressure of the parafoil is too small, and the bearing capacity of inflated canopy without the tensile suspending line can be neglected. If the tensions of the ribs in some cells become zero, the ribs and suspending lines will be slacked, and the parafoil structure will collapse. According to (15), the critical pressure on the upper surface is  $CL'P_2$ . This critical pressure is not the normal aerodynamic load but the perturbation caused by crosswind. This illustrates that the parafoil with large wing loading has a high ability to resist wingtip collapse. For the flight parameters, the critical pressure is 33.7 Pa for the

deformed parafoil shown in Figure 4. This pressure is much lower than the differential pressure of the canopy, which is often considered the critical pressure of wingtip collapse in previous research.

The nonlinear buckling analysis for wingtip collapse of the deformed parafoil shown in Figure 4 was carried out. According to the relationship between the displacement and the load in Figure 7, the critical pressure on the wingtip is 32.9 Pa. The error between this critical pressure and the result above is 2.4%, showing that the two-dimensional model of wingtip collapse can reproduce the phenomena with a low margin of error.

### 3. Chordwise Structure Model

After the inflating deformation of cell, the parafoil can bear aerodynamic load. The inflated canopy should twist under the action of chordwise aerodynamic moment. Compared with the spanwise bumps, the torsion has a completely different mechanism. It is caused by the aerodynamic loading and varied with flow velocity. As is mentioned above, the bearing capacity of inflated canopy without the tensile suspending line can be neglected. The aerodynamic loads of each cell are directly transmitted to payload by the ribs and suspending lines attached on each cell. The force transmission between cells is negligible, so the analysis of the chordwise torsion can focus on a cell and the suspending lines. Hence, the torsion of parafoil can be simplified to two-dimensional chordwise model.

The two-dimensional chordwise sketch of parafoil is shown in Figure 8. Due to the constraint of line OB, the cell in front of line OB can rotate around point B. When the cell presents an upward rotation angle  $\theta$  under the aerodynamic moment, the line OA will be stretched and the elongation is  $l\theta$ ;  $l$  is the distance between points A and B. Hence, the elastic restoring moment of line OA is  $(l^2\theta/L_1)EA$ . Here,  $L_1$ ,  $E$ , and  $A$  are the length, elasticity modulus, and sectional area of line OA, respectively. The torsional rigidity of the cell is shown below:

$$K_\theta = \frac{l^2}{L_1} EA. \quad (14)$$

The initial angle of attack is  $\alpha_0$ , and the free-stream velocity is  $V$ . Due to the elasticity of parafoil structure, the new equilibrium at angle of attack  $\alpha = \alpha_0 + \theta$  will be established under aerodynamic load. The additional angle  $\theta$  is defined by torsional rigidity and aerodynamic load, but the aerodynamic load is also affected by  $\theta$ . According to aerodynamics, the aerodynamic load is composed of the lift force  $L$  applied on the aerodynamic center and the nearly invariable moment  $M_0$  about aerodynamic center. The lift  $L$  and the aerodynamic moment  $M$  about point B are shown below:

$$L = CL' qS = \frac{\partial CL'}{\partial \alpha} (\alpha_0 + \theta - \alpha_{z1}) qS, \quad (15)$$

$$M = M_0 + Lf = M_0 + \frac{\partial CL'}{\partial \alpha} (\alpha_0 + \theta - \alpha_{z1}) qSf. \quad (16)$$

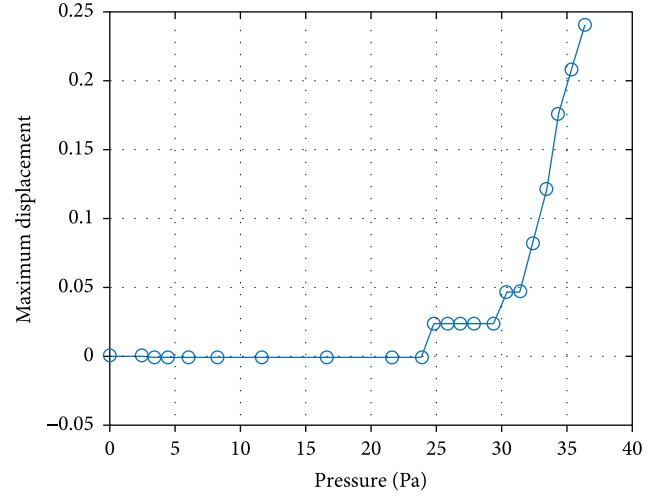


FIGURE 7: Load-displacement curve of deformed canopy.

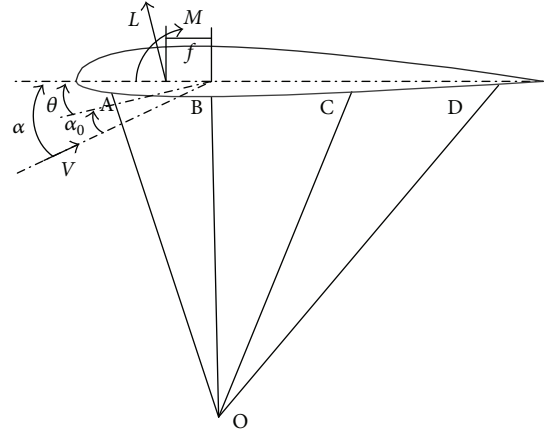


FIGURE 8: Pieces of ideal and wider lower surface.

Here,  $CL'$  is the lift coefficient defined in the cell coordinate system;  $q$  is the dynamic pressure;  $S$  is the reference area of the cell;  $\alpha_{z1}$  is the zero lift angle of attack; and  $f$  is the distance between the aerodynamic center and point B.

The aerodynamic moment is equal to the elastic moment, so the equilibrium equation can be written as below:

$$K_\theta \theta = M_0 + \frac{\partial CL'}{\partial \alpha} (\alpha_0 + \theta - \alpha_{z1}) qSf. \quad (17)$$

The term  $\theta$  is moved to the left:

$$\left( K_\theta - \frac{\partial CL'}{\partial \alpha} qSf \right) \theta = \frac{\partial CL'}{\partial \alpha} qSf (\alpha_0 - \alpha_{z1}) + M_0. \quad (18)$$

Hence, the expression of  $\theta$  is shown below:

$$\theta = \frac{\left( \frac{\partial CL'}{\partial \alpha} \right) qSf (\alpha_0 - \alpha_{z1}) + M_0}{K_\theta - \left( \frac{\partial CL'}{\partial \alpha} \right) qSf}. \quad (19)$$

When the dynamic pressure  $q$  reaches a particular value, the denominator in the equation becomes zero and  $\theta$  is infinity, and the parafoil structure will crash. The critical dynamic pressure  $q_D$  can be written as below:

$$q_D = \frac{K_\theta}{\left(\frac{\partial CL'}{\partial \alpha}\right) Sf} = \frac{l^2}{\left(\frac{\partial CL'}{\partial \alpha}\right) Sf L_1} EA. \quad (20)$$

This critical dynamic pressure is aerodynamic load of incoming flow, rather than the perturbation load for wingtip collapse discussed in Section 2. According to the equation above, when the cell width is constant, the critical dynamic pressure of the parafoil amplified  $k$  times reduces  $k$  times. The structure stability of a large parafoil needs special consideration. The similar conclusion can be drawn by the wind tunnel test [2].

The calculating example is a large rectangular parafoil used in rocket booster recovery. Its design parameters are presented as follows: the baseline airfoil is Clark-Y18, the span length is 48 m, and the chord length is 16 m. The front projection of the canopy is a quadrant arc and its radius is 32 m. There are four chordwise join points between the ribs and suspending lines on the lower aerofoil. The diameter of the lines is 3.2 mm and its material is Kevlar29. The elastic modulus of this material is 97 GPa. The lift-curve slope  $\frac{\partial CL'}{\partial \alpha}$  defined in the cell coordinate system is  $0.044 \text{ deg}^{-1}$  and  $f$  is 5%. According to (14), the torsional rigidity of the calculating example is 25,600 Nm. According to (20), the critical dynamic pressure is 5340 Pa. If the maximum dynamic pressure in booster recovery process is larger than 5340 Pa, the recovery mission is likely to fail. Increasing the section area of suspending lines can enlarge the critical dynamic pressure to improve the reliability of recovery.

The large sectional area of suspending lines results in major drag and large weight. The sectional area should be as little as possible under the premise of safety. The relationship between torsion angle  $\theta$  and dynamic pressure with different torsional rigidity is plotted in Figure 9. The torsion angle of the calculating example is within the acceptable range. In the case of one-tenth sectional area of suspending lines, the torsion angle is too large. Therefore, the design parameters of line OA have significant effects on the structural stiffness of large parafoil.

#### 4. Conclusion

According to the structural characteristic of parafoil, this study has established the spanwise and chordwise structure model of parafoil. The effects of design parameters on deformation and safety of large parafoils are analyzed. This may be useful for the preliminary parafoil design in rocket booster recovery. From the results, the following conclusions are drawn:

- (1) Due to the constraint of flexible ropes, after inflation, the parafoil will greatly distort in comparison to its ideal design shape. For the analyzed parafoil with cell

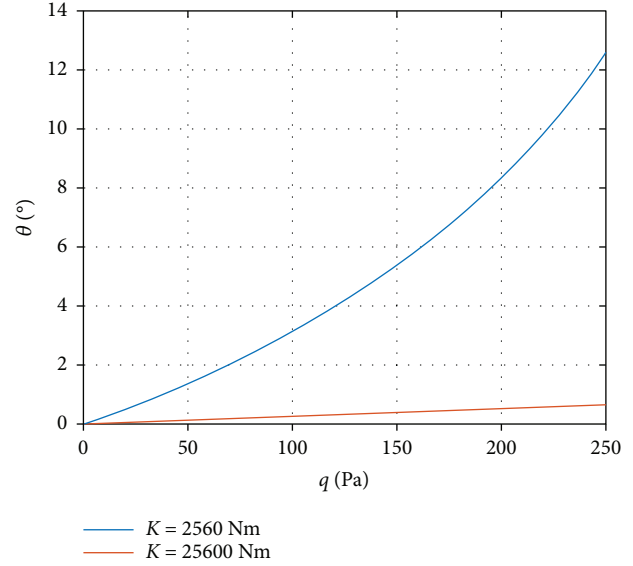


FIGURE 9: Relationship between torsion angle and dynamic pressure.

ratio 0.9, the actual span of the parafoil reduces by 13% compared to the designed span; the maximum thickness of the airfoil Clark-Y18 increases to 26% after the bumps appear.

- (2) The spanwise model is useful for the weakening deformation design and the margin design of the upper and lower piece of the cell. The cell is slender and the canopy surface is smoother. The design value of 2 for the cell ratio is recommended. The aerodynamic load has a bit of effect on the shrinkage and bump ratios.
- (3) The critical disturbance load of wingtip collapse is much lower than the difference of pressure inside and outside. The parafoil with large wing loading has high ability to resist wingtip collapse.
- (4) When the cell width is constant, the critical dynamic pressure reduces  $k$  times with the  $k$  times increasing in parafoil area. The design parameters of line OA have significant effects on the structural stiffness of large parafoils. Increasing the section area of line OA can enlarge the critical dynamic pressure to improve the reliability of booster recovery.

#### Nomenclature

- $P$ : Differential pressure  
 $t$ : Canopy thickness  
 $\sigma$ : Canopy stress  
 $r$ : Widthwise radius of curvature  
 $T_1$ : Tension per unit chord of upper surface  
 $T_2$ : Tension per unit chord of lower surface  
 $T_3$ : Tension per unit chord of the rib  
 $P_1$ : Pressure on upper surface  
 $P_2$ : Stagnation pressure

$h$ : Height of cell  
 $w$ : Width of cell  
 $\varphi$ : Half of the central angle  
 $CL'$ : Lift coefficient defined in the cell coordinate system  
 $\eta_1$ : Shrinkage ratio of cell  
 $\eta_2$ : Bump ratio of cell  
 $l$ : Distance between points A and B  
 $\theta$ : Upward rotation angle  
 $L_1$ : Length of line OA  
 $E$ : Elasticity modulus line OA  
 $A$ : Sectional area of line OA  
 $K_\theta$ : Torsional rigidity of cell  
 $S$ : Reference area of the cell  
 $f$ : Distance between the aerodynamic center and point B.

### Conflicts of Interest

The authors declare that there are no conflicts of interest regarding the publication of this paper.

### References

- [1] C. Matos, R. Mahalingam, G. Ottinger, J. Klapper, R. Funk, and N. Komerath, "Wind tunnel measurements of parafoil geometry and aerodynamics," in *36th AIAA Aerospace Sciences Meeting and Exhibit*, pp. 1–11, Reno, NV, USA, 1998.
- [2] R. H. Geiger and W. K. Wailes, "Advanced recovery systems wind tunnel test report," NASA AD-A238157, Moffett Field, CA, USA, 1990.
- [3] V. Kalro, S. Aliabadi, W. Garrard, T. Tezduyar, S. Mittal, and K. Stein, "Parallel finite element simulation of large ram-air parachutes," *International Journal for Numerical Methods in Fluids*, vol. 24, no. 12, pp. 1353–1369, 1997.
- [4] A. Eslambolchi and H. Johari, "Simulation of flowfield around a ram-air personnel parachute canopy," *Journal of Aircraft*, vol. 50, no. 5, pp. 1628–1636, 2013.
- [5] C. Ibos, C. Lacroix, A. Goy, and P. Bordenave, "Fluid-structure simulation of a 3D ram air parachute with SINPA software," in *15th Aerodynamic Decelerator Systems Technology Conference*, pp. 1628–1636, Toulouse, France, 1999, AIAA-99-1713.
- [6] V. Kalro and T. Tezduyar, "A parallel 3D computational method for fluid-structure interactions in parachute systems," *Computer Methods in Applied Mechanics and Engineering*, vol. 190, no. 3-4, pp. 321–332, 2000.
- [7] N. A. Fogell, S. Sherwin, C. J. Cotter, L. Iannucci, R. Palacios, and D. J. Pope, "Fluid-structure interaction simulation of the inflated shape of ram-air parachutes," in *AIAA Aerodynamic Decelerator Systems (ADS) Conference*, pp. 1–15, Daytona Beach, FL, USA, 2013.
- [8] H. Altmann, "Numerical simulation of parafoil aerodynamics and dynamic behavior," in *20th AIAA Aerodynamic Decelerator Systems Technology Conference and Seminar*, pp. 1–15, Seattle, WA, USA, 2009.
- [9] H. Altmann, "Fluid-structure interaction analysis of ram-air parafoil wings," in *23rd AIAA Aerodynamic Decelerator Systems Technology Conference*, pp. 1–10, Daytona Beach, FL, USA, 2015.
- [10] R. Peralta and H. Johari, "Geometry of a ram-air parachute canopy in steady flight from numerical simulations," in *23rd AIAA Aerodynamic Decelerator Systems Technology Conference*, pp. 1–13, Daytona Beach, FL, USA, 2015.
- [11] Mosseev, "Software tools for the paraglider computer-aided design guide," in *16th AIAA Aerodynamic Decelerator Systems Technology Conference and Seminar*, pp. 52–61, Boston, MA, USA, 2001.
- [12] W. Flügge, *Stresses in Shells*, Springer, Berlin, Heidelberg, 1973.
- [13] L. F. Wang and W. L. He, "Parafoil aerodynamic deformation simulation based on cable-membrane finite element model," *Journal of Beijing University of Aeronautics and Astronautics*, vol. 43, pp. 47–52, 2017.
- [14] Y. C. Gal-Rom and D. E. Raveh, "Simplified aerostructural static model for inflated wings," *AIAA Journal*, vol. 49, no. 6, pp. 1180–1190, 2011.

## Research Article

# Application of a Cohesive Zone Model for Simulating Fatigue Crack Growth from Moderate to High $\Delta K$ Levels of Inconel 718

Huan Li <sup>1,2</sup>, Jinshan Li,<sup>2</sup> and Huang Yuan<sup>3</sup>

<sup>1</sup>School of Mechanics, Civil Engineering and Architecture, Northwestern Polytechnical University, Xi'an, China

<sup>2</sup>State Key Laboratory of Solidification Processing, Northwestern Polytechnical University, Xi'an, China

<sup>3</sup>School of Aerospace Engineering, Tsinghua University, Beijing, China

Correspondence should be addressed to Huan Li; [lihuan@nwpu.edu.cn](mailto:lihuan@nwpu.edu.cn)

Received 8 September 2017; Accepted 6 December 2017; Published 1 February 2018

Academic Editor: Roberto G. Citarella

Copyright © 2018 Huan Li et al. This is an open access article distributed under the Creative Commons Attribution License, which permits unrestricted use, distribution, and reproduction in any medium, provided the original work is properly cited.

A cyclic cohesive zone model is applied to characterize the fatigue crack growth behavior of a IN718 superalloy which is frequently used in aerospace components. In order to improve the limitation of fracture mechanics-based models, besides the predictions of the moderate fatigue crack growth rates at the Paris' regime and the high fatigue crack growth rates at the high stress intensity factor  $\Delta K$  levels, the present work is also aimed at simulating the material damage uniformly and examining the influence of the cohesive model parameters on fatigue crack growth systematically. The gradual loss of the stress-bearing ability of the material is considered through the degradation of a novel cohesive envelope. The experimental data of cracked specimens are used to validate the simulation result. Based on the reasonable estimation for the model parameters, the fatigue crack growth from moderate to high  $\Delta K$  levels can be reproduced under the small-scale yielding condition, which is in fair agreement with the experimental results.

## 1. Introduction

Most of the service failures of aerospace components such as landing gears, turbine blades, fastener joints, and so on are caused by fatigue associated with cyclic loading. The fatigue damage of structural metals normally is associated with the initiation of macrocracks (the nucleation and growth of microcracks), such that a few dominated macrocracks grow until the final unstable fracture happens. By taking into account material degradation instead of one single major crack, continuum damage mechanics provides a sophisticated framework for the fatigue crack initiation analysis of metallic materials [1], while the fracture mechanics-based models are dominated approaches in simulating fatigue crack growth [2].

One of the extensively used models for predicting fatigue crack growth is the Paris' law [3] which relates the range of the stress intensity factor  $\Delta K$  and the crack growth rate  $da/dN$  through a power law in double logarithmic coordinates. Generally, the relationship between  $da/dN$  and  $\Delta K$  for most of metallic materials can be divided into three stages [4], as

illustrated in Figure 1. Regime I corresponds to the formation of a fatigue crack at the low  $\Delta K$ , where crack growth cannot be observed if  $\Delta K$  is less than the threshold  $\Delta K_{th}$ . Regime II usually maintains the Paris' law, which exhibits the moderate fatigue crack growth rate (i.e.,  $10^{-6}$  mm/cycle  $< da/dN < 10^{-3}$  mm/cycle). The high crack growth rate (i.e.,  $da/dN > 10^{-3}$  mm/cycle) achieves at Regime III in which  $\Delta K$  asymptotically approaches the fracture toughness  $\Delta K_c$ . Fatigue life predictions in engineering design have much success with the modifications of the Paris' law to determine crack growth rates [5, 6].

Since elastic or the small-scale yielding (SSY) condition at crack-tip is assumed in the  $K$ -based models, many attractive models have also been proposed to simulate fatigue crack growth with considerable plastic deformations [6–10]. One representative model proposed by Dowling and Begley [7] is constructed by replacing  $\Delta K$  with  $\Delta J$ -integral to extend the Paris' law into the large-scale yielding (LSY) conditions. However, some researchers [11, 12] have pointed out that  $J$ -integral is invalid upon unloading. Although other researchers [10] found that  $\Delta J$ -integral still

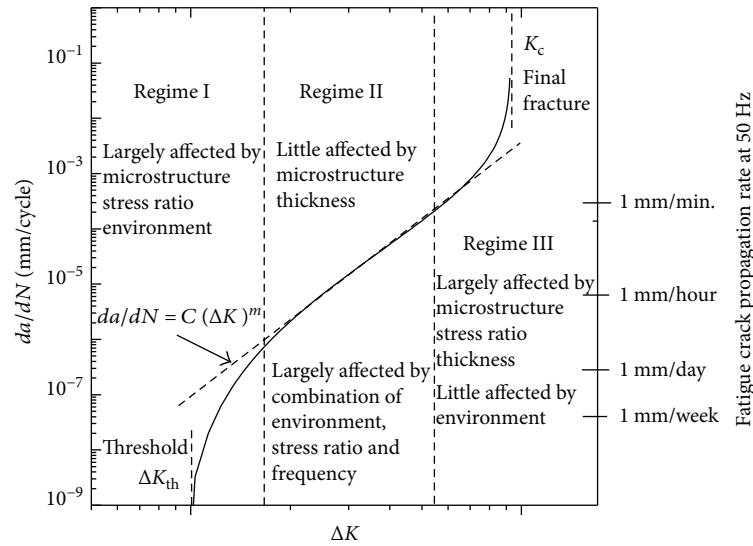


FIGURE 1: The typical fatigue crack growth rate with regard to the stress intensity factor curve for metallic materials, which is distinguished by three regimes. The corresponding influence factors and the crack propagation velocity at 50 Hz under different levels of the fatigue crack growth rate are also illustrated [4].

maintains its path independence under cyclic loadings, nevertheless, it is a considerable issue how to use  $\Delta J$ -integral correctly in fatigue crack growth simulations.

The cohesive zone model (CZM) is another reliable approach which can describe the gradual degradation of stress-carrying ability at a propagating crack-tip within the framework of the nonlinear fracture mechanics. CZMs were firstly proposed by Dugdale [13] and Barenblatt [14] to consider the presence of process zone at crack-tip, where the local degradation during crack growth is determined by a given constitutive law (cohesive law) to relate the traction with the magnitude of material separation. Except the applications in brittle [15] and composite materials [16], cohesive models have been widely used in simulating the ductile fracture of metallic materials. Tvergaard and Hutchinson [17] introduced a trapeziform cohesive law to investigate crack growth resistance during the fracture process of an elastic-plastic solid. Chen et al. [18] simulated the ductile crack growth of the thick CT specimens made of the pressure vessel steel using a polynomial cohesive law. Uthaisangsuk et al. [19] applied a CZM between martensitic islands and ferritic grains to consider interface debonding in the dual-phase microstructure of DP600 steel. Li et al. [20] studied the ductile fracture of a notched Ti-6Al-4V specimen using a CZM. Several authors [21] summarized classifications and applications of the CZM, which demonstrate the importance of cohesive models in simulating ductile fracture.

For fatigue crack calculations, the material degradation under cyclic loading must be considered; namely, the cyclic cohesive zone model (CCZM) should be applied to simulate fatigue crack growth. So far, there are many existing CCZMs that are able to describe the linear Paris' region (Regime II) behavior. The first CCZM disinterring the Paris-like behavior of fatigue crack growth for metallic materials was proposed by Nguyen et al. [22]. They simulated fatigue crack growth of a central cracked aluminum specimen and demonstrated

that the CCZM is capable of reproducing the Paris' law. The unloading-reloading hysteresis was applied to account for dissipative mechanisms, which prevents the "shakedown" effect efficiently in the crack growth process. However, they did not mention the predictive ability of the model in Regime III. Maiti and Geubelle [23] introduced a bilinear cohesive law with an irreversible unloading-loading path to assess capacity of the model for predicting fatigue crack growth in polymers. Although they concluded that the developed model can be used in both Regime II and Regime III for an epoxy, they did not show the applications of the proposed model in simulating ductile materials. Roe and Siegmund [12] considered the effects of the interface fatigue crack growth under different loading modes using an irreversible CZM, and while most of the simulation results were performed under the linear Paris' region, high rates associated with Regime III were not demonstrated. Ural et al. [24] used a damage-based cohesive model to predict the fatigue crack growth behavior in Regime II of an aluminum alloy. However, the application of this model has not been identified in Regime III also. Li and Yuan [25] used a normal stress-dominated cohesive model to simulate fatigue crack growth of cracked and notched specimen and reproduced the linear Paris-like behavior at different loading ratios; nonetheless, the predictive ability in Regime III has not been considered in the CZM. Jimenez and Duddu [26] proposed a strain energy release rate-dependent CZM to model high cycle fatigue delamination of the composite materials under both mode I and mixed mode loadings, and they pointed out that the CZM is suitable for the constant amplitude loading in Regime II and also expected to extended the model to describe all three regimes in fatigue crack simulations. CCZMs can also be applied in analyzing the elastoplastic fatigue cracks by introducing some stress triaxiality-dependent parameters [27, 28]; that is, Jha and Banerjee [28] proposed a triaxiality-dependent cohesive model to

simulate the fatigue failure of ductile metals and proved that the CZM is suitable for the geometries with different stress states. Similarly, these models [27, 28] do not mention their applications for fatigue crack growth at the high  $\Delta K$  levels in Regime III.

Although the Paris-like behavior which corresponds to the moderate  $\Delta K$  levels in Regime II can be predicted by using the aforementioned CCZMs [11, 22-27], this is not the advantage of CCZMs, since the Paris regime associated with SSY has already been described successfully according to the  $K$ -based models. In order to resolve the more challenging task that to simulate the high fatigue crack growth rates in Regime III of the metallic materials, a CCZM was proposed in our previous work [29] in which two damage variables were defined to represent monotonic damage and fatigue damage, respectively. In fact, it is not easy to distinguish these two different damage mechanisms in fatigue crack growth before the final rupture occurs; thus, it is better to describe the material damage evolution uniformly. Meanwhile, it is anticipated that CCZMs have the potential to predict high fatigue crack growth rates in Regime III under the LSY conditions. For the purpose of easing the difficulty level for cohesive modeling of fatigue crack growth at LSY, the predictive ability of CCZMs in simulating high fatigue crack growth rates at SSY should be verified systematically.

Therefore, the objective of this work is to examine a CCZM for predicting high fatigue crack growth rates corresponding to Regime III under the SSY conditions. Meanwhile, the present study attempts to describe the material damage evolution uniformly and identify the effects of the cohesive model parameters on fatigue crack growth under both moderate and high  $\Delta K$  levels. The contents of this paper include the following aspects: in Section 2, the detailed formulations of the CCZM are introduced. In Section 3, the identification of the model parameters is performed firstly, then the numerical results are presented according to the compact-tension (CT) specimens and the single-edge notched (SEN) specimens made of the IN718 superalloy and validated against the experimental data from literatures. Finally, the major conclusions are summarized in Section 4.

## 2. Cohesive Zone Model

The cohesive model has the ability to consider the ductile rupture of the metallic materials under various loading conditions. For fatigue crack growth simulations, the CCZM has to be able to describe accumulative damage associated with cyclic loading. Assume that the degradation of the original cohesive envelope occurs with damage accumulation, and the constitutive law under fatigue loading is defined as

$$T_n = \sigma_{\max} \begin{cases} \frac{\delta_n}{\delta_0} \exp\left(1 - \frac{\delta_n}{\delta_0}\right), & \delta_n \leq \delta_0, \\ 1, \delta_c = \delta_0 + D(\delta_u - \delta_0), & \delta_0 < \delta_n \leq \delta_c, \\ \frac{\delta_u - \delta_n}{\delta_u - \delta_c}, & \delta_c < \delta_n \leq \delta_u, \end{cases} \quad (1)$$

where the normal traction  $T_n$  is assumed to be a piecewise function depending upon the normal separation  $\delta_n$ .  $\delta_0$  is the characteristic length of the cohesive law, which is denoted as the cohesive length.  $\delta_u$  denotes the maximum normal separation above which the normal traction vanishes. Following the concept from the continuum damage models, the damage variable  $D = \int_t \dot{D} dt$  stands for the material degradation and represents failure if  $D$  approaches 1.  $\sigma_{\max} = \sigma_{\max,0}(1 - D)$  is the cohesive strength used to identify the peak value of the normal traction and  $\sigma_{\max,0}$  is the initial cohesive strength. The original cohesive law under monotonic loading can be obtained by substituting  $D = 0$  into (1). The parameter  $\delta_c$  corresponds to the material separation relating to the damage variable  $D$  and  $\delta_0 \leq \delta_c \leq \delta_u$ . For both constant and variable amplitude loadings, the damage evolution equation suggested by Roe and Siegmund [12] can be applied to reflect the accumulative damage for the metallic materials, which reads

$$\dot{D} = \frac{\langle \dot{\delta}_n \rangle}{d_\Sigma} \left\langle \frac{T_n}{\sigma_{\max,0}(1 - D)} - \frac{\sigma_f}{\sigma_{\max,0}} \right\rangle H(\bar{\delta} - \delta_0), \quad \dot{D} \geq 0, \quad (2)$$

where  $d_\Sigma$  is the accumulated cohesive length used to scale the increment of the normal separation  $\dot{\delta}_n$  and  $\bar{\delta} = \int_t |\dot{\delta}_n| dt$ .  $\sigma_f$  is the cohesive endurance limit. The Macaulay brackets  $\langle \rangle$  are used to signify nonnegative value of damage evolution, and the Heaviside function  $H$  states that damage initiates at  $\bar{\delta} > \delta_0$ .

The novel cohesive envelope determined by (1) will degrade and change its shape correspondingly associated with the damage accumulation, and this characteristic is the major difference between the current model and other CCZMs [11, 12, 20, 22-28]. For example, in [25], the combination use of (2) and the cohesive envelope of the exponential form are performed to simulate fatigue crack growth; however, this combination results in the contradictory damage evolution at  $\delta_n > \delta_0$  if a slightly larger value of  $\sigma_f/\sigma_{\max,0}$  is provided, and this problem can be solved by using (1). As mentioned above, the similar CCZM has been proposed to investigate the mixed mode fatigue crack growth in our previous simulations [29], the difference between these two models is that the current one does not introduce the monotonic damage, the material degradation under cyclic loadings is described uniformly by (2), and the monotonic damage is determined by the cohesive envelope implicitly. Actually, the combination of (1) and (2) has the capacity to simulate fatigue crack growth at the high  $\Delta K$  levels, the applications need not be distinguished between monotonic damage and fatigue damage as introduced in [29], the key point in such simulations is the form of (1), and more details will be performed in Section 3.

For the numerical implementation of the model under each unloading-reloading cycle, assume that the residual separation exists after a complete unloading cycle as plastic

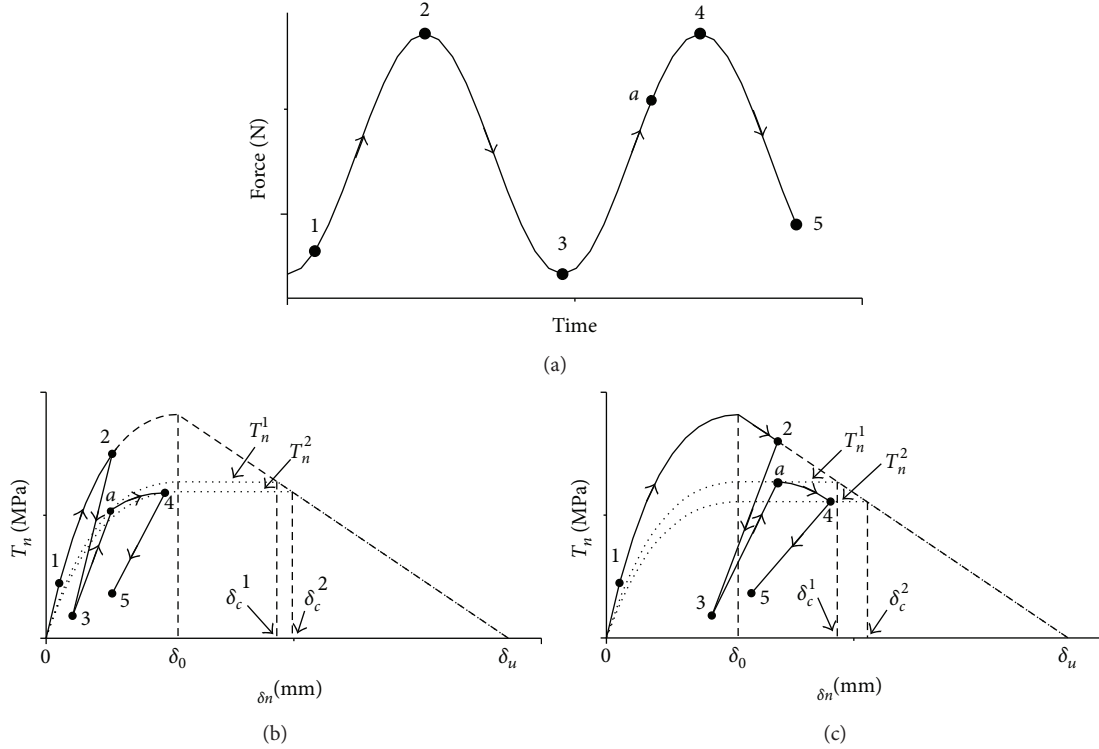


FIGURE 2: Illustration of the loading-unloading-reloading path together with (a) the cyclic loading spectrum at (b)  $\delta_n < \delta_0$  (first half cycle) and (c)  $\delta_n > \delta_0$  (first half cycle): loading with opening of the cohesive surface (1  $\rightarrow$  2); unloading (2  $\rightarrow$  3); reloading with the damage accumulation (3  $\rightarrow$  4); and subsequent partial unloading (4  $\rightarrow$  5). The dot lines represent the degraded cohesive envelopes.

deformations, and the corresponding unloading-reloading path can be denoted by

$$T_n = T_{n,t} + k_n(\delta_n - \delta_{n,t}), \quad \delta_n, \delta_{n,t} \geq 0, \quad (3)$$

with

$$k_n = \frac{\sigma_{\max} \exp(1)}{\delta_0}, \quad (4)$$

where  $T_n$  is the traction at time  $t + \Delta t$  related to the separation  $\delta_n$  according to the cohesive stiffness  $k_n$ .  $T_{n,t}$  and  $\delta_{n,t}$  are the traction and the separation at time  $t$ , respectively.

As shown in Figure 2(a), assume that the rising segment (1  $\rightarrow$  2) of the loading sequence results in the separation of a material point at the cohesive zone. In order to explain the operating mechanism of the model under cyclic loading in detail, two different cases are considered, namely,  $\delta_n \leq \delta_0$  (Figure 2(b)) and  $\delta_n > \delta_0$  (Figure 2(c)). Upon unloading, the path (2  $\rightarrow$  3) follows (3) without damage evolution. The contact of two cohesive surfaces is constrained by introducing a penalized equation as

$$T_n = A\sigma_{\max,0} \exp(1) \frac{\delta_n}{\delta_0}, \quad \delta_n < 0, \quad (5)$$

where  $A$  is the penalty stiffness. Here, we should mention that this contact algorithm is applied to simulate crack closure explicitly. The crack closure effects are related to the plastic

deformation of the bulk material around the crack-tip implicitly under cyclic loading.

The reloading path (3  $\rightarrow$   $a$ ) specified by (3) deviates from the previous unloading path due to damage evolution. At the subsequent loading segment (3  $\rightarrow$  4), the value of  $T_n$  corresponding to reloading may reach the degraded cohesive envelope  $T_n^1$  at  $a$ . Upon further reloading, the value of  $T_n$  moves along the degraded envelope  $T_n^1$  at time  $t$ ; however, the continued damage accumulation through (2) makes it move along the subsequent degraded cohesive envelope  $T_n^2$  at time  $t + \Delta t$ . The dot lines in Figures 2(b) and 2(c) are two degraded cohesive envelopes corresponding to  $\delta_c^1$  and  $\delta_c^2$ , respectively. In both cases, if the loading level makes the reloading path move along the descending part of the degraded cohesive envelop, there is no damage accumulation that will occur and the material degradation is described by (1) implicitly.

The above CCZM has been implemented based on the user interface UMAT of the commercial code ABAQUS via the cohesive element [30]. Since the numerical simulations are performed according to the ABAQUS/Standard solver, both the updated cohesive traction and the material Jacobian matrix should be provided for constructing the internal nodal force vector and the cohesive stiffness matrix in UMAT. The standard Newton method is applied to solve the global nonlinear equations, and the default values for the solution control parameters are adopted. The global convergence rule is checked at the end of each time

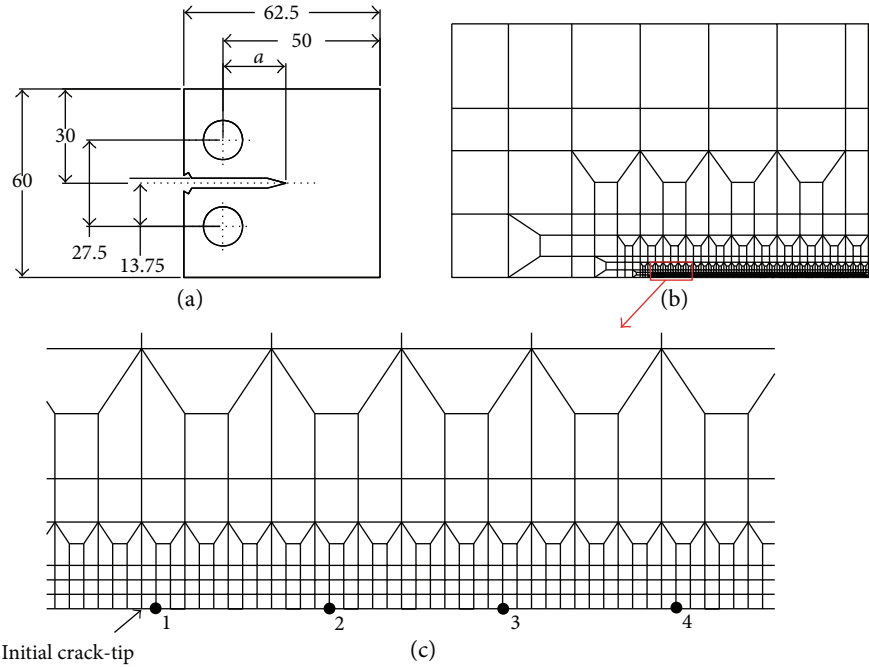


FIGURE 3: (a) Sketch of a CT specimen (initial crack length  $a = 25$  mm, width  $W = 50$  mm, and thickness  $B = 12.5$  mm) and (b) the FE mesh (a half of the specimen is modeled), and (c) points 1, 2, 3, and 4 correspond to the four integration points located along the crack growth path (the distance between two adjacent points is 1.2 mm), and the arrow indicates the initial crack-tip of the CT specimen.

increment, such that the tolerance limit on the residual force can be fulfilled.

### 3. Model Validation

In the present study, the influence of model parameters on fatigue crack growth will be verified systematically; meanwhile, the predictive ability of the model for the high fatigue crack rates in Regime III will be validated experimentally. The material under investigation is a nickel-based superalloy IN718 which is widely used in aeroengine components due to its high yield stress, excellent fatigue resistance, and so on in severe conditions [31]. In modeling a CT specimen with the initial crack, the length is  $a = 25$  mm and the thickness is  $B = 12.5$  mm. The material properties are as follows: Young's modulus  $E = 200$  GPa, Poisson's ratio  $\nu = 0.3$ , the initial yield stress  $\sigma_y = 1196$  MPa, and the plane strain fracture toughness  $K_{Ic} = 125$  MPa m<sup>1/2</sup>. The  $J_2$  plasticity is applied to describe the plastic behavior of the alloy, and the relationship between true stress  $\sigma$  and true plastic strain  $\epsilon_p$  is described by the Holomon's equation as

$$\sigma = K(\epsilon_p)^n, \quad (6)$$

where the bulk modulus  $K = 1531$  MPa and the strain hardening exponent  $n = 0.015$ . We note from the perspective of cohesive modeling for fatigue crack that the isotropic hardening is often assumed to simulate the material response approximately without knowing the exact cyclic deformation behavior of the bulk material [11, 28, 32]. However, the more accurate cyclic plasticity model should be determined experimentally as mentioned in [33]. Due to the symmetry, only

the upper half of the specimen is modeled under the plane strain condition, as shown in Figure 3. The whole finite-element model consists of 1725 elements and 1872 nodes. The cohesive zone is predefined along the crack growth path using 240 COH2D4 elements which are uniformly distributed along the ligament of the specimen with the element length of 0.1 mm. The CPE4 elements are used for the rest of the regions.

**3.1. Identification of Model Parameters.** Based on previous descriptions, the model parameters can be divided into two types. The monotonic model parameters include cohesive strength  $\sigma_{\max,0}$ , cohesive length  $\delta_0$ , and cohesive energy  $\Gamma_0$ . The cyclic model parameters are the accumulative length  $d_\Sigma$  and the cohesive endurance limit  $\sigma_f$ . Omitting shear stress in the cohesive zone, only the normal traction is active under the mode I crack growth condition. The cohesive energy  $\Gamma_0$  is determined by integration of the monotonic cohesive envelope as follows:

$$\Gamma_0 = \int_0^{\delta_u} T_n d\delta_n, \quad (7)$$

where the form of  $T_n$  is represented by (1) with  $D = 0$ . The monotonic cohesive envelope can be constructed through the initial cohesive strength  $\sigma_{\max,0}$ , the cohesive length  $\delta_0$ , and the cohesive energy  $\Gamma_0$ . Under the SSY conditions, the cohesive energy is related to the plain strain fracture toughness  $K_{Ic}$  based on the Irwin's relation as follows:

$$\Gamma_0 = \frac{(1 - \nu^2)K_{Ic}^2}{E}. \quad (8)$$

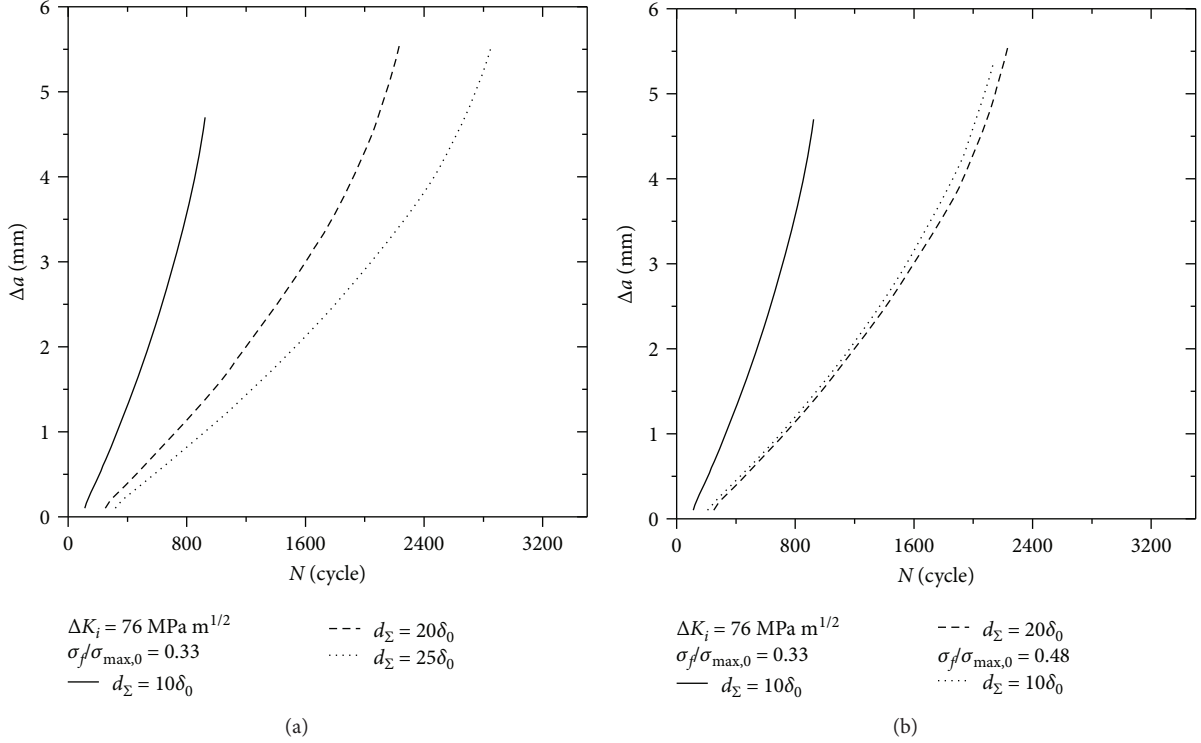


FIGURE 4: The effects of (a) the accumulative length  $d_\Sigma$  and (b)  $\sigma_f/\sigma_{\max,0}$  on the crack growth curve. The constant loading amplitude is carried out with  $F_{\max} = 24 \text{ kN}$  at  $R = 0.1$ , where the corresponding initial stress intensity factor range  $\Delta K_i = 76 \text{ MPa m}^{1/2}$  for the CT specimen.

According to (8), the cohesive energy is  $\Gamma_0 = 7.1 \times 10^4 \text{ J/m}^2$  in the present analysis. The cohesive strength  $\sigma_{\max,0} = 3900 \text{ MPa}$  is used, which is nearly three times above the initial yield stress of IN718 according to the suggestion in [34], where the corresponding cohesive length  $\sigma_0 = 0.003 \text{ m}$ . Actually, the relationship between the initial cohesive strength and cohesive length can be attributed to the effect of the initial cohesive stiffness  $k_n$ . The choice related to  $k_n$  should guarantee that the cohesive zone does not influence the overall compliance before damage initiation and normally a higher value of  $k_n$  is used. Since the cohesive energy is the work needed to create a unit area of two mating fracture surfaces, the resulting  $\delta_u = 0.017 \text{ mm}$  is obtained according to (1) with  $D = 0$ .

Identification of the influence of the model parameters is performed using the CT specimen under constant loading amplitudes at the loading ratio  $R = 0.1$ , where  $R = F_{\min}/F_{\max}$  with  $F_{\max}$  and  $F_{\min}$  are the maximum and minimum of the uniaxial applied force  $F$ , respectively. The nominal stress intensity factor is applied to describe the stress field at crack-tip. The range of the stress intensity factor  $\Delta K$  for the CT specimens can be calculated through [35]:

$$\Delta K = \frac{\Delta F(2 + \zeta)}{B\sqrt{W}(1 - \zeta)^{3/2}} \cdot \left[ 0.886 + 4.64\zeta - 13.32\zeta^2 + 14.72\zeta^3 - 5.6\zeta^4 \right], \quad (9)$$

where  $\zeta = a/W$ . This formulation is accurate within 0.5% error over the range  $0.2 \leq \zeta \leq 1$ .

The effect of the accumulative length  $d_\Sigma$  to the crack growth length curve is indicated in Figure 4(a), where the initial stress intensity factor  $\Delta K_i = 76 \text{ MPa m}^{1/2}$ . At a given crack growth length  $\Delta a$ , the lower value of  $d_\Sigma$  corresponds to the higher crack growth rate for the same value of  $\sigma_f/\sigma_{\max,0}$ . In comparison with the number of loading cycles to the final failure between  $d_\Sigma = 20\delta_0$  and  $d_\Sigma = 25\delta_0$ , the critical crack growth length of approx. 5.5 mm is achieved under both  $d_\Sigma = 20\delta_0$  and  $d_\Sigma = 25\delta_0$  at failure. Theoretically, the critical crack length should be reached at  $d_\Sigma = 10\delta_0$  also; however, the FE calculation is aborted since the high damage evolution rate associated with  $d_\Sigma = 10\delta_0$  is so fast that the mesh resolution of 0.1 mm at crack-tip cannot capture the crack growth rate before the final failure. The effect of  $\sigma_f/\sigma_{\max,0}$  on the crack growth curves is shown in Figure 4(b) by comparing two different values of  $\sigma_f/\sigma_{\max,0}$  at  $d_\Sigma = 10\delta_0$ , where the higher crack growth rate is accompanied by the lower value of  $\sigma_f/\sigma_{\max,0}$  at a given crack length. Based on Figure 4, we can conclude that the critical crack length is only determined by the monotonic model parameters together with the  $\Delta K$  level.

The effect of  $d_\Sigma$  on the  $da/dN$  versus  $\Delta K$  curve is shown in Figure 5(a), where the  $da/dN$  data are determined based on the corresponding  $a - N$  curves (see Figure 4). In order to examine the effects of cyclic model parameters on fatigue crack growth in the Paris' region, the numerical results of the lower loading level  $F_{\max} = 20 \text{ kN}$  associated with  $\Delta K_i = 63 \text{ MPa m}^{1/2}$  is also displayed. The accumulative length  $d_\Sigma$  acts like the intercept coefficient  $C$  which operates in the Paris' law, that is,  $da/dN = C(\Delta K)^m$ . It plays a role

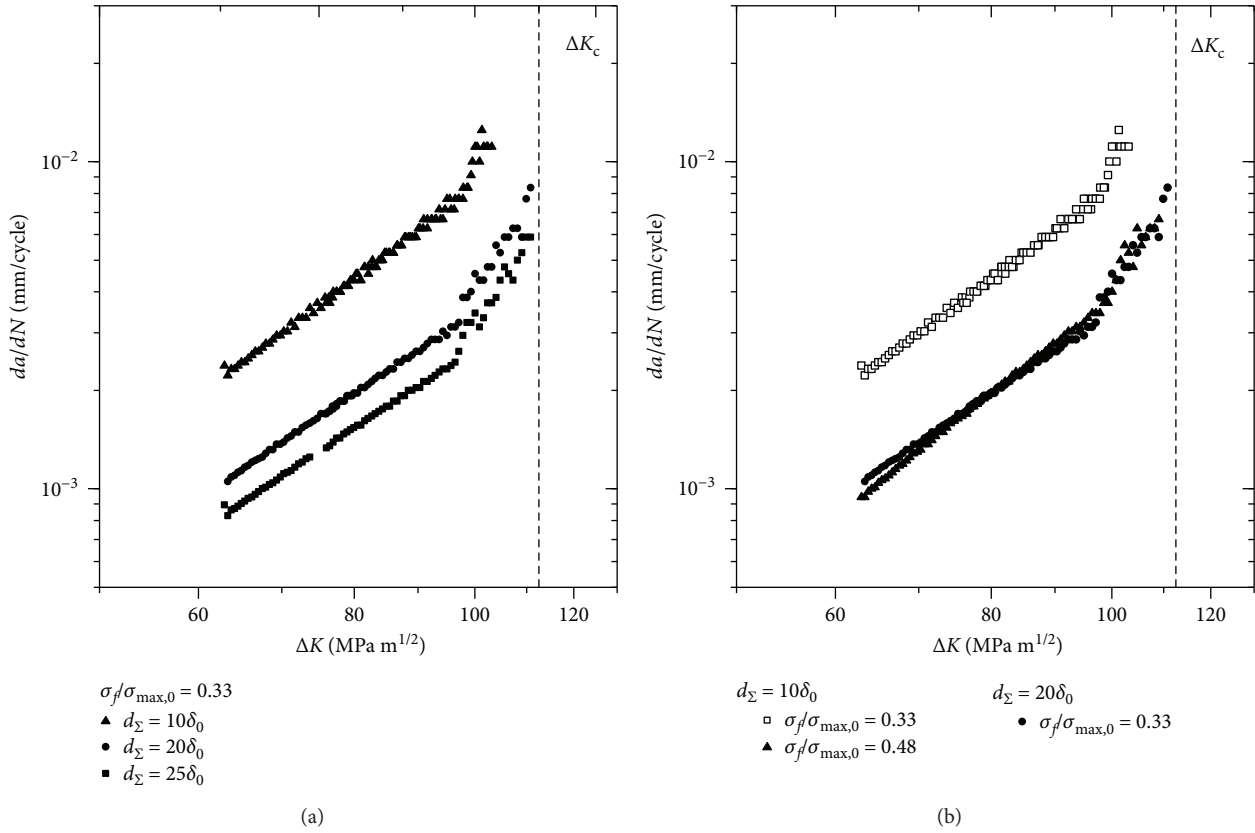


FIGURE 5: The effects of (a) the accumulative length  $d_{\Sigma}$  and (b)  $\sigma_f/\sigma_{max,0}$  on the fatigue crack growth rate. The constant loading amplitude is carried out with  $F_{max} = 20$  kN and 24 kN at  $R = 0.1$ , where the corresponding initial stress intensity factor range  $\Delta K_i = 63$   $\text{MPa m}^{1/2}$  and  $\Delta K_i = 76$   $\text{MPa m}^{1/2}$  for the CT specimen, respectively.

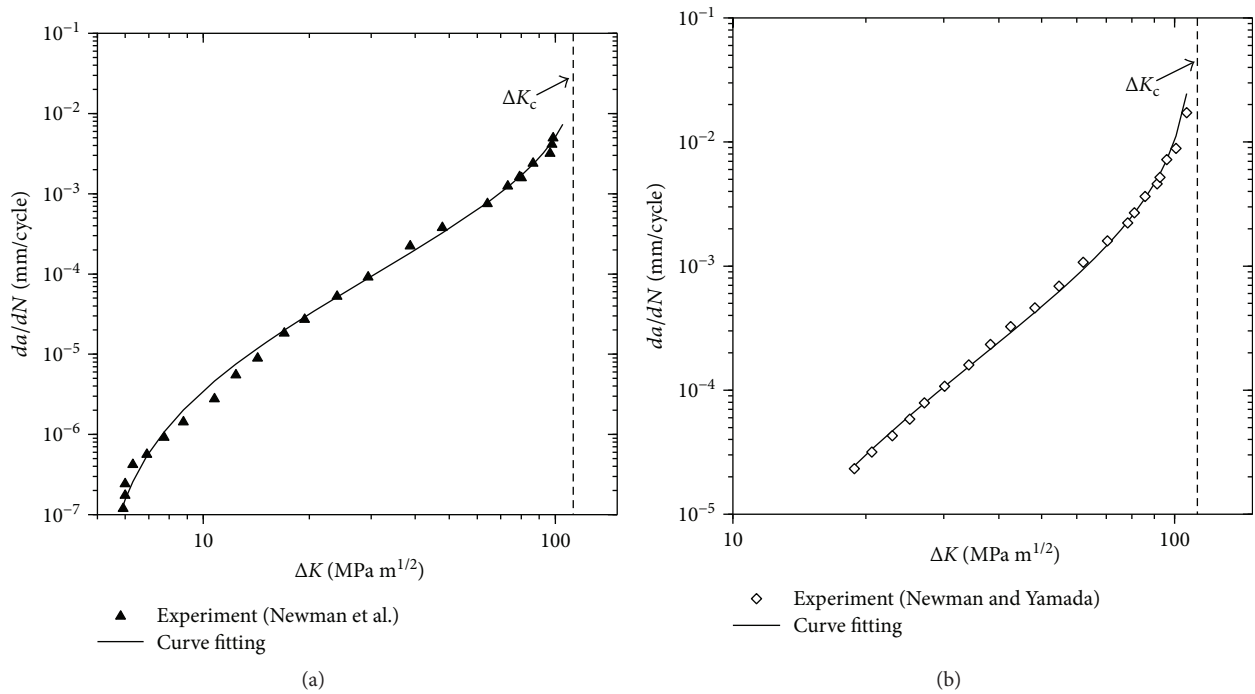


FIGURE 6: Plot of the experimental result and the corresponding fitting curve by using the Erdogan-Ratwani model of the IN718 alloy for (a) the CT specimens and (b) the SEN specimens.

in increasing or decreasing crack growth rate in all portions at a certain value of  $\sigma_f/\sigma_{\max,0}$ . In contrast,  $\sigma_f/\sigma_{\max,0}$  has a tendency to modify the slope of the  $da/dN$  versus  $\Delta K$  curve as the parameter  $m$  of the Paris' law, as shown in Figure 5(b). However, the effects of the cyclic model parameters are also influenced by the monotonic model parameters; namely, the crack growth rate is accelerated inevitably as the  $\Delta K$  level approaches the critical value  $\Delta K_c = (1-R)K_{Ic}$  in Regime III before the final failure. The above results reveal that the high fatigue crack growth rates at high  $\Delta K$  levels can be captured reasonably based on the current model and the uniform damage evolution equation can be applied in such simulations.

**3.2. Comparison with Experiments.** After the parameter identification, the next the predictive ability of the model will be examined using the CT specimen as displayed in Figure 3(a). The experimental data in validations are obtained by digitizing the results reported by Yamada and Newman [36] and Newman et al. [37], as shown in Figure 6, where the fatigue crack growth tests were performed by using the CT specimens and the SEN specimens at  $R = 0.1$ , respectively. The experimental results are fitted according to the Erdogan-Ratwani model [5]. For the CT specimens, the experimental points can be well approximated by the following equation:

$$\frac{da}{dN} = \frac{2.554 \times 10^{-5} (\Delta K - 8)^{1.887}}{\Delta K_c - \Delta K}, \quad (10)$$

where  $da/dN$  is in mm/cycle and  $\Delta K$  is in  $\text{MPa m}^{1/2}$ . For the SEN specimens, all points including the threshold region can be well described by the following equation:

$$\frac{da}{dN} = \frac{1.782 \times 10^{-5} (\Delta K - 5)^{1.917}}{\Delta K_c - \Delta K}. \quad (11)$$

Three constant loading amplitudes, that is,  $F_{\max} = 17 \text{ kN}$ ,  $18.5 \text{ kN}$ , and  $20 \text{ kN}$  at  $R = 0.1$ , are applied to obtain the cyclic cohesive model parameters, where the corresponding initial stress intensity range are  $\Delta K_i = 54 \text{ MPa m}^{1/2}$ ,  $\Delta K_i = 58 \text{ MPa m}^{1/2}$ , and  $\Delta K_i = 63 \text{ MPa m}^{1/2}$ , respectively. The fatigue crack growth simulations are performed to fit the experimental data associated with the moderate growth rates. As depicted in Figure 7, the fitting curve constructed by the aforementioned three  $\Delta K$  levels correlates the experiments very well in the linear Paris' region. The corresponding crack growth versus the applied loading cycle curves are displayed in Figure 8, where the fastest crack growth rate is achieved under the highest  $\Delta K$  level at a given crack length. The determined cyclic model parameters of IN718 are listed in Table 1.

For the fatigue crack growth simulation in Regime III, the constant loading amplitude is applied with  $F_{\max} = 24 \text{ kN}$  at  $R = 0.1$ , which corresponds to the initial stress intensity factor range  $\Delta K_i = 76 \text{ MPa m}^{1/2}$ . In order to capture the local response of each material point along the crack growth path, four material points 1, 2, 3, and 4 located at the crack growth path are used to trace the material responses associated with

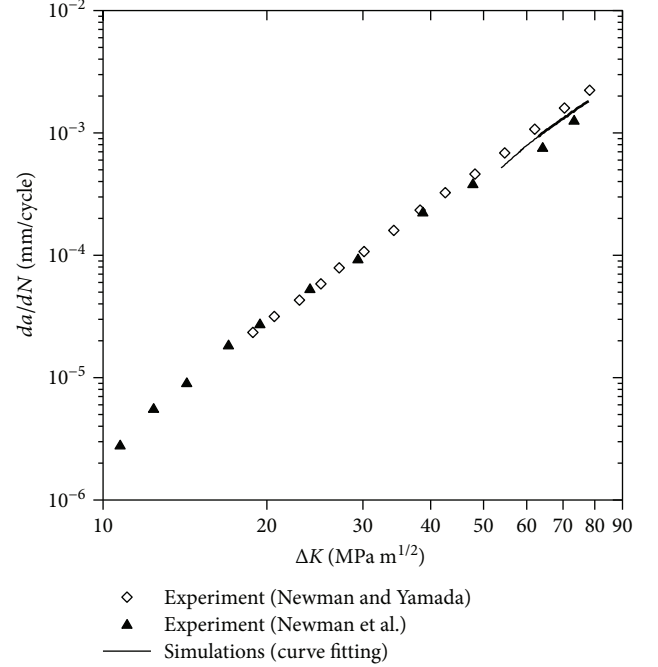


FIGURE 7: Plot of the experimental results and the corresponding fitting curves of the CCZM in the Paris' region.

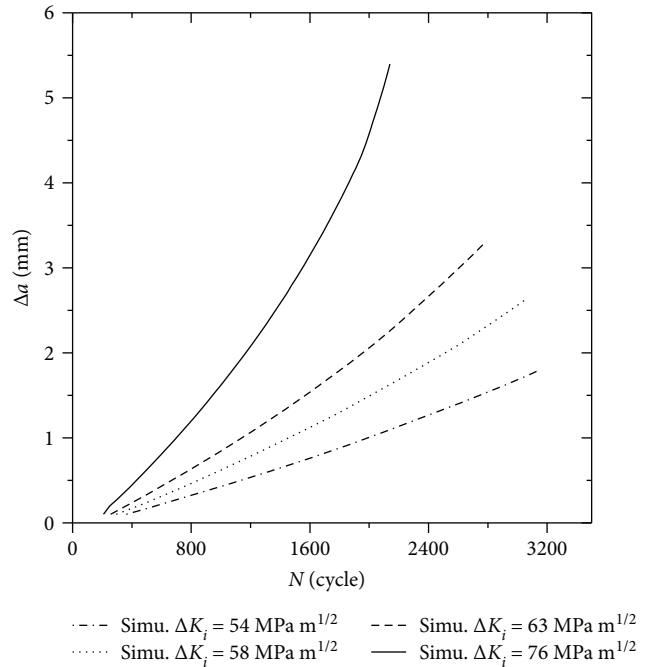


FIGURE 8: The crack growth curves with varying  $\Delta K_i$  under the constant amplitude loading at  $R = 0.1$ .

TABLE 1: Model parameters of IN718 used in simulations.

$\sigma_{\max,0}$ (MPa)	$\delta_0$ (mm)	$\delta_u$ (mm)	$\sigma_f$ (MPa)	$d_{\Sigma}$ (mm)
3900	0.003	0.017	1847	0.03

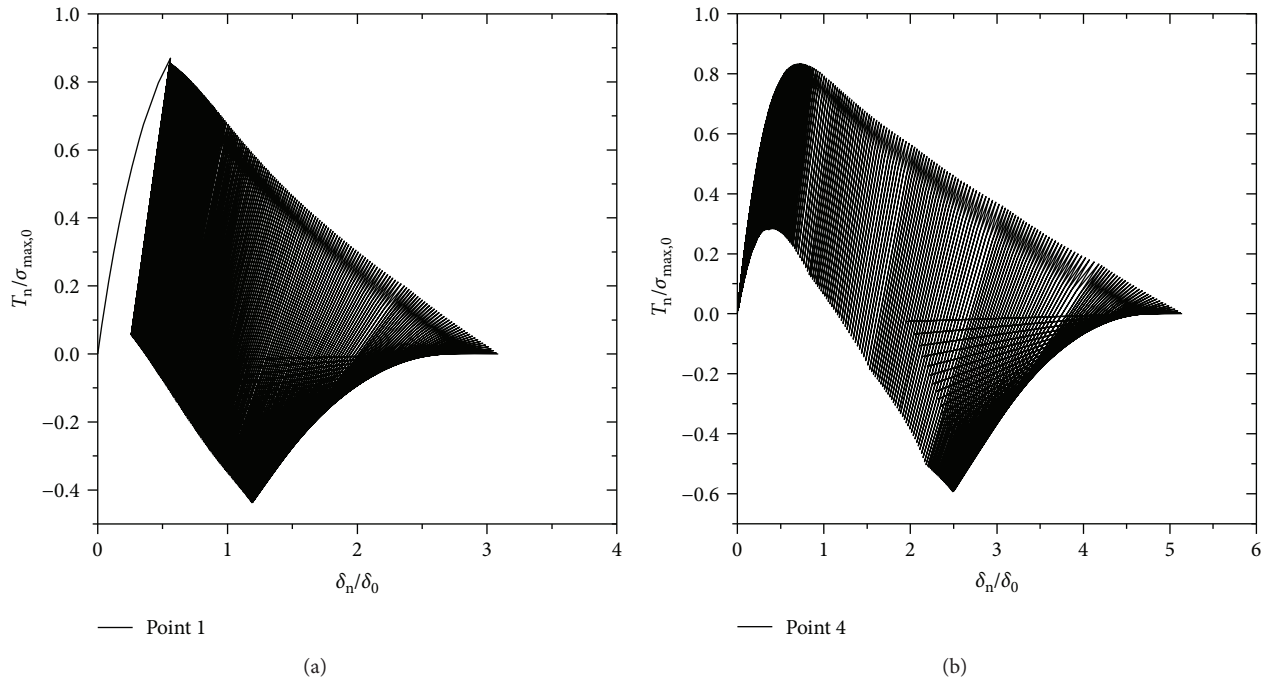


FIGURE 9: The traction versus separation curves are compared between (a) point 1 and (b) point 4, and the constant loading amplitude is carried out with  $F_{max} = 24$  kN at  $R = 0.1$ , which corresponds to the initial stress intensity factor range  $\Delta K_i = 76$  MPa  $m^{1/2}$  for the CT specimen.

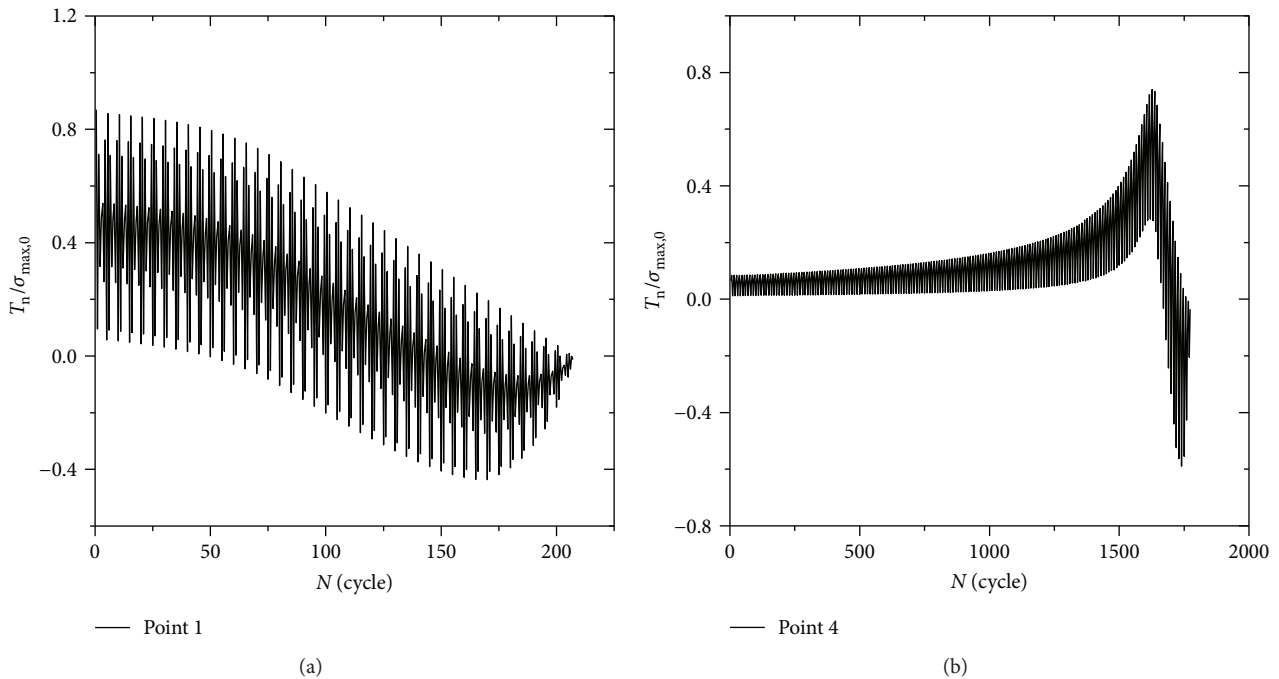


FIGURE 10: The traction against the number of applied cycles is compared between (a) point 1 and (b) point 4, and the constant loading amplitude is carried out with  $F_{max} = 24$  kN at  $R = 0.1$ , which corresponds to the initial stress intensity factor range  $\Delta K_i = 76$  MPa  $m^{1/2}$  for the CT specimen.

the high propagation rates, as illustrated in Figure 3(c). The distance between two adjoining monitor point is 1.2 mm.

The traction-separation responses during crack growth are indicated in Figure 9 for both points 1 and 4, where the material damage is obtained based on (2) for the two material

points. The traction of point 1 approaches 87% of the initial cohesive strength  $\sigma_{max,0}$  at the first loading cycle while the traction of point 4 is still small; namely, the traction of point 4 is only 10% of  $\sigma_{max,0}$  at the first loading cycle, as shown in Figure 10. Except for point 1 loses its stress-carrying ability at

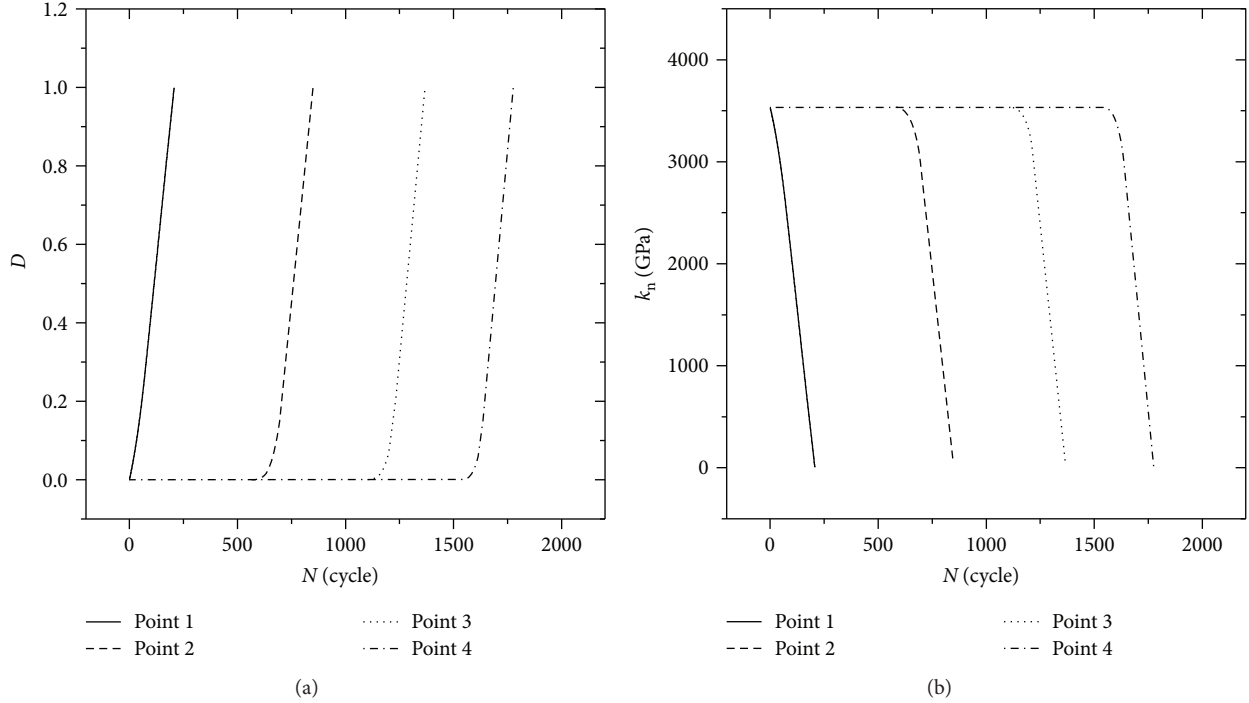


FIGURE 11: (a) The damage evolution and (b) the cohesive stiffness with the number of applied cycles are compared from point 1 to point 4, and the constant loading amplitude is carried out with  $F_{\max} = 24$  kN at  $R = 0.1$ , which corresponds to the initial stress intensity factor range  $\Delta K_i = 76$  MPa m<sup>1/2</sup> for the CT specimen.

the 207th cycle, other points have no damage accumulations at the first 548 loading cycles such that their original cohesive stiffnesses still exist, since there are no damage evolutions for these points (see Figure 11). The damage initiation for point 4 starts after 1500 loading cycles, where the maximal value of the traction increases (up to 80% of  $\sigma_{\max,0}$ ) at first and then decreases with the applied loading cycles until the material point is completely damaged (see Figure 10(b)), and this phenomenon is also true for points 2 and 3.

During the crack growth process, the distributions of the damage zone, the von-Mises stress, and the equivalent plastic strain under both the moderate and the high levels of  $\Delta K$  are compared in Figure 12. The fatigue crack propagates from length  $a = 25.5$  mm to 29.5 mm by measuring the length of the complete damage zone of the two levels of  $\Delta K$ . For two cases, the von-Mises stress ahead of the current crack-tip is greater than the initial yield stress 1196 MPa and the obvious plastic zone is created gradually in the crack wake during crack growth. These results show that the material responses of both the cohesive zone and the surrounding bulk material are simulated reasonably.

Figure 13 summarizes the numerical and experimental crack growth results under constant amplitude loading. The simulation associated with  $F_{\max} = 24$  kN is the predicting result based on the determined model parameters listed in Table 1. The whole  $da/dN$  versus  $\Delta K$  curves are assembled through these four different  $\Delta K_i$  levels. With increment of the crack length,  $da/dN$  becomes very high and approaches instability limited by the  $\Delta K_c$  at failure (see Figure 13). As indicated in Figure 1, fatigue crack growth in Regime II is

largely influenced by the loading ratio and the frequency in the air; therefore, fatigue crack growth with moderate rates is irrelevant to the geometries of specimens. At high propagation rates as  $\Delta K$  approaches to  $\Delta K_c$ , there is a good agreement between the prediction and the experiment of the SEN specimens, while a deviation between the simulation and the experiment of the CT specimens exists. Actually, the difference in experiment data also occurs between the CT and SEN specimens in Regime III due to the occurrence of ductile fracture. The ductile fracture process of metallic materials involves nucleation, growth, and coalescence of microvoids, which is greatly influenced by the stress state and may not be described, for example, by (1) simply, and the local constraint effect accompanied by the specimen geometry also affects the crack growth resistance. Nevertheless, based on the cyclic model parameters determined by the experimental data in Regime II, the numerical result captures the accelerated fatigue crack growth phenomenon of the experimental data in Regime III associated with the high  $\Delta K$  levels.

#### 4. Conclusions

In order to overcome the limitations of fracture mechanics-based models, for example, the Paris' law or the  $\Delta J$ -integral-based model, for predicting elastic-plastic fatigue crack growth rates, the cyclic cohesive model is verified systematically on the fatigue crack growth of the IN718 alloy from moderate to high  $\Delta K$  levels. Since ductile fracture occurs as the  $\Delta K$  level approaches the fracture toughness, the model parameters determined from the experimental

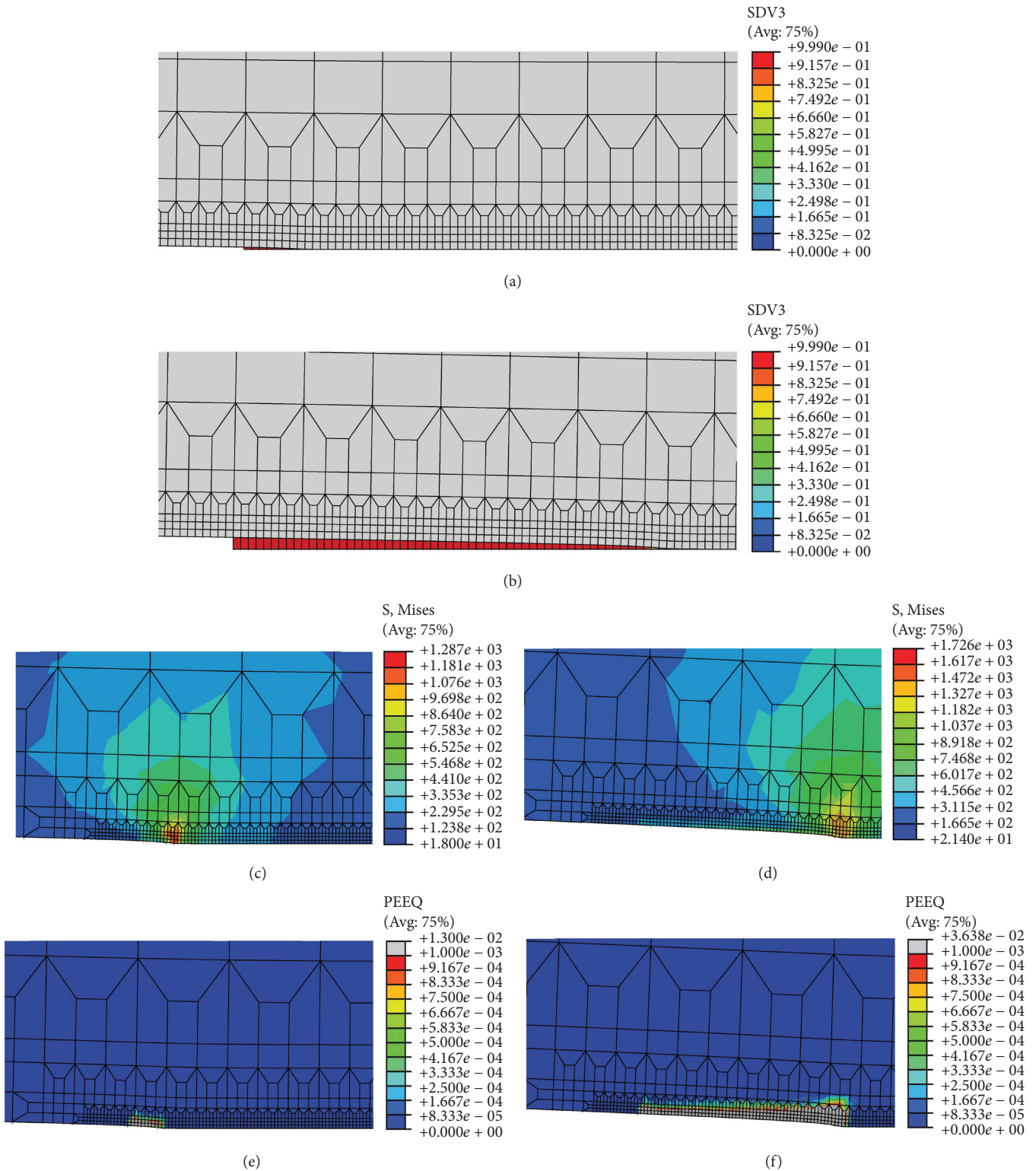


FIGURE 12: Contour plots during crack growth: (a, b) damage evolution; (c, d) von-Mises stress; (e, f) equivalent plastic strain (PEEQ). The corresponding crack length  $a$  is (a, c, e) 25.5 mm with the moderate  $\Delta K = 77 \text{ MPa m}^{1/2}$ ; (b, d, f) 29.5 mm with the high  $\Delta K = 102 \text{ MPa m}^{1/2}$ .

data at the moderate  $\Delta K$  levels cannot predict the fatigue crack growth rates at the high  $\Delta K$  levels for all the specimens exactly, and the local constraint effect should be considered during the damage evolution in Regime III.

The simulations reveal that the novel cohesive envelope combined with one damage evolution equation can also be used to capture the accelerated fatigue crack growth behavior at the high  $\Delta K$  levels, and there is no need to distinguish

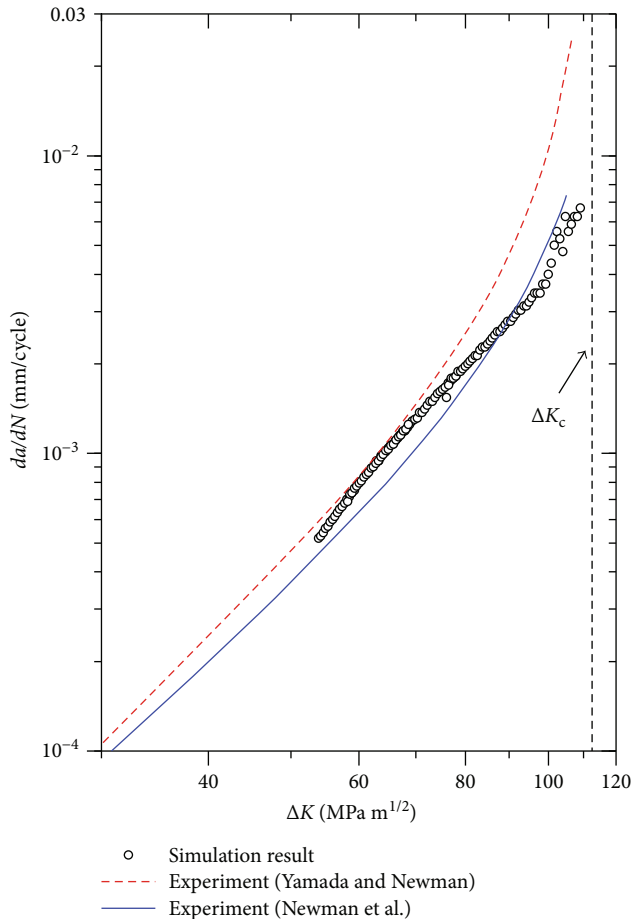


FIGURE 13: Comparison between experiments and the proposed CCZM under the constant force amplitude with  $R = 0.1$ .

between the monotonic damage and the fatigue damage as introduced in [29]. The crack growth behaviors are largely affected by the accumulative length  $d_{\Sigma}$  and the cohesive endurance limit  $\sigma_f$ ; meanwhile, the effects of the cyclic model parameters are also influenced by the monotonic model parameters, that is, cohesive energy and the initial cohesive strength as the  $\Delta K$  level approaches the critical value corresponding to the fracture toughness.

After the model parameter identification and the experimental validation, we confirm that the current model has the capacity to simulate the elastic-plastic fatigue crack growth behavior of IN718 at SSY, especially in Regime III. Furthermore, it remains for the next work to extend the application of the CCZM for simulating fatigue crack growth of other alloys at LSY.

### Conflicts of Interest

The authors declare that there are no conflicts of interest regarding the publication of this paper.

### Acknowledgments

This research was made possible through research funding provided by the National Natural Science Foundation of

China (no. 11502204), the National Key Research and Development Program of China (no. 2016YFB0701303), the Natural Science Basic Research Plan in Shaanxi Province of China (no. 2017JM1023), and the China Postdoctoral Science Foundation funded project (no. 2017M623234).

### References

- [1] J. Lemaitre and R. Desmorat, *Engineering Damage Mechanics: Ductile, Creep, Fatigue and Brittle Failures*, Springer-Verlag, Berlin Heidelberg, 2005.
- [2] Y. Jiang and M. Feng, "Modeling of fatigue crack propagation," *Journal of Engineering Materials and Technology*, vol. 126, no. 1, pp. 77–86, 2004.
- [3] P. Paris, M. Gomez, and W. Anderson, "A rational analytic theory of fatigue," *Trend in Engineering*, vol. 13, pp. 9–14, 1961.
- [4] R. O. Ritchie, "Mechanisms of fatigue-crack propagation in ductile and brittle solids," *International Journal of Fracture*, vol. 100, no. 1, pp. 55–83, 1999.
- [5] F. Erdogan and M. Ratwani, "Fatigue and fracture of cylindrical shells containing a circumferential crack," *International Journal of Fracture Mechanics*, vol. 6, no. 4, pp. 379–392, 1970.
- [6] S. M. Beden, S. Abdullah, and A. Ariffin, "Review of fatigue crack propagation models for metallic components," *European Journal of Scientific Research*, vol. 28, pp. 364–397, 2009.
- [7] N. Dowling and J. Begley, "Fatigue crack growth during gross plasticity and the  $J$ -integral," *Mechanics of crack growth*, vol. 590, pp. 82–103, 1976.
- [8] V. Shlyannikov, N. Boychenko, A. Tumanov, and A. Fernandez-Canteli, "The elastic and plastic constraint parameters for three-dimensional problems," *Engineering Fracture Mechanics*, vol. 127, pp. 83–96, 2014.
- [9] V. Shlyannikov, A. Tumanov, A. Zakharov, and A. Gerasimenko, "Surface flaws behavior under tension, bending and biaxial cyclic loading," *International Journal of Fatigue*, vol. 92, pp. 557–576, 2016.
- [10] M. Metzger, T. Seifert, and C. Schweizer, "Does the cyclic  $J$ -integral  $\Delta J$  describe the crack-tip opening displacement in the presence of crack closure?," *Engineering Fracture Mechanics*, vol. 134, pp. 459–473, 2015.
- [11] A. de-Andrés, J. Pérez, and M. Ortiz, "Elastoplastic finite element analysis of three-dimensional fatigue crack growth in aluminum shafts subjected to axial loading," *International Journal of Solids and Structures*, vol. 36, no. 15, pp. 2231–2258, 1999.
- [12] K. L. Roe and T. Siegmund, "An irreversible cohesive zone model for interface fatigue crack growth simulation," *Engineering Fracture Mechanics*, vol. 70, no. 2, pp. 209–232, 2003.
- [13] D. S. Dugdale, "Yielding of steel sheets containing slits," *Journal of the Mechanics and Physics of Solids*, vol. 8, no. 2, pp. 100–104, 1960.
- [14] G. I. Barenblatt, "The mathematical theory of equilibrium cracks in brittle fracture," *Advances in Applied Mechanics*, vol. 7, pp. 55–129, 1962.
- [15] J. Tryding and M. Ristinmaa, "Normalization of cohesive laws for quasi-brittle materials," *Engineering Fracture Mechanics*, vol. 178, pp. 333–345, 2017.
- [16] O. Shor and R. Vaziri, "Application of the local cohesive zone method to numerical simulation of composite structures

- under impact loading,” *International Journal of Impact Engineering*, vol. 104, pp. 127–149, 2017.
- [17] V. Tvergaard and J. Hutchinson, “The relation between crack growth resistance and fracture process parameters in elastic-plastic solids,” *Journal of the Mechanics and Physics of Solids*, vol. 40, no. 6, pp. 1377–1397, 1992.
- [18] C. R. Chen, O. Kolednik, J. Heerens, and F. D. Fischer, “Three-dimensional modeling of ductile crack growth: cohesive zone parameters and crack tip triaxiality,” *Engineering Fracture Mechanics*, vol. 72, no. 13, pp. 2072–2094, 2005.
- [19] V. Uthaisangsuk, U. Prael, and W. Bleck, “Modelling of damage and failure in multiphase high strength DP and TRIP steels,” *Engineering Fracture Mechanics*, vol. 78, no. 3, pp. 469–486, 2011.
- [20] H. Li, C. Li, and H. Yuan, “Prediction of fatigue crack growth retardation using a cyclic cohesive zone model,” *Archive of Applied Mechanics*, vol. 87, no. 6, pp. 1061–1075, 2017.
- [21] K. Park and G. Paulino, “Cohesive zone models: a critical review of traction-separation relationships across fracture surfaces,” *Applied Mechanics Reviews*, vol. 64, no. 6, article 060802, 2013.
- [22] O. Nguyen, E. A. Repetto, M. Ortiz, and R. A. Radovitzky, “A cohesive model of fatigue crack growth,” *International Journal of Fracture*, vol. 110, no. 4, pp. 351–369, 2001.
- [23] S. Maiti and P. Geubelle, “A cohesive model for fatigue failure of polymers,” *Engineering Fracture Mechanics*, vol. 72, no. 5, pp. 691–708, 2005.
- [24] A. Ural, V. Krishnan, and K. Papoulia, “A cohesive zone model for fatigue crack growth allowing for crack retardation,” *International Journal of Solids and Structures*, vol. 46, no. 11–12, pp. 2453–2462, 2009.
- [25] H. Li and H. Yuan, “Cohesive zone modelling of low cycle fatigue cracks in cracked and notched specimens,” *Fatigue & Fracture of Engineering Materials & Structures*, vol. 36, no. 12, pp. 1246–1257, 2013.
- [26] S. Jimenez and R. Duddu, “On the parametric sensitivity of cohesive zone models for high-cycle fatigue delamination of composites,” *International Journal of Solids and Structures*, vol. 82, pp. 111–124, 2016.
- [27] X. Cao and M. Vormwald, “Application of a new cohesive zone model in low cycle fatigue,” *Solids and Structures*, vol. 2, pp. 31–40, 2013.
- [28] D. Jha and A. Banerjee, “A cohesive model for fatigue failure in complex stress-states,” *International Journal of Fatigue*, vol. 36, no. 1, pp. 155–162, 2012.
- [29] H. Li, H. Yuan, and X. Li, “Assessment of low cycle fatigue crack growth under mixed-mode loading conditions by using a cohesive zone model,” *International Journal of Fatigue*, vol. 75, pp. 39–50, 2015.
- [30] ABAQUS, *Version 6.11, User Subroutines Reference Manual*, Dassault Systèmes Simulia Corp., Providence, RI, USA, 2011.
- [31] E. Lertora, C. Mandolino, and C. Gambaro, “Mechanical behaviour of Inconel 718 thin-walled laser welded components for aircraft engines,” *International Journal of Aerospace Engineering*, vol. 2014, Article ID 721680, 9 pages, 2014.
- [32] P. Beaurepaire and G. I. Schuëller, “Modeling of the variability of fatigue crack growth using cohesive zone elements,” *Engineering Fracture Mechanics*, vol. 78, no. 12, pp. 2399–2413, 2011.
- [33] J. L. Chaboche, “A review of some plasticity and viscoplasticity constitutive theories,” *International Journal of Plasticity*, vol. 24, no. 10, pp. 1642–1693, 2008.
- [34] A. Needleman, “Some issues in cohesive surface modeling,” *Procedia IUTAM*, vol. 10, pp. 221–246, 2014.
- [35] ASTM International, *Standard Test Method for Measurement of Fatigue Crack Growth Rates*, 2011.
- [36] Y. Yamada and J. C. Newman, “Crack closure under high load-ratio conditions for Inconel-718 near threshold behavior,” *Engineering Fracture Mechanics*, vol. 76, no. 2, pp. 209–220, 2009.
- [37] J. Newman, S. Smith, S. Willard, and R. Piascik, *A Comparison of Weld-Repaired and Base Metal for Inconel 718 and CRES 321 at Cryogenic and Room Temperatures*, 2004, NASA/TM-2004-213,253 ARL-TR-3266.